بسم الله الرحمن الرحيم

Sudan University of Science and Technology

College of Post Graduate Studies

A Study on the ZnO/CuO Nano-Diode Multilayer and Some of its Physical Properties

دراسة بعض الخصائص الفيزيائية للثنائي النانوي المتعدد الطبقات المصنع من ZnO/CuO

Thesis submitted for the degree "Doctor of Philosophy"

Submitted by:

FARHAH ELFADEL OMER

Supervisor

Professor: Mubarak Dirar Abdullah

Co Supervisor: Dr.Omer Salih Mohamed Nour

June 2018

الآية

بسم الله الرحمن الرحيم

(وأنزل الله عليك الكتاب و الحكمة و علمك ما لم تكن تعلم و كان فضل الله عليك عظيما)

صدق الله العظيم

DEDICUTION

To my mother, my father, brothers and my husband I am grateful for the knowledge, work ethic and values they continue to trust on me.

Acknowledgement

Firstly I would thanks **ALLAH** for His Grace and for His help to let me complete my thesis.

For most, I would like to express my sincere gratitude to my supervisor Prof. **Mubarak Dirar Abdulla** for the continuous support of my PhD study and research, for his patience, motivation, enthusiasm, and immense knowledge. His guidance helped me in all the time of research and writing of this thesis. I could not imagined having a better supervisor and mentor for my PhD study. **I** would like also to thank my **Co Supervisor: Dr.Omer Salih Mohamed Nour** who has supported me throughout my work with his patience and knowledge whilst allowing me the room to work in my own way. I have been amazingly fortunate to have a second supervisor who gave me the freedom to explore on my PhD thesis and at the same time the guidance to recover when my steps faltered.

I address my thanks to **Dr Ali Sulaiman Mohamed**, **Ustaz Abdelsakhi Sulaiman** and **Miss Mona Ali** for their help during this work.

المستخلص

اخذت البحوث في مجال المواد النانوية اهمية كبيرة لما تمتلكه هذه المواد من خصائص فيزيائية و كيمائية وبصرية فريدة مقارنة بالمادة الجسمية لهذه المواد. لذلك ركزت الدراسات الحديثة علي البنية التركيبة النانوية متعددة الابعاد لكفاتها العالية في الاجهزه النانوية . و من هذه المواد اكسيد الزنك الذي اكتسب اهمية خاصة جعلته منه قوة جاذبة في التطبيقات الالكترونية البصرية تمتلك طاقة فجوة مقدارها 3.6 eV و طاقة ربط في حدود 60 meV عند درجة حرارة الغرفة. بالمثل اكسيد النحاس له طاقة حاجز 1.2 eV مما جعلها تاخذ حيزا كبيرا في مجال البحوث النانوية وتطبيقاتها. بالاضافة المركب الناتتج من هذين الاكسيدين كوصلة ثنائية p-n وجدت تطبيقاتت في مجال الالكترونات البصرية.

في هذا البحث تم تحضير ثمانية عينات من الوصلة الثنائية ZnO/CuO لدراسة بعض الخصائص الفيزيائية كالامتصاصية والنفاذية طاقة الحاجز بتغير درجة الحرارة من C^o 60 إلى $130C^o$. كما درست الخصائص الكهربية (I-V Characteristic) وذلك بتتغير درجة الحرارة تحت الضوء المباشر في الظلام حيث اظهرت منحى شبه لوغاريثمي كما تم حساب فجوة الطاقة .

ولمعرفة الشكل البلوري والحجم النانوي اسخدمت تقنية (SEM) وذلك بتتغير درجة الحرارة ($60C^o.70C^o.80C^o.90C^o.100C^o.110C^o.120C^o.130C^o$) حيث وجد ان القطر كدالة في درجة الحرارة يتراوح

(94.69nm.92nm.109nm.130nm.169nm.222nm.561nm.1.5µm) على التوالي.

Abstract

Research on nanomaterials has become increasingly popular because of their unique physical, chemical, optical and catalytic properties compared to their bulk counterparts. Therefore, many efforts have been made to synthesize multidimensional nanostructures for new and efficient nanodevices. Among those materials, zinc oxide (ZnO), has gained substantial attention owing to many outstanding properties. ZnO besides its wide band gap of 3.34 eV exhibits a relatively large excitons binding energy (60meV) at room temperature which is attractive for optoelectronic applications. Likewise, cupric oxide (CuO), having a narrow band gap of 1.2 eV and a variety of chemo-physical properties that are attractive in many fields. Moreover, composite nanostructures of these two oxides *(CuO/ZnO)* may pave the way for various new applications. So in this thesis eight samples of CuO/ZnO junction were synthesized and exposed to temperatures 60, 70 80 90, 100, 110, 120 and 130. The electrical properties of Schottky diode junctions were analyzed by I–V measurements under the influence of direct solar radiation and, lag of radiation (darkness) which shows the semi–logarithmic $I-V$ characteristic curve of the fabricated photodiodes.

Also those samples ($CuO/d\ ZnO$ diodes) were exposed to temperatures 60, 70 80. 90, 100, 110, 120 and 130 to study the absorption, transmittance absorption coefficients and energy gap change with temperature it was found that the absorption coefficient increases while the energy gap decreases upon increasing temperature

The morphology and particle sizes of the prepared samples were determined by SEM. The SEM images of $ZnO + CuO$ sample films were heated at (60, 70 80 90, 100, 110, 120 and 130 C^{o}) temperatures are showed sphere-like $ZnO + Cu$O sample films uniform in both morphology and particle size, but have agglomeration to some extent. The average size was calculated to be (1.5

μm. 561 *nm*. 222 *nm*. 169 *nm*. 130 *nm.* 109 *nm.* 92 *nm.* 94.69 *nm.* respectively). Corresponding histograms, showing the particle size distribution, are also presented. The mean particle size which estimated from SEM is in close agreement with the average crystallite size as calculated from histograms line broadening. The microstructure and chemical composition of the film surface were analyzed using a scanning electron microscope (SEM, Tuscan Vega LMU). Their sizes are found to range from 109 to 124 nm.

Table of contents

List of Table

List of Figures

Chapter one

1.1Introduction

The little word "nano" with huge potential has been rapidly indicating itself into the world's map and has an enormous influence in every aspect of science and engineering fields. The idea of nanotechnology was introduced by Richard Feynman in his talk “There is a plenty of room at the bottom”, in 1959. Though he never explicitly mentioned "nanotechnology,"

Feynman suggested that it will eventually be possible to precisely manipulate atoms and molecules. In general, nanotechnology consists of materials with Nanoscale dimensions, remarkable properties, and great potential.

1.2 Background

During the last few decades, nanomaterials have been the subject of extensive interest because of their potential use in a wide range of fields like, optoelectronics, Catalysis and sensing applications etc . The physical and chemical properties of

nanomaterials can differ significantly from their bulk counterpart because of their small size. In general, nanomaterials comprised novel properties that are typically not observed in their conventional, bulk counterparts. Nanomaterials have a much larger surface area to volume ratio than their bulk counterparts, which is one of the basis of their novel physical and/or chemical properties. Nanomaterials are classified into one-dimensional (1D), two-dimensional (2D) and three-dimensional

(3D). at present, research on nanomaterials is intensified and is expanding rapidly.

In addition, metal oxide nanomaterials have drawn a particular attention because of their excellent structural flexibility combined with other attractive properties. These metal oxides nanostructures not only inherit the fascinating properties

from their bulk form such as piezoelectricity, chemical sensing, and photo detection, but also possess unique properties associated with their highly anisotropic geometry and size confinement [1]. The combinations of the new and the conventional properties with the unique effects of nanostructures make the investigation of novel metal oxide nanostructures a very important issue in research and development both from fundamental and industrial standpoints.

Among the various metal oxides, zinc oxide (ZnO) possessed a considerable attention due to its unique properties and applications. In particular, ZnO nanostructures (NSs) are of intense interest since they can be grown by a variety of methods with different morphologies. Among the different growth methods, the chemical bath deposition method is low temperature, simple, inexpensive and environment friendly method. These are all factors which further contribute to the resurgent attention in ZnO. Specifically, one-dimensional ZnO nanorods (NRs) amongst other nanostructures are attractive components for manufacturing nanoscale electronics and photonic devices as well as their biomedical applications because of their interesting chemical and physical properties [2, 3]. Also ZnO NRs can easily be grown on a variety of substrates like metal surface, semiconductors, glass, plastic and disposable paper substrates etc. [4-7]. Furthermore, a direct wide band gap ~ 3.37 eV and relatively large excitonic binding energy ~ 60 meV of ZnO along with many radiative deep level defects, makes ZnO attractive for its emission tendency in blue/ultraviolet and full colour lighting [8, 9]. To utilize theses properties of ZnO in LEDs application, another p-type material is necessary as ZnO NRs is unintentionally n-type material. Since mostly polymers are p-type and their special properties like low cost, low power consumption, flexible and easy manufacturing all makes polymers a better choice to use with ZnO NRs to fabricate a flexible device that utilizes the properties of both materials for large area lighting and display application [10, 11].

On the other hand, natural abundance of copper (II) oxide (CuO) as well as its low production cost, good electrochemical and catalytic properties makes the copper oxide to be one of the best materials for various applications. CuO also has a variety of nanostructures and can be grown using the low temperature aqueous chemical method. It is one of the most important catalysts and is widely used in environmental catalyst.

One-dimensional (1-D) metal oxide (MO) nanostructures have attracted much attention in fabricating unique optoelectronic, electronic, and electrochemical devices such as UV sensors 1, solar cells 2, and gas sensors 3. It pertains to those applications that nanorods possess relatively large aspect ratio and relatively large surface area to volume ratio ensuring high efficiency and sensitivity. As for materials of choice, zinc oxide (ZnO) is an environmentally friendly n-type semiconductor that has better electron mobility compared to other wide band gap oxides including TiO2 [4]. Therefore, ZnO is expected to exhibits faster electron transport with reduced recombination loss. Different types of ZnO nanostructures have been used as gas sensors to detect gases, vapors, and metal ions, such as ethanol [3, 5], NH_3 [6], O_2 [7], and Ca^{+} [8]. Likewise, CuO is an important p-type semiconductor with a narrow band gap (1.2 eV). CuO has been intensively studied for sensing devices due to its rich family of nanostructures and promising electrochemical and catalytic properties [8-11]. Previously reported CuO nanostructures are grown on Cu substrate using thermal oxidation process or synthesized through wet chemical routes on other supporting substrates like glass. However , CuO nanostructures (NS) grown by the later method showed poor adhesion to the substrates [11]. In recent years, the simple and cost effective hydrothermal method has proven to be successful for the synthesis of nanostructures of CuO or ZnO[12, 13]. By combining the advantages of both nanostructures in a composite simple, reliable and cost effective synthesis route might be realized. Many combinations of CuO and ZnO

nanostructures have been demonstrated, but involve high temperature (>500 oC) to oxidize a Cu foil into CuO followed by the deposition of ZnO [14]. Furthermore, Jung, S. et al [15] recently demonstrated the fabrication of flower-like CuO ZnO nanowire Heterostructures by photochemical deposition, which is a slow and rather expensive process.

1.3 The Problem of the study

There has been much debate on the future implications of nanotechnology. Nanotechnology has the potential to create many new material and devices with a vast range of application, such as medicine,, electronics and energy production. On the other hand, nanotechnology raises many of the same issues as with any introduction of new technology, including concerns about toxicity and environmental impact of nanomaterials [16]. And their potential; effects on global economics, as well as speculation about various doomsday scenarios. These concerns have led to a debate among advocacy and governments on whether special regulation of nanotechnology is warranted.

1.4 The Objective of the study

The objective of this thesis is

1. To synthesize metal oxide semiconductor nanostructures and utilize them for light emitting diodes, catalytic and sensing applications
2. To study the effect of temperature on their optical properties
3. To study I-V characteristics under the influence of temperature variation
4. To study of the morphology and particle size using the SEM under temperature variation

1.5 The Method of study

For the ease of gathering all presented work, the thesis is divided into

Parts:

i) Synthesis of ZnO and CuO nanostructures. The morphology, crystal structure

and crystallinity of the nanostructures were monitored by using scanning electron
microscope (SEM) and x-ray diffraction.

ii) Fabrication of a solution-process able hybrid ZnO NRs/polymer light emitting diodes (LEDs) on flexible substrates. N-type ZnO NRs. Along with the properties of the ZnO NRs, choice of the polymer is also crucial for tuning the emission of fabricated LEDs. The emission colour of the hybrid LEDs can be tuned by blending different polymers or by changing the polymer concentrations.

iii) Utilization of the CuO nanostructures to develop a pH sensor and exploit these NSs as a catalyst to degrade organic dyes. Owing to its good electrochemical activity, CuO is a promising candidate for sensing applications. Thus, CuO based pH sensor was developed to check the sensitivity and response over a wide pH range. Moreover, CuO is known to be a good catalyst and morphology of the CuO affects the properties of the catalyst in general. Therefore CuO NSs having different morphology were investigated to boost the degradation of the organic dyes.

iv) Finally, extend the growth of ZnO and CuO to achieve their composite CuO/ZnO nanostructure. The growth kinetics of composite NSs was studied and found that it depends on the nature and the pH value of the nutrient solution. The CuO/ZnO nanocomposite exhibited a broad and extended light absorption covering the whole visible range.

1.6 Thesis Scope

The general introduction and the objective of the thesis are presented in chapter one. Some basic properties of ZnO, CuO and polymers are studied in chapter two. The theoretical back ground discussed on chapter three.

The literature review is the subject of chapter four. The material and method in addition to conclusion of whole work and possible future prospects were demonstrated in chapter five.

Chapter two

. Some basic properties of ZnO, CuO

2.1 Back ground

The little word "nano" with huge potential has been rapidly indicating itself into the world's map and has an enormous influence in every aspect of science and engineering fields. The idea of nanotechnology was introduced by Richard Feynman in his talk “There is a plenty of room at the bottom”, in 1959. Though he never explicitly mentioned "nanotechnology," Feynman suggested that it will eventually be possible to precisely manipulate atoms and molecules. In general, nanotechnology consists of materials with nanoscale dimensions, remarkable properties, and great potential.

During the last few decades, nanomaterials have been the subject of extensive interest because of their potential use in a wide range of fields like, optoelectronics,

catalysis and sensing applications etc. The physical and chemical properties of nanomaterials can differ significantly from their bulk counterpart because of their small size. In general, nanomaterials comprised novel properties that are typically not observed in their conventional, bulk counterparts. Nanomaterials have a much larger surface area to volume ratio than their bulk counterparts, which is one of the basis of their novel physical and/or chemical properties. Nanomaterials are

classified into one-dimensional (1D), two-dimensional (2D) and three-dimensional (3D). At present, research on nanomaterials is intensified and is expanding rapidly.

In addition, metal oxide nanomaterials have drawn a particular attention because of their excellent structural flexibility combined with other attractive properties. These metal oxides nanostructures not only inherit the fascinating properties

from their bulk form such as piezoelectricity, chemical sensing, and photodetection, but also possess unique properties associated with their highly anisotropic geometry and size confinement [17]. The combinations of the new and the conventional properties with the unique effects of nanostructures make the investigation of novel metal oxide nanostructures a very important issue in research and development both from fundamental and industrial standpoints.

Among the various metal oxides, zinc oxide (ZnO) possessed a considerable attention due to its unique properties and applications. In particular, ZnO nanostructures (NSs) are of intense interest since they can be grown by a variety of methods with different morphologies. Among the different growth methods, the chemical bath deposition method is low temperature, simple, inexpensive and environment friendly method. These are all factors which further contribute to the resurgent attention in ZnO. Specifically, one-dimensional ZnO nanorods (NRs) amongst other nanostructures are attractive components for manufacturing nanoscale electronics and photonic devices as well as their biomedical applications because of their interesting chemical and physical properties [18, 19]. Also ZnO NRs can easily be grown on a variety of substrates like metal surface, semiconductors, glass, plastic and disposable paper substrates etc. [20-21]. Furthermore, a direct wide band gap ~ 3.37 eV and relatively large excitonic binding energy ~ 60 meV of ZnO along with many radiative deep level defects, makes ZnO attractive for its emission tendency in blue/ultraviolet and full colour lighting [22, 23]. To utilize theses properties of ZnO in LEDs application, another p-type material is necessary as ZnO NRs is unintentionally n-type material. Since mostly polymers are p-type and their special properties like low cost, low power consumption, flexible and easy manufacturing all makes polymers a better choice to use with ZnO NRs to fabricate a flexible device that utilizes the properties of both materials for large area lighting and display application [24, 25].

On the other hand, natural abundance of copper (II) oxide (CuO) as well as its low production cost, good electrochemical and catalytic properties makes the copper oxide to be one of the best materials for various applications. CuO also has a variety of nanostructures and can be grown using the low temperature aqueous chemical method. It is one of the most important catalysts and is widely used in environmental catalyst.

2.2 Materials and properties

ZnO is a wide band gap material possessing many interesting properties and probably the richest family of nanostructures. Moreover, CuO is a narrow band gap material and has been studied extensively. In this chapter we aim to narrate some properties of ZnO and CuO in *a* comprehensive manner, as well as discuss the polymers which are used in this work.

2.2.1 Zinc Oxide

Zinc oxide (ZnO) is a metal oxide semiconductor with wurtzite structure under ambient condition. The wurtzite structure has hexagonal unit cell as shown in figure (2.1). In this crystal structure, two interpenetrating hexagonal-close-pack (hcp) sub lattices are alternatively stacks along the c-axis. One sub lattice consists of four Zn atoms and the other sub lattice consists of four Oxygen O atoms in one unit cell; every atom of one kind is surrounded by four atoms of the other kind and forms a tetrahedron structure [26].

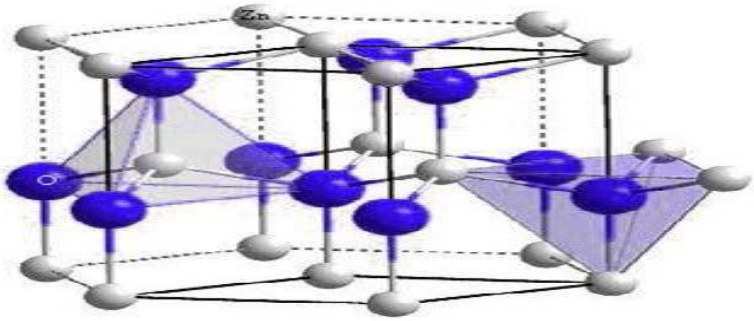

Figure (2.1) the hexagonal wurtzite structure of ZnO [reproduced from [Wikipedia].

ZnO commonly consists of polar (0001) and non-polar (10-10), (11-20) surfaces. The surface energy of the polar surface is higher than the non-polar surfaces and Therefore the preferential growth direction of ZnO NR is along the <0001> [27]. Figure (2.2) shows the schematic diagram of a ZnO NR growing along the <0001> direction or along the c-axis.

Figure (2.2), Schematic diagram of ZnO NR showing the growth direction.

The enormous interest of using ZnO in optoelectronic devices is due to its excellent optical properties. The direct wide band gap of ZnO ~ 3.4eV is suitable for short wavelength optoelectronic applications, while the high excitons binding energy ~ 60 meV allows efficient excitonic emission at room temperature [28]. Moreover ZnO, in addition to the ultraviolet (UV) emission, emits covering the whole visible region i.e. containing green, yellow and red emission peaks [29-30]. The emission in the visible region is associated with deep level defects. Generally oxygen vacancies (VO), zinc vacancies (VZn), zinc interstitials (Zni), and the incorporation of hydroxyl (OH) groups in the crystal lattice during the growth of ZnO are most common sources of the defects related emission [31-32]. ZnO naturally exhibits n-type semiconductor polarity due to native defects such as oxygen vacancies and zinc interstitials. P-type doping of ZnO is still a challenging problem that is hindering the possibility of a p-n homojunction ZnO devices. Furthermore, the remarkable properties of ZnO like being bio-safe, bio-compatible, having high-electron transfer rates and enhanced analytical performance are suitable for intra/extra-cellular sensing applications [33, 34]. Some basic physical parameters of ZnO at the room temperature are presented in the table (2.1).

Table (2.1) some basic properties of wurtzite ZnO.

Property	Value	Reference
Lattice Parameters	a= b=3.25 *Å* c=5.21 *Å*	[12, 22]
Stable crystal structure	Wurtzite	[10]
Density	5.606 gm/cm^3	[25]
Melting point	1975 C^o	[26]
Dielectric constant	8.66	[10]
Refractive index	2.008	[10, 27]
Energy gap	3.4 eV, direct	[28]
Exaction binding energy	60 *meV*	[27]
Effective mass Electron/Hole	0.24 *mo*/0.59 *mo*	[25]
Electron mobility	100-200 cm^2/VS	[29]
Hole mobility	5-50 cm^2/VS	[29]
Bulk young modulus	111.2±4.7 *GPa*	[28]

2.2.2 Copper (II) Oxide

Copper (II) oxide (CuO) is another metal oxide semiconductor having narrow band gap ~ 1.2 eV in bulk. CuO has monoclinic crystal structure as shown in figure 2.3, and belongs to the space group 2/m. The copper atom is coordinated by four oxygen atom in a square planer configuration [30]. It is intrinsically p-type semiconductor. CuO draw much attention since the starting growth material is inexpensive and easy to get, and the methods to prepare these materials are of low cost [31].

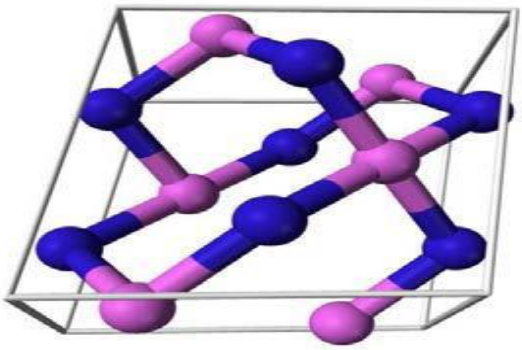

Figure (2.2) the monoclinic crystal structure of CuO [reproduced from Wikipedia].

CuO nanostructures (NSs) have stimulated intensive research due to their high surface area to volume ratio. CuO NSs are a good candidate for sensing owing to its exceptional electrochemical activity and the possibility of promoting electron transfer at a low potentials [30]. Due to the photoconductive and photochemical properties, CuO NSs are also promising materials for the fabrication of solar cells [31, 32]. CuO based materials are well known with regard to their high temperature superconductivity and the relatively huge magneto resistance [33, 34]. Additionally, This compound is well-known for its excellent performance as a sensing material for hazardous gas detection and as negative electrode in lithium ions batteries [35-37]. CuO is very important from the standpoint of the catalytic usage and the morphology affects the properties of a catalyst in general [38]. It is therefore significant to synthesize novel sizes and shapes of the CuO NSs and to further improve its application as a catalyst. Some of the physical features of CuO are summarized in table (2.2).

Table (2.2) some basic properties of CuO at room temperature.

Property	Value	Reference
Lattice Parameters	a= b=3.25 Å c=5.21 Å	[10 22]
Stable crystal structure	wurtzite	[10]
Density	5.606 gm/cm^3	[23]
Melting point	1975 C^o	[24]
Dielectric constant	8.66	[10]
Refractive index	2.008	[10, 25]
Energy gap	3.4 eV, direct	[26]
Exaction binding energy	60 meV	[25]
Effective mass Electron/Hole	0.24 mo/0.59 mo	[23]
Electron mobility	100-200 cm^2/VS	[27]
Hole mobility	5-50 cm^2/VS	[27]
Bulk young modulus	111.2±4.7 GPa	[26]

2.3 Synthesis and characterization of nanomaterials

The growth procedure of the ZnO and CuO nanostructures are described in this chapter. The low temperature chemical bath deposition method was chosen for the growth of ZnO, CuO and their composite nanostructures. After the growth, diverse characterization techniques were used to probe the morphology and structural aspects of the as grown nanomaterials. The techniques used during this work are: scanning electron microscope (SEM), transmission electron microscope (TEM) and x-ray diffraction analysis. The working principles of these techniques are appended in [39-55].

2.3.1 Synthesis of ZnO

In recent years, with the increasing awareness of both environmental safety and the need for optimal energy utilization, there is a case for the development of nonhazardous materials. These materials should not only be compatible with human life but also with other living forms or species. Moreover, processing methods such as fabrication, manipulation, treatment, reuse, and recycling of waste materials should be environmentally friendly. In this respect, the hydrothermal technique occupies a unique place in modern science and technology.

The hydrothermal growth technique is promising for low cost and for scaling up the synthesis of nanostructures. This technique is not only useful to grow single material but can also be useful to synthesize nano-hybrid or nano-composite materials [56,-66]. Moreover, the hydrothermal growth occurs at low temperature and therefore has great pledge for nanostructures to be synthesized on various flexible plastic and paper substrates. This low temperature growth also makes it easier to integrate nanomaterials with organic optoelectronic material. The chemical bath deposition (CBD) method is an example of the hydrothermal method which was used for the synthesis of ZnO NRs and CuO NSs presented in this thesis.

2.3.2 Chemical bath deposition growth of ZnO NRs

The chemical bath deposition is a two step growth technique for ZnO NRs growth. Figure (3.1) is the schematic illustration of the CBD growth of ZnO NRs. First step is to cover the substrate with a seed layer of ZnO nanoparticles which serve as a nucleation sites for the growth of the NRs. The seed layer is beneficial for the growth of aligned NRs and it can also control the density of the grown NRs [67]. The seed layer that is used in our work is prepared as follow: 5 mM of zinc acetate (Zn(CH3COO)2) and 2 mM of KOH were dissolved in

methanol separately and then under continuous stirring both solutions were mixed.

Prior to the start of the growth of ZnO NRs substrate cleaning is a necessary step. Acetone, isopropanol and de-ionized (DI) water were separately used under ultrasonication bath to clean the substrates. Then spin coating of the seed layer on the substrate (plastic, paper and metal coated glass) at a speed of 3000 rpm for 30 seconds. The thickness of the seed layer is controlled by adjusting the speed of the spin coater which can control the density and alignment of the ZnO NRs.

The aqueous solution of zinc nitrate (Zn(NO3)2. 6H2O) and hexamethylenetetramine (HMT) in equimolar amount of 0.1 M was prepared in a reaction vessel. The pre-seeded substrate was then immersed in the precursor solution and loaded in a laboratory oven at 50 oC for several hours (h). After the growth process the samples were soaked in DI water to remove the residuals and dried with N2 blow. The ZnO NRs density, morphology and aspect ratio can be controlled by adjusting the reaction parameters like e.g. precursor concentration, pH value, growth temperature and growth time [68].

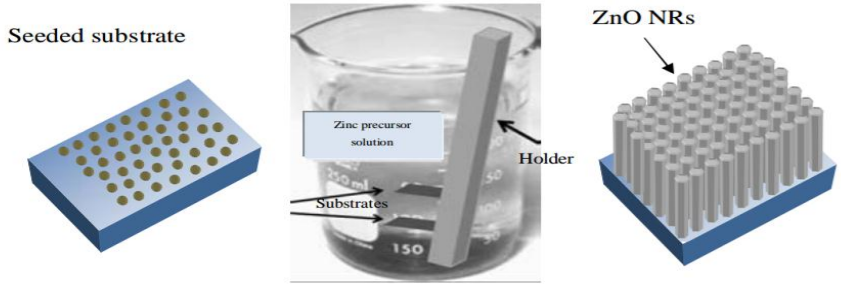

Figure (2.3) Schematic diagram of the CBD growth of ZnO NRs.

2.3.3 Characterization of ZnO NRs

The morphology of the ZnO NRs was investigated by using SEM which is an important technique to study the surface morphology at the nanoscale. The SEM image of the ZnO NRs grown on various substrates e.g. plastic, metals and

semiconductors are demonstrated in figure 3.2. It is seen that ZnO NRs covered the substrates uniformly and grow perpendicular to the substrates. ZnO NRs with well identified hexagonal facet are obtained shown in the high magnification image (inset of figure (3.2). This shows that the ZnO NRs can easily be grown on any amorphous and crystalline substrate morphology at low temperature ~ 50 ^{o}C.

Chapter three

Theoretical back ground

3.1 Preface

A pn junction at equilibrium is characterized by a depletion region where there are no charge carriers (except for those created and annihilated dynamically) and a contact potential. The contact potential is related to the doping concentration in the p and n sides with higher concentrations leading to larger contact potentials. This, in turn, is related to the position of the Fermi levels in the p and n sides since a higher do pant concentration pushes the Fermi level closer to the valence or conduction band. The pn junction can be biased by connecting to an external circuit and there are two types of biasing (similar to the arguments for the metal-semiconductor Schottky junction)

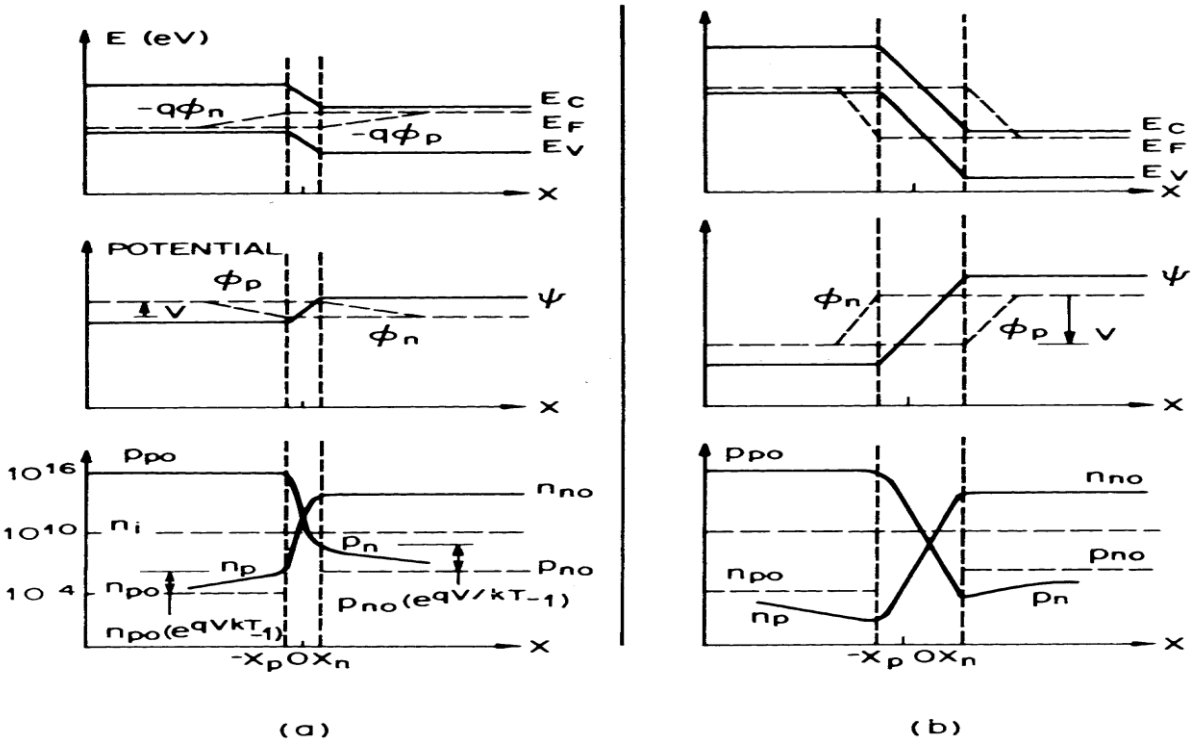

Figure (3.1) shows Energy band diagrams showing the intrinsic Fermi level , the quasi-Fermi levels for electrons *n* and holes *p* , and the carrier distributions for forward (a) and reverse bias conditions (b).

3.2 formation of depletion layer in PN junction

Electrons and holes diffuse into regions with lower concentrations of electrons and holes, much as ink diffuses into water until it is uniformly distributed. By definition, N-type semiconductor has an excess of free electrons compared to the P-type region, and P-type has an excess of holes compared to the N-type region. Therefore when N-doped and P-doped pieces of semiconductor are placed together to form a junction, electrons migrate into the P-side and holes migrate into the N-side. Departure of an electron from the N-side to the P-side leaves a positive donor ion behind on the N-side, and likewise the hole leaves a negative acceptor ion on the P-side.

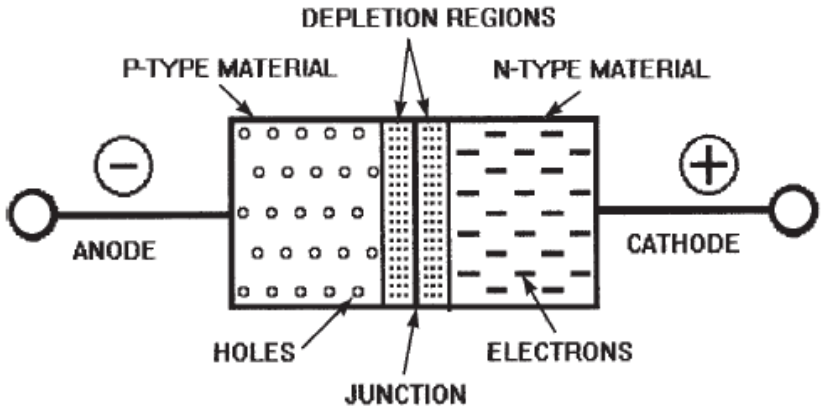

Figure (3.2) shows formation of depletion layer in PN junction

The diffused electrons come into contact with holes on the P-side and are eliminated by recombination. Likewise for the diffused holes on the N-side. The net result is the diffused electrons and holes are gone, leaving behind the charged ions adjacent to the interface in a region with no mobile carriers (called the depletion region). The uncompensated ions are positive on the N side and negative on the P side. This creates an electric field that provides a force opposing the continued exchange of charge carriers. When the electric field is sufficient to arrest further transfer of holes and electrons, the depletion region has reached its equilibrium dimensions. Integrating the electric field across the

depletion region determines what is called the built-in voltage (also called the junction voltage or barrier voltage or contact potential

3.3 **Forward bias**

Consider a pn junction under forward bias. This is achieved by connecting the p side to the positive terminal of an external power source and the n side to the negative terminal. In reverse bias, the connections are interchanged. Equilibrium, forward, and reverse bias connections are shown in figure 1. In the forward bias the external potential (V) opposes the contact potential, V_0, that develops in equilibrium. The effect of this is that the net potential at the junction is lowered. In the presence of an external potential the Fermi levels no longer line up but are shifted. This shift can be seen in the band diagram, summarized in figure (3.2. The application of the external potential, in forward bias, shifts the n side up with respect to the p side, see figure (3.2).

This leads to a lowering of the barrier for injection of electrons from the n to the p side (there is a similar lowering of the barrier for holes to be injected from p to n side) and leads to a current in the circuit. This current is due to the injection of minority carriers in the pn junction. In forward bias, the p-type is connected with the positive terminal and the n-type is connected with the negative terminal. i^{th} a battery connected this way, the holes in the P-type region and the electrons in the N-type region are pushed toward the junction. This reduces the width of the depletion zone.

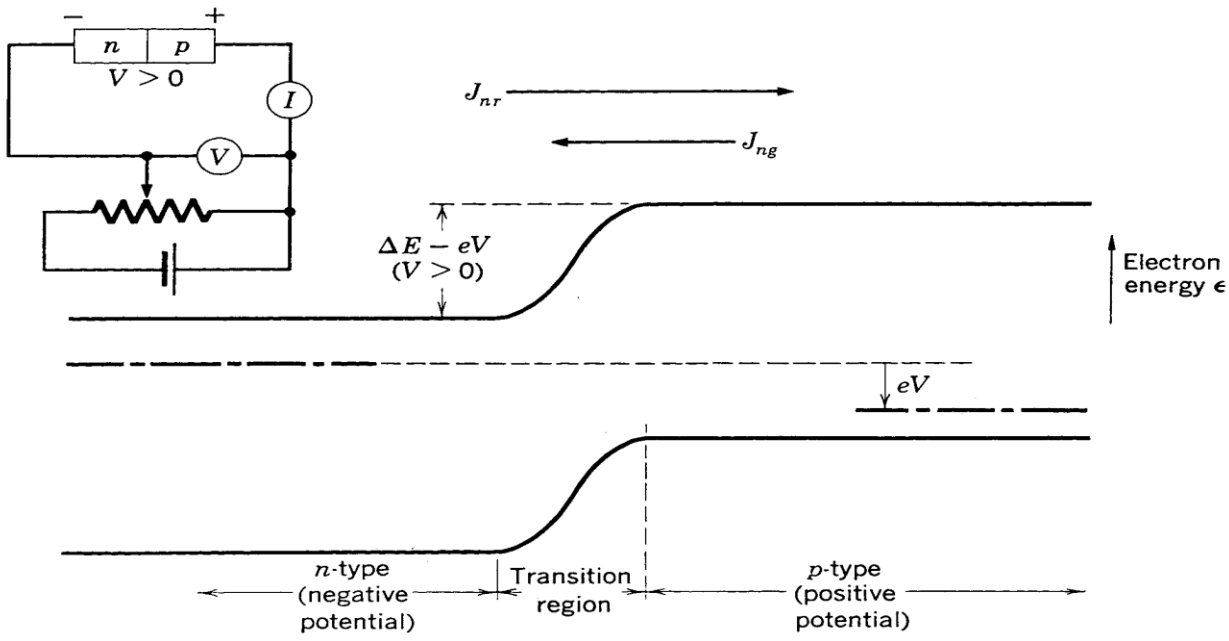

Figure (3.3) Band diagram of pn junction under reverse bias.

The Fermi level on the positive potential applied to the P-type material repels the holes, while the negative potential applied to the N-type material repels the electrons. As electrons and holes are pushed toward the junction, the distance between them decreases. This lowers the barrier in potential. With increasing forward-bias voltage, the depletion zone eventually becomes thin enough that the zone's electric field cannot counteract charge carrier motion across the p–n junction, as a consequence reducing electrical resistance. The electrons that cross the p–n junction into the P-type material (or holes that cross into the N-type material) will diffuse in the near-neutral region. Therefore, the amount of minority diffusion in the near-neutral zones determines the amount of current that may flow through the diode.

3.3.1 Forward bias current

Consider the pn junction schematic shown in figure (3.3).The excess electron concentration at the interface between the depletion width and the p side is $n_p(0)$ and similarly the excess hole concentration on the n side is $p_n(0)$.

These excess carriers are replenished by the applied voltage of the external circuit so that a current owes through the entire circuit.

Consider the n side of the junction, where the excess minority carriers are holes. When the length of the n region is longer than the diffusion length, the hole concentration at a distance x from the depletion region, marked in figure (3.3) is given by

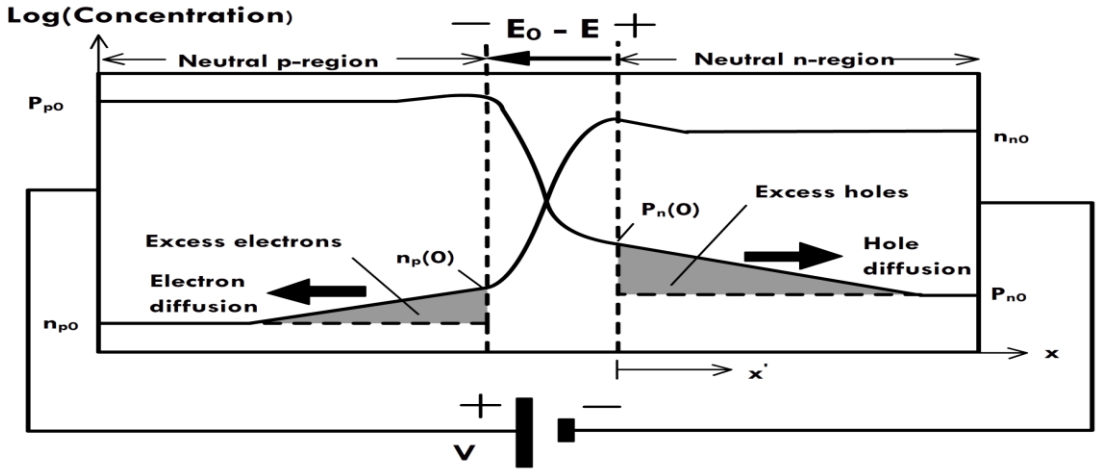

Figure (3.4) Current in a pn junction is due to injection of minority carriers in forward bias. These excess carriers can diffuse before recombining with the majority carriers. Adapted from Principles of Electronic Materials - S.O. Kasap.

The excess holes is above the base hole concentration in the n side, which is very small. The hole diffusion current (J_D; hole) is then defined by the diffusion coefficient and concentration gradient

3.3.2 Band gap dependence

Consider the reverse saturation current (J_{S0}) shown in equation 11. This contains the termn_{2i}, which is the intrinsic carrier concentration. This is a material property, for a given temperature, and depends on the band gap. Vg here represents the band gap $E_g$converted into a potential (dividing by e). The diffusion current then depends on a temperature dependent constant multiplied

by a term that depends on the band gap. The forward bias I-V characteristics for different semiconductors are plotted in figure (3.6). For a given current value, the voltage required is higher with higher Vg (higher band gap).

3.4 Reverse bias

In forward bias the current increases exponentially with the applied voltage.

The external potential opposes the in-built potential and has the effect of lowering the barrier for the electrons and holes. In reverse bias, the applied external potential is in the same direction as the contact potential. This is shown schematically in figure (3.7). The p side is connected to the negative potential and the n side is connected to the positive potential. The effect of the reverse bias on depletion width is shown schematically in figure (3.1). The reverse bias causes the depletion region width to increase since the majority carriers are attracted to the external potential. In the energy band diagram

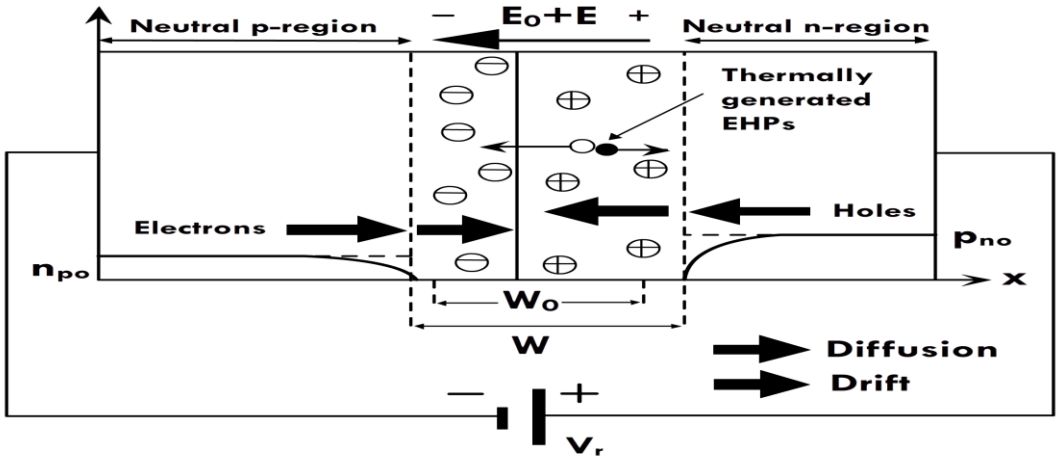

Figure (3.5) Reverse bias configuration for a pn junction. The total potential at the depletion region is increases. This has the effect of increasing the depletion width making it harder for carriers to cross the junction. Adapted from Principles of Electronic Materials - S.O. Kasap.

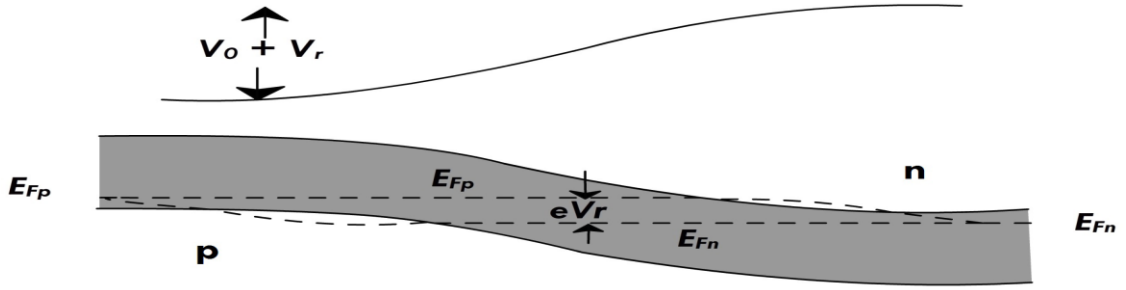

Figure (3.6) Band diagram of pn junction under reverse bias. The Fermi level on the n side shifts down leading to a overall increase in the junction potential. Adapted from Semiconductor device physics and design - Umesh Mishra and Jasprit Singh.

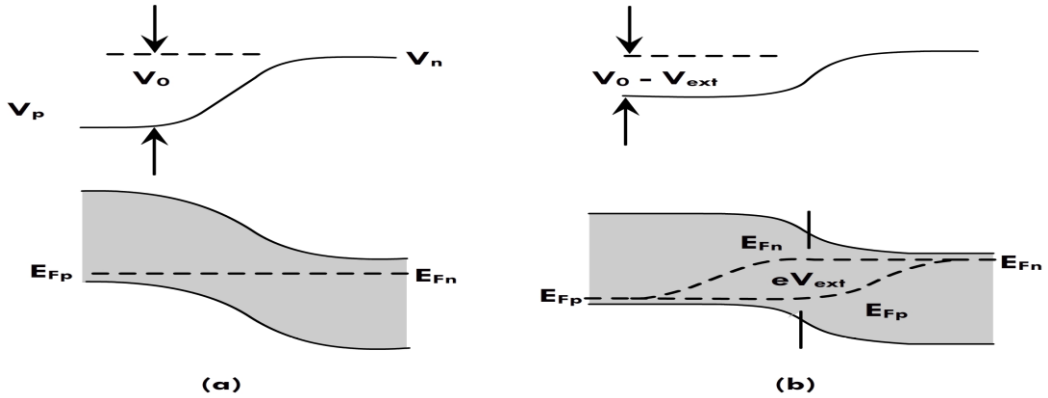

Figure (3.7) Band diagram of pn junction under (a) equilibrium and (b) forward bias. While Fermi levels line up in equilibrium in the presence of an external potential the levels shift by an amount proportional to the applied potential. Adapted from Semiconductor device physics and design - Umesh Mishra and Jasprit Singh**.**

The Fermi levels are shifted, as shown in figure (3.5). This is opposite to the direction of forward bias, shown in figure (3.2). Because of the higher barrier, diffusion current is negligible in reverse bias. There is however a small current that owns through the pn junction, called the reverse saturation current.

This current is a constant (independent of reverse bias voltage) and is generated by drift of the thermally generated carriers in the depletion region.

Electron and holes dynamically generated in the depletion region get accelerated towards the n and p side due to the applied voltage and this leads to a small reverse saturation current, also called drift current. This is given by Js0,. Connecting the P-type region to the negative terminal of the battery and the N-type region to the positive terminal corresponds to reverse bias. If a diode is reverse-biased, the voltage at the cathode is comparatively higher than the anode. Therefore, no current will flow until the diode breaks down. The connections are illustrated in the diagram to the right.

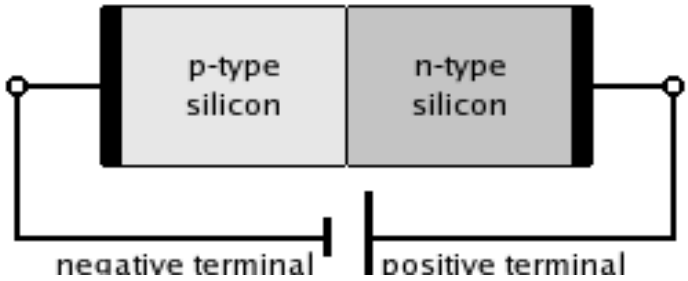

Figure (3.8) p-n type

Because the p-type material is now connected to the negative terminal of the power supply, the 'holes' in the P-type material are pulled away from the junction, causing the width of the depletion zone to increase. Likewise, because the N-type region is connected to the positive terminal, the electrons will also be pulled away from the junction. Therefore, the depletion region widens, and does so increasingly with increasing reverse-bias voltage. This increases the voltage barrier causing a high resistance to the flow of charge carriers, thus allowing minimal electric current to cross the p–n junction. The increase in resistance of the p–n junction results in the junction behaving as an insulator.

3.5 Depletion Region

•As electrons diffuse from the n region into the p region and holes diffuse from the p region into the n region, the ionized donors and acceptors that created the

electrons and holes are left behind as the donors and acceptors are bound in place by their bonds with the Si atoms in the crystal.

These fixed charges induce an electric field in the semiconductor, which produces a drift currents that counters the diffusion currents.

▫The depletion region is the distance over which the electric field is induced.

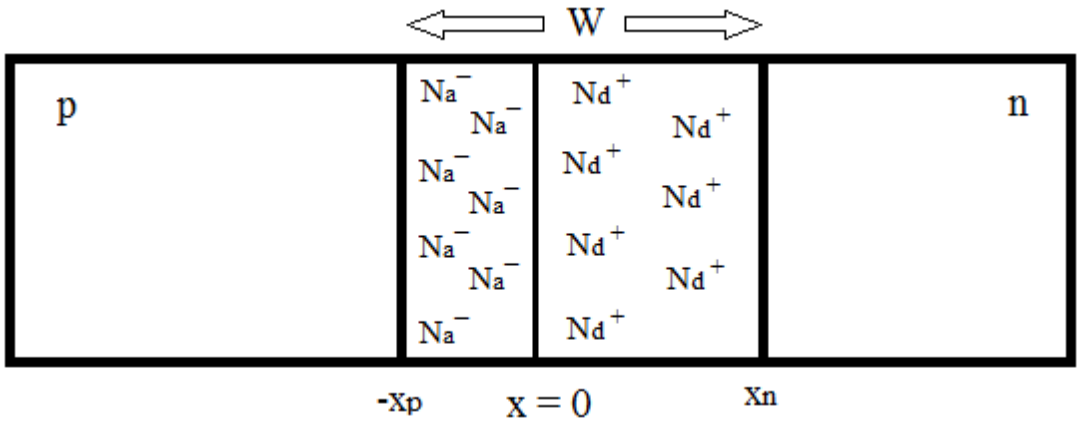

Figure (3.9) Depletion Region

The number of ionized acceptors in the depletion region is equal to the number of ionized donors.

▫In the diagram below, the n-type region is more lightly doped (has fewer donors per cubic centimeter) and the p-type region.

▫Therefore, the depletion width extends deeper into the n-region and the p region.

x = 0 is the metallurgical interface between the p-type material and the n-type material. -xp and xn are the edges of the depletion region in the p-type and n-type material, respectively.

3.6 Operating principle and characteristics of a p-n junction diode

A p-n junction diode is formed by placing **p** and **n** type semiconductor materials in intimate contact on an atomic scale. This may be achieved by diffusing acceptor impurities in to an **n** type silicon crystal or by the opposite sequence.

A junction is characterized by the doping level (impurity atom density). In a step junction accepter atom density has a high constant value in the **p** region and a very low value in the **n** region. The opposite holds true for the donor atom density. In a graded junction impurity density changes more gradually across the junction. Figure (3.1) shows a typical plot of impurity densities for both types of junction.

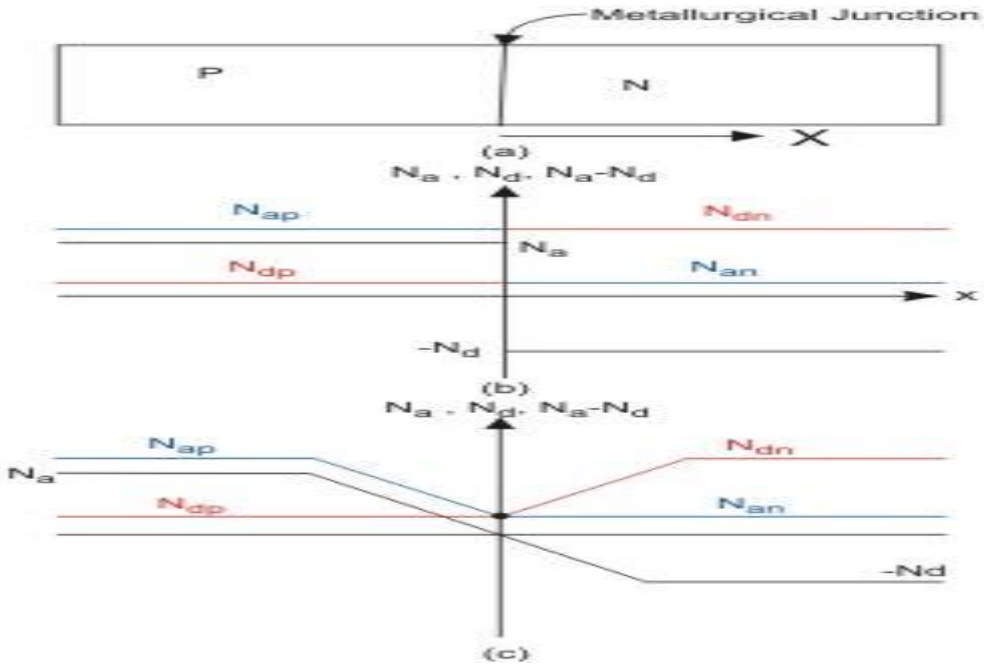

Figure (3.10) Schematic diagram and impurity atom densities in a p-n junction (a) Schematic diagram, (b) Impurity density in a step junction, (c) Impurity density in a graded junction.

For the rest of the discussion a step **p-n** junction will be assumed. In an open circuit p-n junction majority carriers from either side with defuse across the junction to the opposite side where they are in minority. These diffusing carriers will leave behind a region of ionized atoms at the immediate vicinity of the metallurgical junction. This region of immobile ionized atoms is called the "space charge region". Accumulated space charges give rise to an electric field and potential barrier at the junction which opposes the diffusion of carriers. Once

the electric field and the potential barrier develop to sufficient level, migration of carriers across the junction stops. At this point the **p-n** junction is said to have attained "thermal equilibrium". A somewhat idealized plot of the variation of the space charge density, the electric field and the electric potential along the device is shown in Figure (3.2).

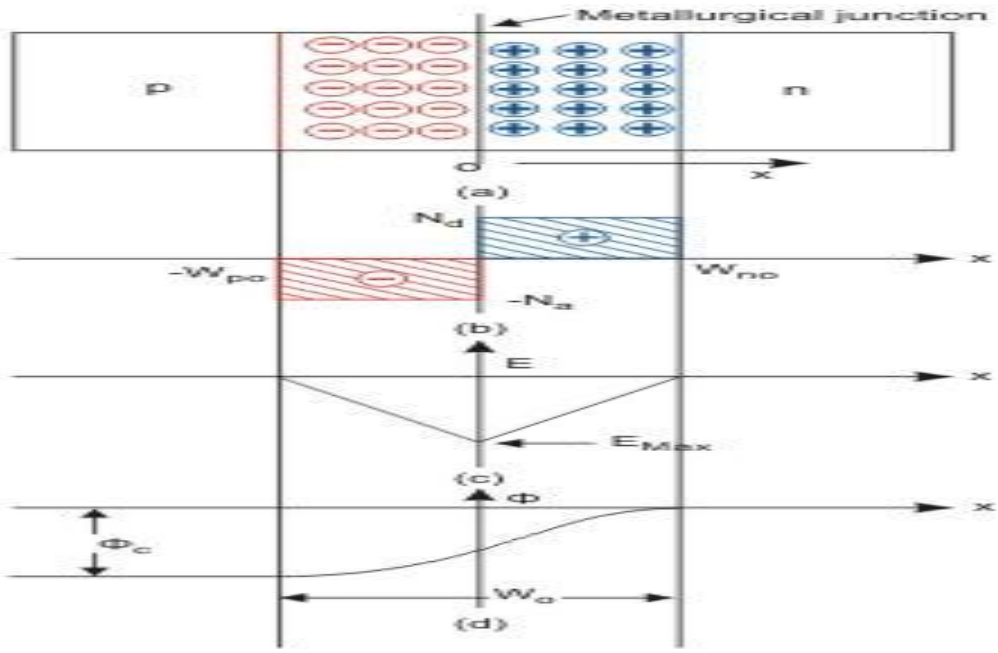

Figure (3.11) Space charge density, electric field and electric potential inside a p-n junction in thermal equilibrium; (a) schematic diagram; (b) space charge density; (c) electric field; (d) electric potential.

The space charge densities in this idealized representation are assumed to be step functions of magnitudes –Na and Nd on the **p** are **n** sides respectively over the space charge regions ($-W_{po}$ in the p side and W_{no} in the n side).

Under this assumption the electric field strength is obtained by solving the one dimensional Poisson's equation.

$$\frac{dE(x)}{dx} = \frac{-qNa}{\in} \quad -W_{po} < x \le 0 \qquad (3.1)$$

$$E(-w_{ro}) = 0$$

$$\therefore E(x) = \frac{-qNa(x + W_{po})}{\in}, -W_{po} < x \le 0 \qquad (3.2)$$

$$\frac{dE(x)}{dx} = \frac{qNd}{\in} \quad 0 < x \le W_{no} \qquad (3.3)$$

$$E(W_{no}) = 0$$

$$\therefore E(x) = \frac{qNd(x - W_{no})}{\in} \; 0 < x \le W_{no} \qquad (3.4)$$

From (3.2) $E_{max} = E(0) = \frac{-qN_a W_{po}}{\in}$ (3.5)

From (3.4) $E_{max} = E(0) = \frac{-qN_d W_{no}}{\in}$ (3.6)

Since E(x) is continuous at x=0, from (3.5) and (3.6) (3.7)

$$N_a W_{po} = N_d W_{no}$$

Now $\phi_c = -\int_{-W_{po}}^{W_{no}} E(x)\,dx = \frac{q(N_a W_{po}^2 + N_d W_{no}^2)}{2\in}$ (3.8)

Using (3.7) in (3.8)

$$\phi_c = \frac{qN_a W_{po}(W_{po} + W_{no})}{2\in} = \frac{qN_d W_{no}(W_{po} + W_{no})}{2\in} \qquad (3.9)$$

Substituting $W_{po} + W_{no} = W_o$ = Zero bias space charge layer width

$$W_{po} = \frac{2\in\phi_c}{qW_o}\,\frac{1}{N_a} \;;\; W_{no} = \frac{2\in\phi_c}{qW_o}\,\frac{1}{N_d} \qquad (3.10$$

$$\therefore W_{po} + W_{no} = W_o = \frac{2 \in \phi_c}{qW_o} \frac{N_a + N_d}{N_a N_d}$$

$$\therefore W_o = \sqrt{\frac{2 \in \phi_c (N_a + N_d)}{qN_a N_d}} \quad (3.11)$$

From (3.7) & (3.10) $|E_{max}| = 2\phi_c / W_o$ (3.12)

In all these equations q is the charge of an electron and $\in$ is the dielectric constant of the semiconductor material.

When an external voltage V is applied across the **p** and **n** sides, it adds or subtracts with the contact potential ϕ_C. If the **p** side is made more positive with respect to the **n** side (assumed positive convention of V) it subtracts from ϕ_C. Since the potential barrier reduces, the width of the space charge layer and the maximum electric field strength at the junction also reduce. The **p-n** junction is said to be forward biased under this condition. Reversing the polarity of V (i.e reverse biasing the **p-n** junction) has the opposite effect.

Application of an external voltage does not qualitatively change the shapes of the space charge density, electric field or the electric potential distribution. Therefore, all the relationships given so far hold good with suitable modifications. In particular

W(v) = Width of the space charge region with applied external voltage V

$$= \sqrt{\frac{2 \in (N_a + N_d)}{qN_a N_d} (\phi_c - V)} = \sqrt{\frac{2 \in \phi_c (N_a + N_d)}{qN_a N_d} \left(1 - \frac{V}{\phi_c}\right)}$$

$$\text{or } W(v) = W_o \sqrt{1 - \left(V / \phi_c\right)} \quad (3.13)$$

$$\text{Similarly } \left|E_{max}(v)\right| = \frac{2(\phi_c - V)}{W(v)} = \frac{2\phi_c\left(1 - V/\phi_c\right)}{W_o\sqrt{1 - V/\phi_c}}$$

$$\text{or } \left|E_{Max}(V)\right| = \frac{2\phi_c}{W_o}\sqrt{1 - V/\phi_c} \qquad (3.14)$$

3.7 Calculation of Reverse Break down Voltage

Equation (3.14) indicates that the maximum field strength at the metallurgical junction increases with the reverse bias voltage (V negative). At some critical value of $V = -V_B$ $|E_{Max}|$ reaches impact ionization value E_B. At this electric field strength free electrons gain sufficient kinetic energy to break other electrons free from the valance bonds. This impact ionization field strength (E_B) depends on the magnitude of the energy band gap (between conduction and valance bands) of the semiconductor material and has a typical value of 2×10^5 V/cm for silicon. If the reverse bias voltage exceeds V_B impact ionization will release a large number of free carriers by avalanche multiplication process and the **p-n** junction will undergo "reverse break down" characterized by a large reverse current (from **n** to **p** side) flowing across the junction. Such large current quickly destroys the junction by over heating. Therefore, a **p-n** junction should never be operated at reverse break down voltage. The reverse break down voltage can be calculated as follows.

From (3.14) putting $\left|E_{Max}(V_B)\right| = E_B$ and $V = -V_B$

$$E_B = \frac{2\phi_c}{W_o}\sqrt{1 + V_B/\phi_c}$$

$$\text{OR } V_B = \frac{W_o^2 E_B^2}{4\phi_c} - \phi_c \approx \frac{W_o^2 E_B^2}{4\phi_c} \quad (\because \phi_c << V_B)$$

Substituting the expression of W_O from (11) in to the above equation

$$V_B = \frac{\in (N_a + N_d)}{2qN_aN_d} E_B^2 \tag{3.15}$$

3.8 Calculation of the Forward and Reverse Current Densities

3.8.1 Forward biased p-n junction equation

Application of external voltage not only changes the width of the space charge region (also called "depletion region") but also have very prominent effect on the excess minority carrier density distribution as shown in Figure (3.1)

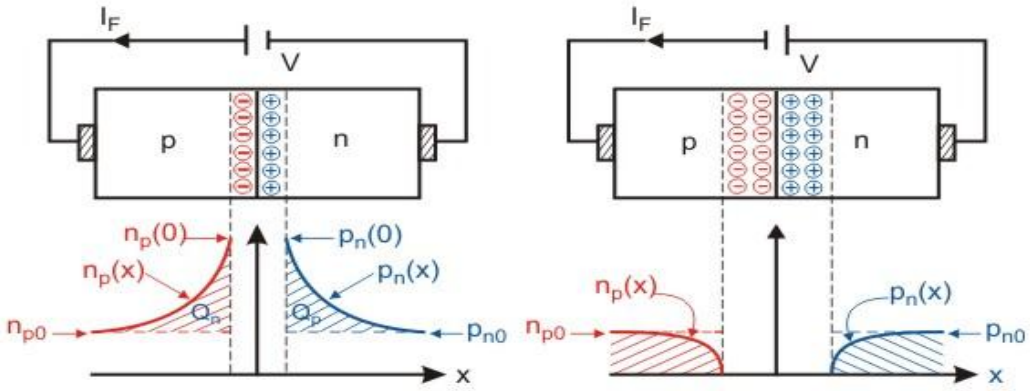

Figure (3.12) Excess minority carrier density distribution in a p-n junction (a) under forward bias condition; (b) under reverse bias condition.

A forward bias voltage lowers the potential barrier and allows a large number of carriers to change sides. It is known from the "law of the junction" that the

minority carrier density at the edge of the depletion region of a forward biased **p-n** junction is given by

$$\mathbf{p_n(o) = p_{no}\, e^{qv/KT}} \tag{3.16}$$

$$\mathbf{n_p(o) = n_{po}\, e^{qv/KT}} \tag{3.17}$$

Where $P_{n0}$and n_{p0} are thermal equilibrium minority carrier densities in the **p** side and the **n** side respectively and V is the applied voltage.

From basic semiconductor physics relationship

$$p_{no} = \frac{n_i^2}{N_d} \;\&\; n_{po} = \frac{n_i^2}{N_a} \tag{3.18}$$

Where $n_i$is the intrinsic carrier density in the semiconductor material .

Injected minority carriers recombine with majority carriers as they defuse further in the electrically neutral region of the semiconductor body. In steady state minority carrier density is exponentially distributed in distance from the junction on either side. i.e.

$$\mathbf{n_p(x) = n_p(o)e^{-|x|/L_n}} \tag{3.19}$$

$$\mathbf{p_n(x) = p_n(o)e^{-|x|/L_p}} \tag{3.20}$$

Where $L_n$and $L_p$are diffusion lengths of **n** and **p** type carriers in the **p** and the**n** type regions respectively.

Hatched portions of Figure (3.3) (a) represent stored excess minority carriers in the p and the n type regions respectively.

$$|Q_n| = q\left[n_p(o) - n_{po}\right]L_n \tag{3.21}$$

$$|Q_p| = q\left[p_n(o) - p_{no}\right]L_p \tag{3.22}$$

Now in steady state forward bias condition excess minority carrier distributions shown in Figure (3.3) (a) remain stationary which implies that the carriers lost per unit time by recombination must be replaced by forward current I_F

$$\text{i.e.} \qquad J_F = \left|\frac{dQ_p}{dt}\right| + \left|\frac{dQ_n}{dt}\right| \tag{3.23}$$

From basic semiconductor physics the recombination dynamics is given by

$$\frac{dQ_n}{dt} = -\frac{Q_n}{\tau_n} \text{ and } \frac{dQ_p}{dt} = -\frac{Q_p}{\tau_p} \tag{3.24}$$

Where τ_n an τ_p area carrier lifetimes of **n** and **p** type carriers in the **p** and the **n** type regions respectively.

Combining (3.23) and (3.24)

$$J_F = \frac{|Q_p|}{\tau_p} + \frac{|Q_n|}{\tau_n} = q\,n_i^2\left[\frac{L_n}{N_a\tau_n} + \frac{L_p}{N_d\tau_p}\right]\left(e^{\frac{qv}{KT}} - 1\right) \tag{3.25}$$

Equation (3.25) also holds for reverse bias condition i.e. when v is negative. For sufficient reverse bias the reverse saturation current density is given by.

$$J_s = q\,n_i^2\left[\frac{L_n}{N_a\tau_n} + \frac{L_p}{N_d\tau_p}\right] \tag{3.26}$$

$$\therefore \quad J_F = J_s\left(e^{qv/KT} - 1\right) \tag{3.27}$$

Equations (3.26) and (3.27) define the i-v characteristics of a junction diode under reverse and forward bias conditions respectively.

3.9 Turn on Behavior of a Power Diode

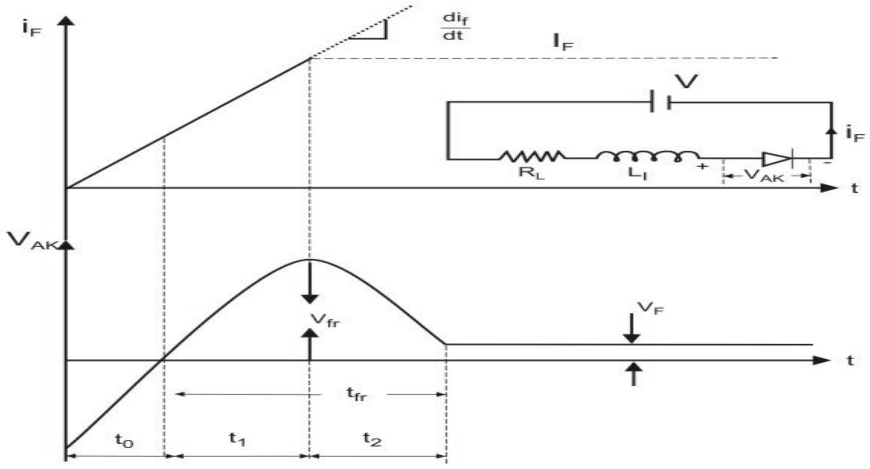

Figure (3.13) forward current and voltage waveforms of a Power Diode during Turn ON. Several physical mechanism as explained below takes place during Turn ON of a diode.

From time 0 to t_o growing forward current charges the depletion layer capacitance formed by the space charge of the drift region. The diode voltage increases gradually to the forward bias junction voltage V_F at which point the metallurgical junction $p^+ n^-$ becomes forward biased. Minority carrier densities in all the sections of the diode just reach their respective thermal equilibrium levels at this point.

Although the diode is forward biased after t_o, the forward voltage drop across the device keeps on increasing with the forward current for same more time. During this period the drift region offers significant resistance due to insufficient carrier injection. Stray inductance of the wafer and bonding wires, coupled with the forward dI_F/dt, also contributes to the increase in the forward voltage drop.

Finally after time t_o+t_1 resistance of the drift region starts decreasing due to conductivity modulation. Forward current also reaches its steady state value "I_F" and dI_F/dt becomes zero. As a result, the waveform of the forward voltage drop turns over and starts decreasing, reaching steady state value "V_F" in time t_2.

The peak voltage drop across the diode is called the forward recovery voltage and is a strong function of the forward dI_F/dt, the time interval t_1 is a function of the forward $dI_F/dt$with typical values in hundreds of nanoseconds. However, t_2 is more or less constant for a given diode with typical values less than 10 us. The time period t_1 + t_2 is often called the forward recover time (t_{fr}).

The next diagram explains the diode Turn on process.

3.10 Reverse Recovery characteristics of a power Diode

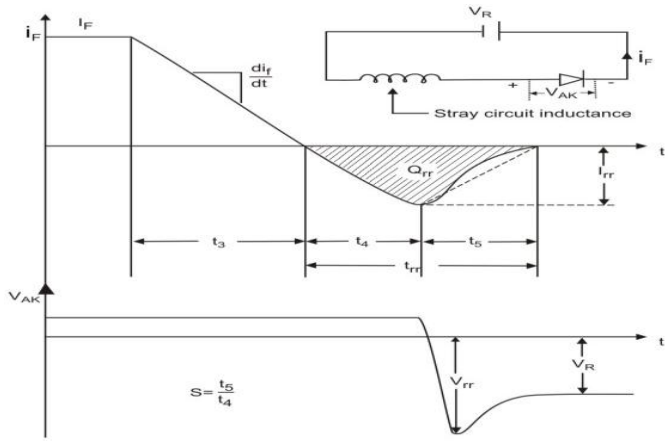

Figure (3.14) Reverse Recovery characteristics of a power Diode.

Conceptually the Turn off process of a diode can be through of as the reverse of the Turn on process. Excess minority carriers injected into the drift region during Turn on have to be removed before the diode can start blocking reverse voltage.

The reverse recovery current sweeps out excess carriers from the drift region. At the end of time period t_3 minority carrier density in the $\mathbf{p}^+$ and $\mathbf{n}^+$ regions are already at their thermal equilibrium level. However, there is still a large amount

of excess carriers trapped in the drift region which is then removed by the reverse recovery current during time period t_4. During this period minority carrier densities in the p^+ and n^+ regions do not change very much. At the end of t_4 too few carriers exist in the n^- drift region to support the reverse recovery current demanded by the stray circuit inductance.

Recovery current starts falling sharply while the reverse voltage across the device starts growing. Stay circuit inductance, coupled with large falling rate of the recovery current, can give rise to a peak reverse voltage (V_r) far in excess of the steady state blocking voltage (V_r).

With increase in the reverse voltage across the diode, the depletion layer starts spreading into the drift region. Minority carrier densities quickly attain their respective reverse bias profile in the p^+ and n^+ regions.

Even at the end of t_5 some trapped charges exist inside the drift regions which disappear by the process of recombination. Therefore, reverse recovery charge (Q_{rr}) is always less than the total amount of excess carriers stored in the drift region during Turn on. Next figure explains the carrier density variation with time during the Turn off process.

With reference ro Figure (3.5)

$$I_{rr} = \left|\frac{di_F}{dt}\right| t_4 = \left|\frac{di_F}{dt}\right| \frac{trr}{s+1} \tag{3.28}$$

$$Q_{rr} \approx \tfrac{1}{2} I_{rr} t_{rr} = \left|\frac{di_F}{dt}\right| \frac{trr}{2(s+1)} \tag{3.29}$$

$$t_{rr} = \sqrt{\frac{Qrr(1+s)}{|di_F/dt|}} \tag{3.30}$$

$$I_{rr} = \sqrt{\frac{2Qrr|di_F/dt|}{s+1}} \tag{3.31}$$

Now if the total charge stored in the drift region is Q_F at a steady forward current I_F then

$$I_F = \frac{dQ_F}{dt} = \frac{Q_F}{\tau} \quad \text{OR} \quad Q_F = \tau I_F \tag{3.32}$$

Where τ is the excess carrier life time in the drift region.

Now it has been argued earlier that $Q_{rr} \leq Q_F$ always.

Therefore for S $\angle\angle$1 $t_{rr} \angle \sqrt{\frac{2\tau I_F}{\left|\frac{di_F}{dt}\right|}}$ (3.33)

And $I_{rr} \angle \sqrt{2\tau I_F \left|\frac{di_F}{dt}\right|}$ (3.34)

Equations (3.33) and (3.34) indicate that both I_{rr} and t_{rr} increases with τ. I_{rr} increases with I_F and $\left|\frac{di_F}{dt}\right|$ while t_{rr} increases with I_F but decreases with $\left|\frac{di_F}{dt}\right|$.

3.11 Power loss due to reverse recovery:

With reference to Figure (3.4) energy loss per reverse recovery is given approximately by.

$$E_{rr} = \frac{1}{2} I_{rr} t_4 V_F + \frac{1}{2} I_{rr} t_5 V_R$$

$$= \frac{1}{2} I_{rr} t_{rr} \left[\frac{V_F + SV_R}{S+1}\right] = \frac{Q_{rr}}{S+1}[V_F + SV_R] \tag{3.35}$$

If the switching frequency is f_{sw} then reverse recovery power loss is

$$p_{rr} = E_{rr} f_{sw} = Q_{rr} f_{sw} \frac{V_F + s_{vr}}{S+1} \tag{3.36}$$

3.12 Schottky Diodes

3.12.1 Construction and Operating Principle

A Schottky diode is formed by placing a thin film of metal, usually Aluminum in direct contact with a **n** type epitaxial layer grown on a n^+ type substrate. The metal film acts as the positive electrode (anode) while the n^+ substrate acts as the cathode. Another metal contact is placed on the n^+ cathode side for current collection. Fig. 2 shows the schematic structure of a Schottky diode.

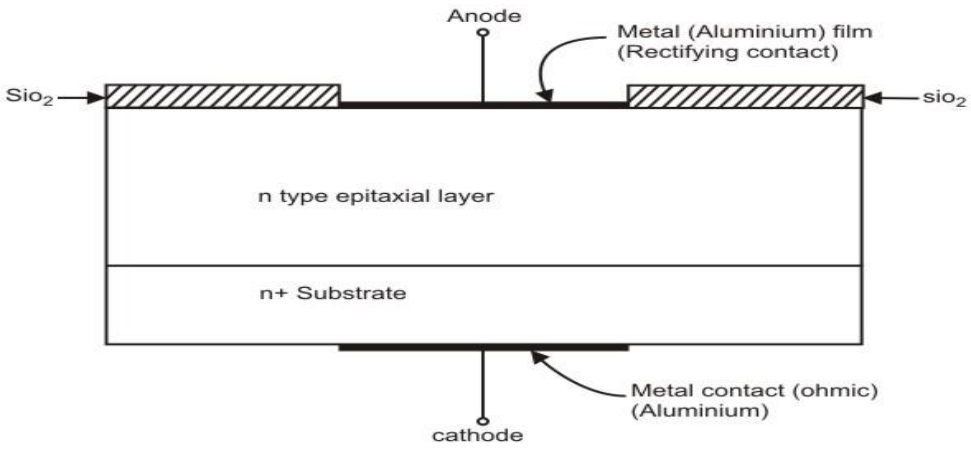

Figure (3.15) Schematic structure of a Schottky diode.

The insulating sio_2 layer helps reduce the surface electric field and improves reverse characteristics.

The metal semiconductor junction on the anode side has a rectifying property because the electrons in the semiconductor have higher absolute potential energy compared to the metal. So there will be a large flux of electrons flowing from the semiconductor to the metal across this interface. Consequently the metal will become negatively charged while the semiconductor positively charged and a depletion region similar to a **p-n** junction will be formed at this interface. However, the negative space charge in the metal comes from free electrons and not from movement of holes. This flow of electron will continue till the

electrostatic potential associated with the space charge stops further movement of electrons.

When a forward bias voltage (i.e, anode positive with respect to cathode) across this structure, it reduces the potential barrier and makes it easier

for electrons to cross over. Biasing the metal negative with respect to the semiconductor has the opposite effect. Thus, the metal semiconductor interface exhibits a rectifying properly.

The same rectifying properly is not observed at the cathode metal interface. The cathode has a much larger doping density. Thus the depletion region that is formed is very narrow and the electric field very large. Under these circumstances, the electrons move very easily across the interface using a quantum mechanical effect called “Tunneling” under the influence of small applied voltage. That is why the cathode-metal interface is an ohmic contact and not a rectifying contact.

3.12.2 Characteristics of Schottky diodes

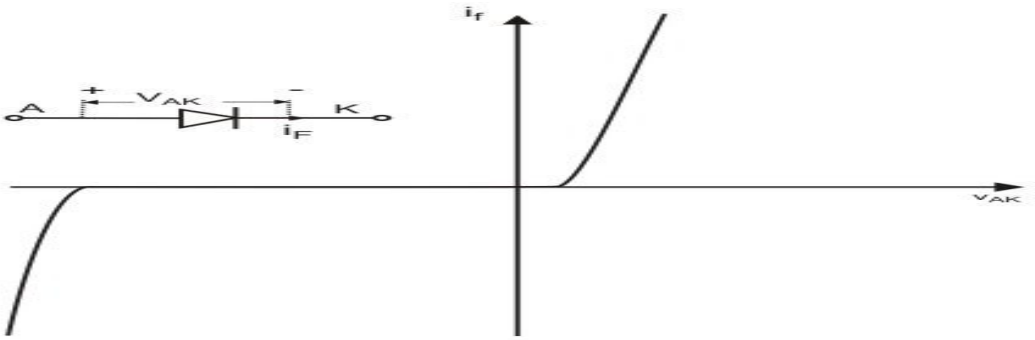

Figure (3.16) I- V characteristic of a Schottky diode.

The Forward bias i-v characteristic of a Schottky diode is similar to that of a p-n junction diode. However, these diodes are designed to have lower forward voltage drop, the difference being 0.3-04V for the same forward current density.

In the reverse direction, a Schottky diode has much larger reverse leakage current compared to a **p-n** junction diode. The break down voltage is also considerably lower (<200v). After break down it exhibits resistance like characteristics.

Schottky diodes have much shorter switching times. Being a majority carrier device, no stored charge needs to be removed during Turn off. Consequently, there will be no reverse current corresponding to removal of minority carriers. Reverse current associated with the growth of the depletion layer charge in reverse bias will flow. But this is much smaller compared to a **p-n** junction diode (< 5%). Reverse recovery time (a few hundreds of nano seconds) and energy loss are also much smaller. During Turn on forward recovery voltage V_{fr} is negligible due to much larger doping density and smaller width of the n type epitaxial layer. Voltage overshoot due to parasitic inductance may, however, be observed at largedI_F/dt.

3.13 solar cells

Solar cells are photovoltaic (PV) device that convert the electromagnetic radiation (i.e. light, including infrared, visible, and ultraviolet) from the sun in to utilizable electrical energy. The conversion process can be considered as a sequence of the four basic steps. The first step is the light absorption, which causes a transition from a ground state to an excited state in a material (the absorber of light). The second steps the conversion of the excited state in to at least one free electron, hole pair (photo generation). The third step is the presence of a force such that the produced free electrons travel in one direction and the produced free hole travel in the opposite direction. This causes charge separation. Then it is important the last step requires completion of an external circuit by the combination of returning electrons with hole to return the absorber to the ground state (non-equilibrium open system).

3.13.1 The Efficiency of a solar cell

Figure (3.13) shows a plot of the possible J-V operating points, called the "light" J-V characteristic of the PV cell. The points labeled J_{sc} and V_{oc} represent, respectively the extreme cases of no voltage produced between the opposite ends of the device (i-e. the illuminated the cell is at short – circuit condition) and of no current flowing between the two ends (i-e- illuminated cell is open – circuit condition).

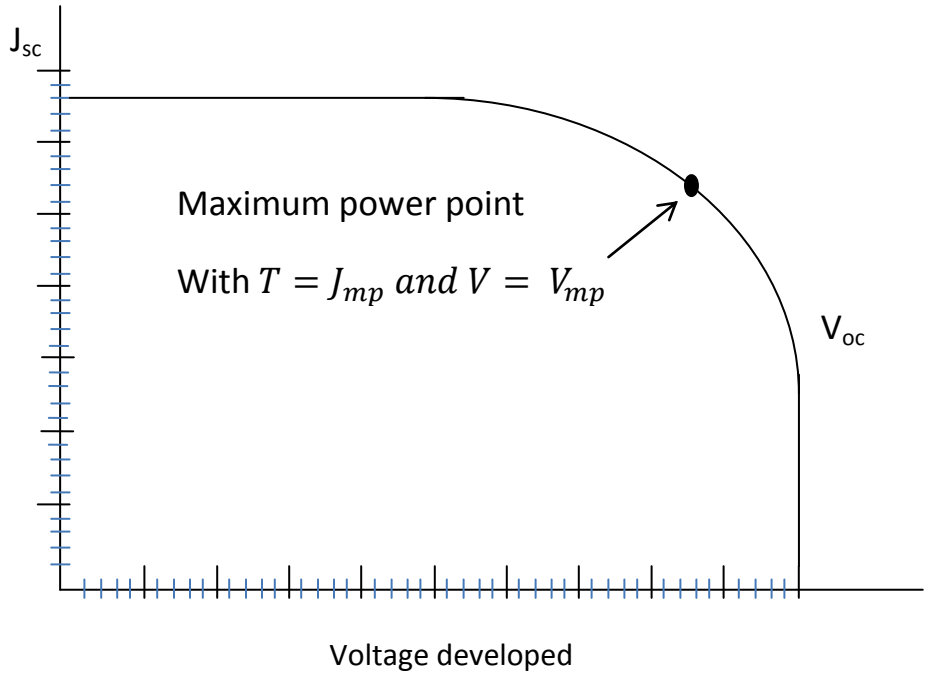

Figure (3.17) typical (I-V characteristic of photovoltaic structure under illumination)

It must be noted that the power output (defined) as J.V product at any point) has its highest value at the maximum power point corresponding to the values of J_{mp} and V_{mp} .

The definition of these quantities helps define the thermodynamic efficiency η (eta) of the PV conversion process in terms of the input power P_{input} as:

$$\eta = J_{mp}.V_{mp}/P \qquad (3..37)$$

It can be seen from figure (3.3) that's an ideal shaped J-V curve would be rectangular and would deliver a constant current density I_{sc} up to the open – circuit voltage V_{oc}.

A term called the fill factor FF is hence used to measure how close a given characteristic is to conforming to this ideal rectangular J-V shape the fill factor, by definition, is ≤ 1.

The efficiency of a PV device can now be defined in terms of the fill factor as:

$$\eta = FF.J_{sc}\,.V_{oc}/pinput \qquad (3.38)$$

It is evident that the two major parameters governing efficiencies in solar cells are short – circuit current density J_{sc} and open – circuit V_{oc}. Consequently, improvements to PV conversion efficiencies involve increasing J_{sc} of V_{oc} values or both [68].

3.14 Photovoltaic characterizations

3.14.1 Real Solar Cells

For a real solar cell, the effect of parallel resistance R_{sh} (shunt resistance due to leakage current, e.g. by local shorts of the solar cell) and serial resistance R_s (due to ohmic loss) must be considered.

$$In\left(\frac{I+I_L}{I_s}-\frac{V-IR_s}{I_sR_{sh}}+1\right)=\frac{e}{kT}(V-IR_s) \qquad (3..39)$$

The serial resistance affects the filling factor more strongly than the shunt resistance (Fig (3.14).

$$I = I_s \left[\exp\left(\frac{e(V - IR_s}{kT}\right) - 1\right] - I_L. \qquad (3.40)$$

In the example of Fig 3.14, a serial resistance of 5Ω reduces the filling factor by a factor of about four [69].

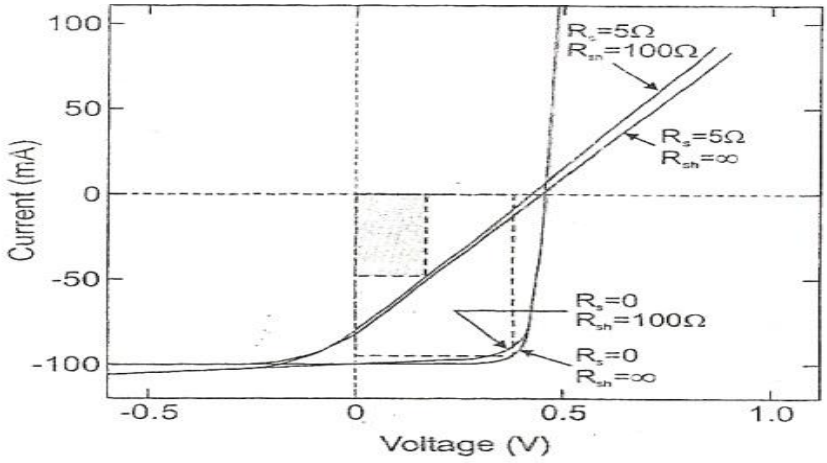

Fig (3.18) I-V characteristics of a solar cell considering shunt and series resistances R and R_h, respectively. The efficiency of the real cell (shaded power rectangle) is less than 30% of that of the ideal cell.

3.14.2 Ideal conversion Efficiency

The conventional solar cells, typically a p-n Junction, have a single band gapE_g. When the cell is exposed to the solar spectrum, a photon with energy greater than $E_g$makes no contribution to the cell output (neglecting phonon assisted absorption). A photon with energy with energy greater than $E_g$contributes an electric charge to the cell output, and the excess energy over $E_g$is wasted as heat. To derive the ideal conversion efficiency.

We shall consider the energy band of the semiconductor used. The solar cell is assumed to have ideal diode I-V characteristics. The equivalent circuit is shown in fig (3.15)

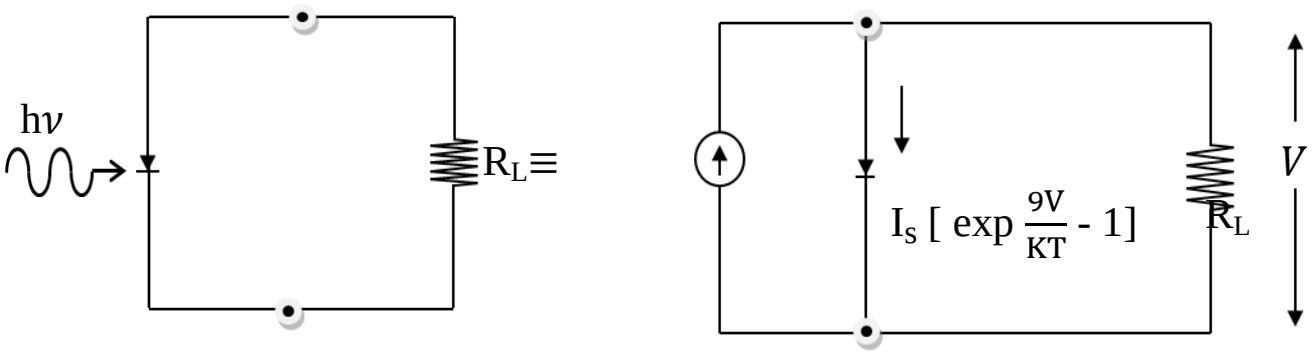

Figure (3.19) Idealized equivalent circuit of solar cell under illumination.

Where a constant – current source of photo current is in parallel with the Junction. The source I_L results from the excitation of excess carriers by solar radiation, I_s is the diode saturation current and R_s is the load resistance. To obtain the photocurrent I_L, need to integrate the total area under the graph shown figure (3.16)

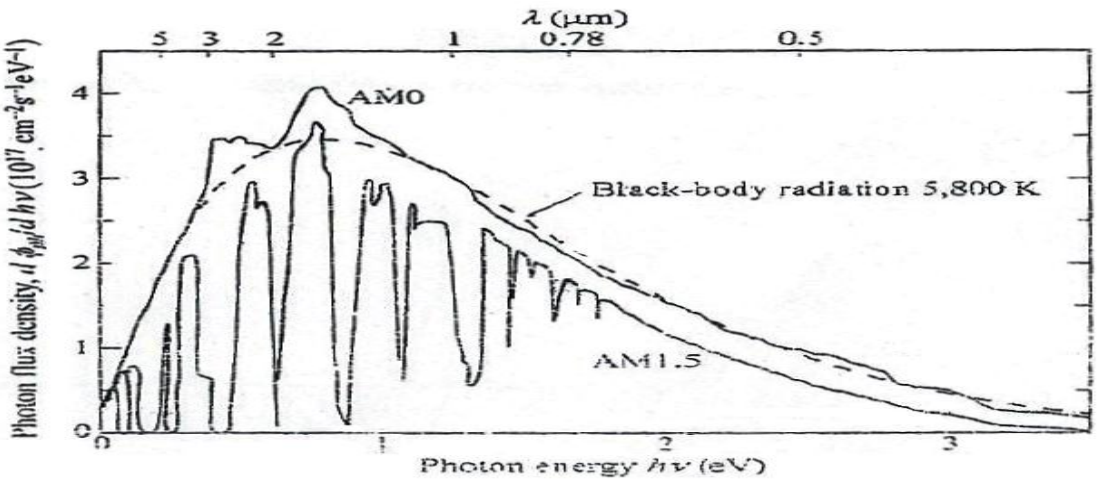

Fig (3.20) I-V Characteristics of solar cell under illumination. Determination of illuminated power output is indicated

$$That\ is\ , I_L\ (E_a)\ =\ Aq \int_{h\upsilon=Eg}^{\infty} \frac{d\ \phi\ ph}{dh\upsilon} d(h\upsilon) \qquad (3..41)$$

The result is show in fig (3.17) as a function of the band gap of the semiconductor. For the photo current consideration, the smaller band gap the better because more photons are collected.

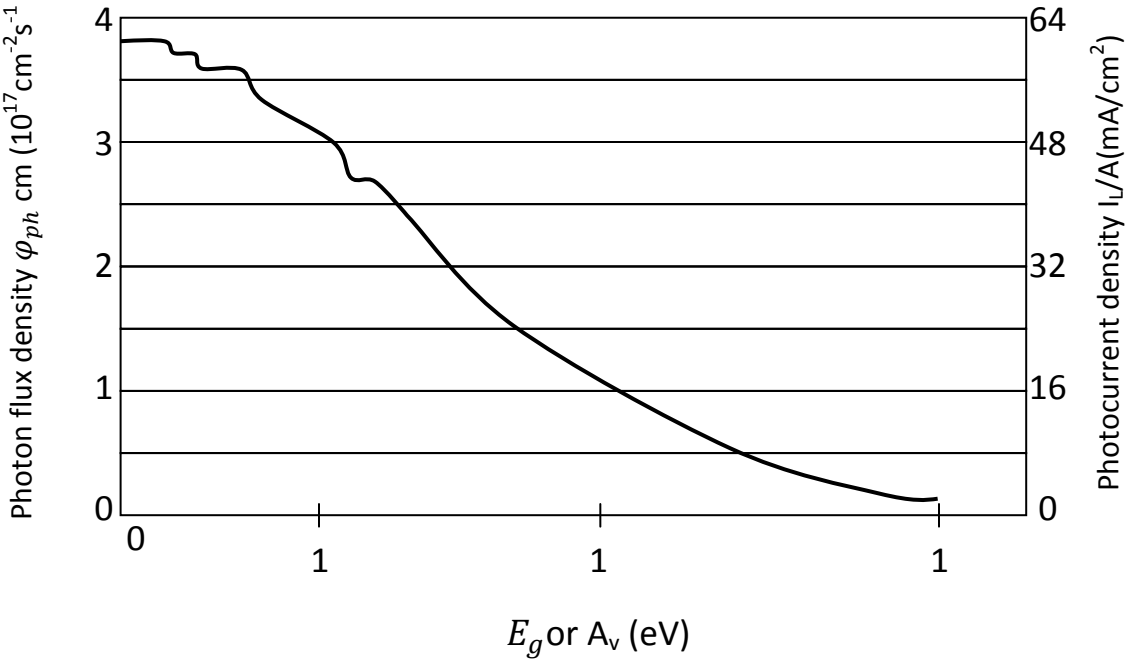

Fig (3.21) Total number of photons in the solar spectrum (of AMI-5) above an energy value. Contributing to the maximum photo current for a solar cell made with specific E_g.

The total I-V characteristics of such a device under illumination is simply a summation of the dark current and the photocurrent, given as

$$I = I_s \left[\exp\left(\frac{qV}{KT}\right) - 1\right] - I_L \qquad (3,42)$$

From equation (3.42) one obtains the open – circuit voltage by setting I= 0:

$$V_{oc} = \frac{KT}{q} Ln \left(\frac{I_L}{I_s} + 1\right) \approx \frac{KT}{q} \ln\left(\frac{I_L}{I_s}\right) \qquad (3.43)$$

Hence for a given I_L, the open-circuit voltage increases logarithmically with decreasing saturation current I_s. For a regular p-n Junction, the ideal saturation current is given by:

$$I_s = Aq\, N_c\, N_v \left[\frac{1}{N_A}\sqrt{\frac{D_n}{\zeta_n}} + \frac{1}{N_D}\sqrt{\frac{D_p}{\zeta_p}}\right] \exp\left[\frac{-Eg}{KT}\right] \qquad (3.44)$$

As seen, I_S decreases exponentially withE_g. So the obtain a large V_{oc}, a largeE_g. Is required.

Qualitatively, we know the maximum V_{oc} is the built – in potential of the Junction, and the maximum built- in potential is close to the energy gap. A plot of equation (3.42) is given in figure (3.18).

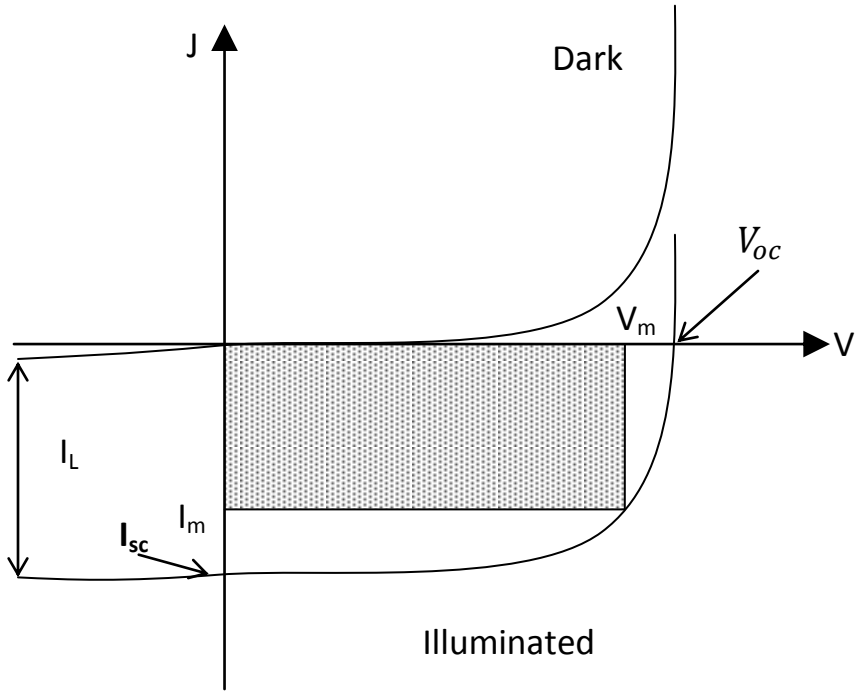

Fig (3.22) I-V Characteristics of solar cell under illumination. Determination of illuminated power output is indicated

The curve passes through the fourth guardant and, therefore, power can be extracted from the device to a load. By properly choosing a load, close to 80% of the product I_{sc} V_{oc} can be extracted.

Here I_{sc} is the short- circuit current which is equal to the photocurrent derived. The shaded area is the maximum power output. We also define in Fig (3,19) the quantities $I_m$and $V_m$that correspond to the current and voltage. For the maximum power output($P_m = I_m V_m$)

To derive the maximum-power operating point, the output power is given by:

$$P = IV = I_S V[\exp\left(\frac{qV}{KT}\right) - 1] - I_L V \qquad (3.45)$$

The condition for maximum power can be obtained when

$$dp/_{dv} = 0$$

Or :

$$I_m = I_s \beta V_m \exp(\beta V_m) \approx I_L(1 - \frac{1}{\beta V_m}) \qquad (3.46)$$

$$V_m = \frac{1}{\beta}\ln\left[\frac{I_L/I_S + 1}{1 + \beta V_m}\right] \approx V_{oc} - \frac{1}{\beta}\ln(1 + \beta V_m) \qquad (3.47)$$

Where β=q/kT .the maximum power output P_m is then

$$P_m = I_m V_m = FF I_{sc} V_{oc} \approx I_L[V_{oo} - \frac{1}{\beta}\ln(1 + \beta V_m) \qquad (3.48)$$

Where the full factor FF measures the sharpness of the curve and is defined as:

$$FF \equiv \frac{I_m V_m}{I_{sc} V_{oc}} \qquad (3.49)$$

In practice a good fill factor as around 0.8.

The ideal conversion efficiency is the ratio of the maximum power output to the incident power P_{in}

$$\eta = \frac{P_m}{P_{in}} = \frac{I_m V_m}{P_{in}} = \frac{V_m^2 I_s \left(\frac{q}{KT}\right) exp(qV_m/KT)}{Pin} \qquad (3.50)$$

Theoretically, the ideal efficiency can be calculated. We have shown that the photocurrent increases with smaller E_g. On the other hand, the voltage increases with E_g. By having a small saturation current. So to maximize the power, there exists an optimum value for the band gap E_g. Furthermore, by using the ideal saturation current of E_g (3.43) in relation to E_g, the theoretical maximum conversion efficiency can be calculated [67].

Chapter four

Literature Review

In this chapter some attempts to fabricate ZnO and CuO a P-N junction and their performance are investigated. The purpose of the present works to fabricate ZnO/CuO thin film diode by electrodepositing, and to investigate the effect of CuO and ZnO layers on their optical properties. In addition to I-V characteristics, Structural, morphological and absorption measurement of CuO/ZnO heterojunction were studied by using x-ray diffraction, SEM.. In the other hand CuO and ZnO films were deposited using a galvanostatic method.

4.1 Fabrication and characterization of copper oxide –zinc oxide solar cells prepared by electrodeposition [69].

In this paper the Cu_2O and CuO layers were prepared on pre-cleaned indium tin oxide (ITO) glass plate by electro deposition using platinum counter electrode, Copper (11) sulfate ($CuSO_4$,0.4 mol L^{-1} ,Wako 97.5%) and L-lactic acid (3 mol L^{-1} ,Wako) were dissolved into distilled water. Electrolyte pH was adjusted to 12.5 by adding NaOH. The electrolyte temperature was kept at 65 ^{0}C during electrodepositing. Preparation of Cu_2O layers were carried out at current density at 1.5 mA cm^{-2} and quantity of electric charge of 4.0 C cm^{-2}. ZnO layers were also galvanostatically pared at current density at 5 and 10 $mAcm^{-2}$ from 8mM aqueous solution of Zn $(NO_3)_2$ on Cu_2O layers. Electric charge was adjusted 1.5 C cm^{-2} .Gold (Au) metal contacts were vacuum deposited as top electrodes. Structures were denoted as ITO or FTO/ZnO/Cu_2O or Cu_2O/Au. Current density-voltage (J-V) characteristics (Hokuto Denko, HSV-110)

Of the solar cells were measured both in the dark and under illumination at 100mW cm^{-2} by using an AM1.5 solar simulator (San-ei Electric, XES-301S). The solar cells were illuminated through the side of the ITO substrates, and the

illuminated area was 0.16 cm^2.Optical absorption of the solar cells was investigated by means of UV visible spectroscopy (Jasco, V-670). The incident photon to current conversion efficiency (IPCE) of solar cells of investigated (Peccell technologies, PEC-S20). The microstructures of the copper oxide were investigated by X-ray diffract meter (XRD, Philips, X' Pert-MPD System) with CuKα radiation operating at40KVand 40 mA, and scanning electron microscope (SEM) operating at 15KV (Jeol, JEM-6380).

4.1.1 Results and Discussion

J-V characteristics of ZnO/Cu_2O structure under illumination at 100mW cm^{-2} by using an AM 1.5 solar simulator. The photocurrent was observed under illumination and the CuO/ZnO structure shoed characteristic curves with short-circuits current and open-circuit voltage. A solar cell with FTO/ZnO/Cu_2O structure provided power conversion efficiency (η) of 0.25%, fill factor (FF) of 0.33, and short-circuit current density (J_{sc}) of 2.7 mA cm^{-2} and open-circuit voltage (V_{oc}) of 0.28V. Solar cells with ITO/ZnO (mA cm^{-2}) /Cu_2O structure provided power conversion efficiency (η) 7.3×10^{-3}%, fill factor (FF) 0.26, and short-circuit current density (J_{sc}) of 0.45mA$cm^{-2}$and open-circuit voltage (0.063) V. Solar cell with ITO/ZnO(5mAcm^{-2}) /Cu_2O also provided power conversion efficiency (η) 6.9×10^{-2} %, fill factor (FF) 0.26, and (J_{sc}) 1.38mAcm^{-2}, and (V_{oc}) 0.20V. Solar cell with ITO/ZnO (5mAcm^{-2}) also provided power conversion efficiency(η) 1×10^{-5}%,fill factor (FF) of 0.25, and (J_{sc}) of 2.4×10^{-3} mAcm^{-2}, and open-circuit voltage (V_{oc}) 0.017 [70].

4.1.2 Fabrication and Evaluation of CuO/ZnO Heterostructures for Photoelectric Conversion

Solar cell with cuprous oxide (CuO) and zinc oxide (ZnO) heterojuntion fabricated on indium tin oxide –glass were studied. CuO and ZnO films were

deposited using a galvanostatic method. Structural, morphological and optoelectronic properties of the CuO/ZnO heterojuntion were studied by using X-ray diffraction, atomic force microscopy and light current-voltage characteristics.

Silicon is used as the semiconductor material for conventional solar cells, but silicon is expensive and cost reduction of the solar cells is one of the most important issues. Oxide semiconductors are one of the alternatives to silicon solar cells, and copper oxide such as CuO and Cu_2O are one of the candidate materials. The features of copper oxide semiconductors are relatively higher optical absorption, low cost of raw materials and non-toxic. CuO and Cu_2O are p-type semiconductors with band gap energies of 1.5 eV and 2.0 eV, respectively, which are close to the ideal energy gap of 1.4 eV for solar cells and allows for good solar spectral absorption. Zinc oxide (ZnO) is an n-type semiconductor with a wide band gap of ~3.37 eV, which can be applied to solar cells .The highest efficiency of ~2% for Cu_2O solar cells has been obtained by using the high temperature annealing method.

4.1.3 Experimental Procedures

The purpose of the present work is to fabricate and characterize solar cells with CuO/ZnO structures. CuO layer were prepared on pre-cleaned indium tin oxide (ITO) glass plate by electro deposition using platinum as counter electrode. Copper (11) sulfate ($CuSO_4$, 0.4 mol/L, Wako97.5%) and l-lactic acid (3 mol/L, wako) were dissolved into distilled water. PH of the electrolyte solution was adjusted to 12.5 by adding NaHO. The temperature of electrolyte solution was kept at 65^0C during electro deposition. Preparation of CuO layers were carried out at voltage of +0.70Vand quantity of electric charge of 2.2C cm^{-2}. After the deposition, the sample was rinsed with water and transferred in to the ZnO electro deposition bath. ZnO layers were galvanostatically electro-deposited

from 0.025 M aqueous solution of Zn (NO_3) on the ITO/CuO substrate. The sample thickness ranged between 1and 2μm depending on the deposition time and current. Finally, the substrates were rinsed with water, dried with air and quickly transferred into a thermal evaporator for the vacuum deposition of the aluminum (Al) back contact, Structure of heterojunction solar cells were denoted as ITO/CuO/ZnO/Al,

Current density- voltage (J-V) characteristics (Hokuto Denko Corp., HSV-100) of the solar cells were measured using potentiostat (Hokuto Denko,HSV-100) in the dark and under illumination at 100 mW/cm^2 by using an AM 1.5 solar simulator(San-ei Electric, XES-301S). The solar cells were illuminated through the side of the ITO substrate, and the illuminated area was 0.16 cm^2. Optical absorption of the solar cells was investigated by means of UV visible spectroscopy (Hitachi, Ltd., U-4100). Microstructures of the copper oxide were investigated by X-ray diffractometer (XRD, PHILIPS X' Pert-MPD System) with CuKα radiation operating at 40 KV and 40mA. Transmission electron microscopy (TEM, Hitachi H-8100, 200 kV operating voltage) was also carried out for nanostructure analysis.

4.1.4 Results and Discussion

Thicknesses of CuO were ~1μm and ~2μm for 5 min and 10min, respectively. A solar cell with a CuO/ZnO structure provided power conversion efficiency (η) of 1.1×10^{-4} %, fill factor (FF) of 0.25, and short-circuit current density (J_{sc}) of 1.9mAcm^{-2} and open-circuit voltage (V_{oc}) of 2.8×10^{-4}. Thicknesses of CuO~2μm for 10min, solar cell structure provided power conversion efficiency (η) $1.1x10^{-7}$, fill factor (FF) 0.25, and short-circuit current (J_{sc}) 0.017 mA/cm^{-2} and open –circuit voltage (V_{oc}) of 1.8×10^{-4} V. The ZnO/CuO (5 min) structure provided power conversion efficiency 9.9×10^{-5} , fill factor (FF) of 0.28, and short-circuit current density (J_{sc}) 0.43, and open-

circuit voltage (V_{oc}) 8.2×10^{-4}V. The photocurrent was observed under illumination and CuO/ZnO structure showed characteristic curves with short-circuits current and open-circuit voltage. The CuO and ZnO thin films show high optical absorption in the range of 400nm and 700nm.

Transmittance spectrum of 100nm thick CuO film, deposited on ITO, the optical absorption coefficients (α) of this film was determined from the spectral transmittance using the next equation $\alpha = \frac{1}{d} .\ln(\frac{1}{T})$. Where d is the film thickness and T is the transmittance. For determination of the optical band gap energy (E_g), the method based on the relation of $\alpha h\upsilon = A\ (h\upsilon - E_g)^{n/2}$ was used, where n is a number that depends on the nature of the transition. In this case, its value was found to be 1, which corresponds to direct band to band transition.

In this research we use a tauc plot, which shows $(\alpha h\upsilon)^2$ versus hυ for the CuO film. The intersection of the straight line with hυ-exis determines the optical band gap energy E_g. It was found to be ~ 2.1eV which is lower than the ideal band gap of the CuO crystal. Because of the small band gap energy, the open-circuit voltage would be low [71].

4.2 Current-Voltage Characteristics of P-CuO/n-ZnO :Sn Solar Cell

In this study p-CuO/n-ZnO:Sn heterojunction solar cell has been fabricated on glass substrate in steps using Edwards AUTO 306vacuum coater system. Copper oxide has energy band gap of the range 1.21-2.1eV while tin doped zinc oxide (TZO) has good transmittance properties. A solar cell with thickness of 250nm of p-type copper oxide and thickness of 140nm of n-type TZO with 2% tin doping has been made. Current-Voltage (I-V) measurement has been done on the solar cell using Keithley 2400sourcemeter interfaced with the computer running labview program. Diode properties determined from I-V measurements are open circuit voltage (V_{oc}), short circuit current (I_{sc}), fill factor

(FF), maximum current output (I_m), and maximum voltage output (V_m), and conversion efficiency (η). The solar cell had V_{oc} of 480 mV, I_{sc} of 326.8mA, FF=0.63 and η=0.232%.

4.2.1 Experimental Procedure

The process of fabrication the solar cell was done in stages using Edwards AUTO 306 vacuum coater system. Silver paste acting as the back contact electrode was applies on a clean glass substrate measuring 70mm×27mm. The glass slide was wrapped with strips of aluminum foil 20mm from both ends so as to mask the edges and parts of silver layer film deposition. The glass slide was mounted on revolving substrate holder of the vacuum coater. Then 250nm thick CuO was deposited on the glass slide at room temperature by reactive dc magnetron sputtering method at oxygen flow of 5sccm. Argon was used as the sputtering gas and oxygen as the reacting gas. CuO film was deposited at chamber pressure of 9×10^{-3} mbars, argon flow of 20sccm and power of 200W.

Then a 140 nm thick TZO was deposited on CuO layer by reactive evaporation technique at temperature of 750^0C, oxygen flow of 20sccm and base pressure of 3×10^{-5}mbars. Current supplied to the molybdenum boat was 3.5A.The film deposited was doped at 2% tin concentration. Temperature was monitored using digital thermometer attached to the backside of molybdenum boat. A P-N junction of CuO-ZnO:Sn was denoted as Glass Substrate/Ag back contact/CuO/ZnO:Sn Solar Cell.

4.2.2 The Result and Discussion

The Diode characteristics investigated for the fabricated solar cell are open –circuit voltage (V_{oc}), short-circuit current (I_{sc}), fill factor (FF), maximum-current output (I_m), maximum-voltage output (V_m), and conversion (η). Fill

factor and conversion efficiency are obtained using the diode parameters as shown in equations 1and 2 below.

$$FF = \frac{I_m V_m}{I_{sc} V_{oc}} \tag{4.1}$$

$$\eta = \frac{I_m V_m}{P_{in}} \times 100 \tag{4.2}$$

Where V_{oc} is open-circuit voltage, I_{sc} short circuit-current, FF is fill factor, I_m maximum current output, V_m maximum voltage output, η conversion efficiency and P_{in} is power of photons incident on solar cell.

Diode properties of the solar cells were determined from measurements of current and voltage generated across the solar cell using four point probe system by use of Keithley 2400sourcemeter interfaced with a computer running labview program. The measurement was done with 100W bulb radiating light at power of 640W/m^2 and temperature of 25^{0}C. The power of light from the bulb was measured by a pyranometer. The bulb-solar cell separation distance was 15cm.The lab view program was such that a voltage of 0.8Vwas sourced from Keithley source meter to the solar cell and then current across it measured. The appropriate formulas were fitted into the program enabling it to automatically plot current versus voltage graph and determine V_{oc} ,I_{sc} ,I_m ,V_m and η for the solar cell.

4.2.3 Conclusion

A solar cell with silver back contact, n-type TZO window layer and p-type CuO absorber layer was fabricated in stages using Edwards AUTO306 vacuum coater system. I-V characteristics were measured using Keithley 2400sourcemeter interfaced with computer running lab view program. The solar cell had V_{oc} of 480mV, I_{sc} of 0.182mA, FF of 0.63 and efficiency of 0.232%.

The values of V_{oc} and fill factor obtained are higher than those of other solar cells like $CuSe_2$, CIGS and SIGS/ZnO whose values of V_{oc} and fill factor are 450mV and 0.62 respectively but with higher efficiency of 11%. The low efficiency may be attributed to surface reflections of incident photons leaving less radiation for conversion to electricity. Heating also decreases efficiency because at higher temperatures, conductivity decreases. More so series resistance of the cell due to non-ohmic contacts inhibits the flow of electrons. This decreases V_{oc} and makes current of the I-V curve fall slowly. Even though the efficiency of the solar cell fabricated was low, the availability and low cost of the materials makes it relatively affordable as compared to other cell devices like CIGS based cells whose materials are very expensive and not easily available [72].

4.3 Fabrication and Characterization of CuO/ZnO Solar Cells

In this study cuprous oxide (CuO) and zinc oxide (ZnO) heterojunction solar cells fabricated on indium tin oxide –coated glass were studied. CuO and ZnO films were deposited using a galvanostatic method. The purpose of the present work is to fabricate and characterize solar cells with CuO/ZnO structures. The band gab energy of CuO is ~1.5eV, which is closer to the ideal band gap of 1.4eV. Zinc oxide (ZnO) is an n-type semiconductor with a wide band gap of ~3.37eV, which can be applied to solar cells. Structural, morphological and optoelectronic properties of the CuO/ZnO heterojunction were studied by using X-ray diffraction, atomic force microscopy and light current-voltage characteristics.

4. 3.1Experimental Procedures

CuO layers were prepared on per-cleaned indium tin oxide (ITO) glass plate by electro deposition using platinum as counter electrode. Copper (II)

sulfate ($CuSO_4$, 0.4 mol /L, Wako 97.5%) and 1-lactic acid (3mol/, Wako) were dissolved into distilled water. pH of the electrolyte solution was adjusted to 12.5 by adding NaOH. The temperature of electrolyte solution was kept at 65^0C during electro deposition. Preparation of CuO layers were carried out at voltages of +0.70V and quantity of electric charge of 2.2C cm^{-2}. After the deposition, the sample was rinsed with water and transferred into the ZnO electro deposition bath. ZnO layers were galvanostatically electro-deposited from 0.025 M aqueous solution of Zn (NO_3) on the ITO/CuO substrate. The sample thickness ranged between 1and 2 µm depending on the deposition time and current. Finally, the substrates were rinsed with water, dried with air and quickly transferred into a thermal evaporator for the vacuum deposition of the aluminum (Al) back contact. Structure of heterojunction solar cells were denoted as ITO/CuO/ZnO/Al,

Current density- voltage (J-V) characteristics (Hokuto Denko Corp, HSV-100) of the solar cells were measured both in the dark and under illumination at 100 mW/cm^2 by using an AM 1.5 solar simulator (San-ei Electric, XES-301S). The solar cells were illuminated through the side of the ITO substrate, and illuminated area was $0.16cm^2$. Optical absorption of the solar cells was investigated by means of U V visible spectroscopy (Hitachi, Ltd; U-4100). Microstructures of the copper oxides were investigated by X-Ray diffractometer (XRD, PHILIPS X' P X' Pert-MPD System) with CuKα radiation operating at 40KV and 40mA.

4.3.2 Results and Discussion

Thicknesses of CuO were ~1µm and~2µm for 5min and10 min, respectively. A solar cell with a CuO/ZnO structure provided power conversion efficiency (η) of 1.1×10^{-4}%, fill factor (FF) of 0.25, short-circuit current density (J_{sc}) of 1.6 $mAcm^{-2}$ and open-circuit voltage (V_{oc}) of 2.8×10^{-4}V. The

photocurrent was observed under illumination, and the CuO/ZnO structures showed characteristic curves with short-circuit current and open-circuit voltage. The CuO and ZnO thin films show high optical absorption in the range of 400nm and 800nm. Also Thicknesses of ~2μm for 10 min (η) 1.1×10^{-7}%, fill factor (FF) 0.25, short-circuit current density (J_{sc}) 0.017mAcm^2, and open-circuit voltage (V_{oc}) of 0.18mV.Transmittance spectrum of 100nm of thick CuO film, deposited on ITO, is presented from this spectrum, the optical absorption coefficients (α) of this film was determined from the spectral transmittance using the next equation α=1/d.ln (1/T). Where d is the film thickness and T is transmittance. For determination of the optical band gap energy (E_g), the method based on the relation of $\alpha h\upsilon=A\ (h\nu = E_g)^{n/2}$ was used, where n is a number that depends on the nature of the transition. In this case, its value was found to be 1, which corresponds to direct band to band transition.

Use a Tauc plot, which shows $(\alpha h\nu)^2$ versus hνfor the CuO film. The intersection of the straight line with the hν-axis determines the optical band gap energy E_g. It was found to be ~2.1eV which is lower than the ideal band gap of the CuO crystal. Because of the small band gap energy, the open-circuit voltage would be low. Diffraction peaks corresponding to CuO and ZnO are observed in thin film, which consisted of cupric phase with monoclinic system (space group of C2/c and lattice parameter of a=0.4653 nm, b=0.3410 nm, c=0.5018 nm, $\beta=99.481^0$). The particle size was estimated using Scherer's equation; $D=0.9\lambda/B\cos\theta$, where λ, B, and θ represent the

Wavelength of the X-ray source, the full width at half maximum (FWHM), and the Bragg angle, respectively. The crystallite size of CuO and ZnO were determined to be 49.0nm and 82.0nm, respectively. Lattice constant of CuO and ZnO were obtains and comparing with reported value. From the lattice constant, the crystal structures of CuO and ZnO have some crystal distortions.

To increase the efficiency of the CuO/ZnO solar cells, small grain size of ZnO and higher crystalline of CuO would be necessary [73].

Energy level diagram of the CuO/ZnO solar cell was showed. Previously reported values were used for the energy levels. It has been reported that V_{oc} is nearly proportional to the band gap of the semiconductors, and control of the energy level is important to increase efficiency. Compared to silicon with an indirect transition band structure, CuO with a direct transition band structure is more suitable for the optical absorption property. In addition, the ultrathin film of the CuO layers could provide efficient charge injection because of the optical absorption. In the present work, microstructures of CuO and ZnO thin film were found to have some crystal distortion, which would result in the reduction of electrical transport. If the crystal qualities of the CuO and ZnO thin films are increased, V_{oc} would be improved.

4.3.3 Conclusion

ITO/CuO/ZnO/Al solar cells were produced and characterized which provided ηof 1.1×10^{-4}%, FF of 0.25, J_{sc} of 1.6 $mAcm^{-2}$ and V_{oc} of 2.8×10^{-4} V. The CuO/ZnO structure showed high optical absorption in the range of 400 nm and 800 nm, and the E_g of CuO was found to be ~1.2 eV from the Tauc plot which is smaller than that of the ideal band gap of the CuO crystal and the open-circuit voltage would be decreased. A crystallite size of CuO was determined to be 49.0 nm, and higher crystalline of CuO would increase the efficiency of the CuO/ZnO solar cells. The energy level of the present solar cell was proposed, and separated holes could transfer from the valence band of the CuO to the ITO, and separated electrons could transfer from the conduction band of the CuO to the Al electrode, respectively. Formation of the CuO/ZnO active layer with homogeneous distributed CuO nanoparticles would improve the efficiencies of the solar cells.

4.4 Current Transport Mechanisms of n-ZnO/p-CuO Heterojunction

In this study n – ZnO/p –CuO heterojunction have been fabricated by sol – gel dip – coating technique which is simple and inexpensive. The structure of the p-CuO/n –ZnO was analyzed by x-ray diffraction spectroscopy and UV-VIS spectroscopy. The electrical junction properties were characterized by temperature dependent current-voltage (I-V) characteristics and at high frequency capacitance – voltage (C-V) characteristic at room temperature. The structure showed non – ideal behavior of I-V characteristics with an ideality factor of 3.5 at room temperature. Temperature dependent forward current-voltage measurements suggest that trap-assisted multi-step tunneling is the dominant current mechanism in this structure.

4.4.1 Experiments

In order to prepare ZnO solution, firstly, zinc acetate 2-hydrate [Zn $(CH_3COO)_2$ $2H_2O$] was dissolved in ethanol (CH_3COCH_3 , 99.9%, Merck) and then lactic acid was added as hydrolysis catalyst in drops. Afterwards solution was thoroughly mixed by a magnetic stirs for 2 hours, and homogeneous transparent solution was obtained which had a concentration of 0.4M. Each coating on the ATO (Antimony Tin Oxide) substrate was first dried at 250^0 C for 5min. This process of coating was repeated for 10 times and then the final film was annealed at 250^0 C for 15 min.

CuO layer was deposited on ZnO. The CuO sol was prepared by adding copper 11 acetate ($(CH_3\ COO)_2$ Cu, H_2O) to ethanol and mixing the both components. While sol was mixing, the triethylamine was added in the sol. After the sol prepared, the CuO film was deposited on the ZnO film dried at 250^0 C for 5 min. This process of coating was repeated for 10 times and then the p – n junction was annealed at 250^0 C for 30 min.

After 10 coating for the ZnO film, thickness of the film was calculated $\sim 70nm$ and after 10 coating for the CuO film, it was calculated$\sim 212nm$.

After ZnO/CuO heterojunction was prepared, the contact was composed between the coated film and Cu wire. To insure good contact between the film and Cu wire. Ag paste was used. The crystal structure of the n- ZnO/p- CuO heterojunction was determined by XRD using Rikagu D-max 2200 X-Ray diffract meter system with CuKα radiation ($\lambda = 1.5405$)A^0 and by the UV – VIS spectroscopy (350 – 1100nm) using Perkin Elmer UV – VIS Spectrometer Lambda 2S. The current – voltage characteristics of the heterojunctions were measured with a system which consists of a DC voltage –current source Keithley 2420, a specially designed sample holder computer. Thin films samples were mounted in the sample holder. To control the temperature of the samples. Lake Shore 330 auto tuning temperature controller is used.

4.4.2 Results and discussion

The lattice constants of ZnO calculated from the present data are a=3.300 A^0 and c=5.131 A^0 which are agreement with a=3.253 A^0 and c=5.209 A^0 of ZnO known from the literature (JCPDS Card No. 80-00075) and the lattice constants of CuO calculated from the present data are a= 4.774 A^0, b= 3.434 A^0 and c=5.131 A^0 which are in agreement with the values a= 4.68 A^0, b=3.42 A^0 and c=5.129 A^0 of CuO obtained by kimura et al.

The band gab of ZnO and CuO were determined from measured transmittance spectra. We shows plot of the square of the absorption coefficient (α^2) of ZnO and CuO films fabricated onto glass substrate as a function of the energy of incident radiation. For this, the fundamental absorption coefficient α was evaluated using $\alpha = lnT^{-1}$/d where d is the film thickness and T is the transmittance. The optical band gap, E_g of the film was calculated using the Tauc

relation, which is given as $\alpha = \alpha_0 (h\nu - E_g)^n$ where hν is the photon energy. α_0 is a constant and n=0.5, 1.5, 2 or 3for allowed direct, forbidden direct, allowed indirect and forbidden indirect electronic transitions, respectively. In the present case the band -gap energy gap (E_g) has been estimated by assuming an allowed direct transition (n=1/2). The factor (α^2) varies linearly with hν in the high-energy region. In the low – energy region, the absorption spectrum deviates from the straight line. The band gap was obtained by extrapolating the linear portion of the plot of $(\alpha)^2$ against hν to $(\alpha)^2$ =0. The intercept on energy axis gives the value of the band gap energy (E_g) for the film. The band gap energy (E_g) values of ZnO and CuO are 3.3 and 1.8 eV respectively, which are in agreement with what have been reported previously.

XRD and UV- VIS measurements showed that ZnO films consisted of hexagonal wurtzite crystal grains with energy band gap of 3.3eV. At ambient conditions. The thermodynamically stable phase is hexagonal wurtzite, the cubic zinc blended ZnO structure can be stabilized only by layer growth on cubic substrates, and the cubic rock salt structure may be obtained at relatively high pressures. In our heterojunctions, the ZnO films were deposited onto the ATO substrates. The ATO films are a tetragonal system because tin oxide is a tetragonal system and the lattice parameters are not affected much the incorporation of the dopants in the films, is hexagonal wurtzite system. The CuO layer is monoclinic system. Since all layers at our heterojunction are different crystal systems, the lattice mismatch occur. To confirm the presence of the interface state. We calculate the lattice mismatch given by the relation:

$$\frac{\Delta a}{a} = \frac{a_2 - a_1}{a_2} \tag{4.3}$$

Where a_1 and a_2 are the lattice constant of the ZnO and CuO respectively. The lattice mismatch between CuO and ZnO calculated to be 32%, which is

higher than the Cu_2O/ZnO heterojunction with mismatch of 7.1%, and Cu_2O/ZnO/ITO p-i-n heterojunction with the mismatch 27.1%. So the lattice mismatch leads to an interface defect states. In order to determine the dominant current transport mechanism through n-ZnO/p-CuO heterojunctions, we measured the I-V characteristics at various temperatures. The forward and reverse bias I-V graphics of ZnO/CuO heterojunction samples at different temperature in the range of 300-360 K. The sample was kept in the dark condition during the measurement. It is obvious that the heterojunction are rectifying in the nature with a turn on voltage of ∼0.5Vand under reverse voltage. The breakdown voltage for the sample is ∼0.6 V which is same as that of ZnO/Cu_2O heterojunction prepared by RF-magnetron sputtering and Cu_2O/ZnO/ITO p-i-n heterojunction prepared by electrochemical deposition method. The current at real diode were given at equation (3-5):

$$I = I_0\, exp\left(\frac{qV}{nKT}\right)\left[1 - exp\left(-\frac{qV}{KT}\right)\right] \tag{4.4}$$

Where q is electronic charge, I_0 is the reverse saturation current, V is the applied voltage, n is ideality, k is Boltzmann constant and T is temperature. For V$>$ $3KT/q$ .Eq. (2-5) can also be shown as

$$I = I_0\, exp\left(\frac{qV}{nKT}\right) \tag{4.5}$$

The ideality factor (n) is obtained from the slope of the plot In I versus V. The forward bias ln (I)-V characteristics of the samples at different temperature in the range of 300-360 K. The forward current can be classified into two regions. In the region 11, the forward currents behave linearly due to the serial resistance effect on the system. In region 1, the forward current can be expressed:

$$I = I_0 exp(AV) \tag{4..6}$$

There are three models for explaining the current through heterojunctions: A is independent of the measuring temperature T for a tunneling model, (2) A is temperature, n=1, A=q/KT for the diffusion model, (3) A is temperature dependent, n=2, A=q/2KT for the recombination model. The ideality factor (n), the reverse saturation current I_0 which is a function of temperature, depending on the nature of dominant carrier transport mechanisms in the heterojunction and the slope of ln (I)-V graphics A(is independent of the voltage) of the samples are calculated from the graphics. In table 1, the slope A of the ln (I)-V graphicstemperature insensitive. Therefore, the data are consistent with Eq. (4.7). The ideality factor n is larger than 2.

Table (4.1).The I_0, A and n values for the sample of the n-ZnO/p-CuO heterojunction

T (K)	**I_0 (A)**	**A (V^{-1})**	**N**
300	1.36×10^{-9}	11.0	3.5
310	2.80×10^{-9}	10.1	3.7
320	2.80×10^{-9}	10.6	3.4
330	1.75×10^{-9}	9.7	3.6
340	1.26×10^{-9}	10.1	3.4
350	1.37×10^{-9}	10.0	3.3
360	1.84×10^{-9}	10.1	3.2

The temperature dependence of saturation current I_0 is expressed as:

$$I_0 = I_{00} exp\left(-\frac{\Delta E_a}{KT}\right) \quad (4.7)$$

Where ΔE_a is the thermal activation energy of carrier conduction. Form the slope of ln (I_0) versus T^{-1} graphics, the activation energy was calculated to be 0.412eV. The data fits almost on straight lines, which agrees with multi-step tunneling model. The capacitance per unit area given by Anderson

$$C = \left\{\frac{q\varepsilon_n\varepsilon_p N_a N_d}{2\left(\varepsilon_n N_d + \varepsilon_p \varepsilon_d\right)}\right\}(V_{bi} - V)^{-\frac{1}{2}} \quad (4.8)$$

Where ε_n , ε_p are the dielectric constant and N_d, N_a are ionized impurity density of ZnO and CuO respectively, V_{bi} is the built in potential and V is the applied voltage. The capacitance-voltage characteristics of n-ZnO/p-CuO heterojunction at MHz frequency in dark and at room temperature.

4.4.3 Conclusion

n-ZnO/p-CuO heterojunction has been successfully fabricated onto ATO substrates using sol-gel dip coating method. The thickness of ZnO film prepared by 10-times coating is ~70nm while that of CuO film coated 10-times is ~212 nm. At room temperature, the diode turn –on voltage is of ~0.5V. The temperature dependent I-V characteristics of the n-ZnO/p-CuO heterojuncion showed that the forward current transport can be explained with a multi-step tunneling model between 300-360K. While the activation energy of the saturation current is about 0.412, the built-in potential is about 1.5eV [74].

4.5 Characterization of Cu_2O thin films prepared by evaporation of CuO powder

Among the potential photovoltaic devices based on semiconductor oxides as active layer is cuprous oxide (Cu_2O). This oxide semiconductor shows many attractive characterizes useful for solar cells production such as low cost, nontoxicity, high mobility and diffusion length of minority carriers, high absorption coefficient and direct energy gap. In this work we report out results of optical and structural investigations of Cu_2O thin films fabricated by thermal vacuum evaporation of CuO powder. The effects of the deposition velocity on structural and optical properties of Cu_2O films were investigated. The X-ray investigations have shown that at low deposition velocity the films consist only of Cu_2O phase without any interstitial phase and have a nano-grain structure. The grains have an average dimensions about (25-30) nm and all these grains showed (200) preferential crystallographic orientation. Optical investigations have shown that the absorption edge of prepared films is due to a direct allowed transition. The value of determined optical band gap is 2.05 eV which corresponds to band gap of bulk Cu_2O.

4.5.1 Experiments

Thin films of Cu_2O were fabricated by continuous thermal evaporation of CuO small particles. Schematic view of vacuum evaporation setup presented in figure (3.1). CuO particles have different size from 100 to 500 micrometers. These particles were prepped by crush of pallet which was obtained by pressing commercially available CuO powder (99.9% purity) and sintering at 700°C in air 1 h. The vacuum chamber before evaporation was pumped to a base pressure of 1.5×10^{-5} mm Hg. The thermal evaporation was carried out by dosed supply of CuO particles to the molybdenum boat heated to the temperature 1300°C. Process of CuO particles evaporation occurred as follows. After contact to boat

the particles of CuO in process of their heating at first convert to Cu_2O by the reaction:

$$4CuO \rightarrow 2Cu_2O + O_2 \quad (4.9)$$

And then convert to Cu by the reaction:

$$2Cu_2O \rightarrow 4Cu + O_2 \quad (4.10)$$

Since the temperature of boat was above the temperature of Cu evaporation (1260°C) after thermal decomposition of Cu_2O to Cu and O_2 a full evaporation of Cu was occurred. This method of evaporation provides in average the same flows of copper and oxygen atoms due to different temperature of evaporating particles.

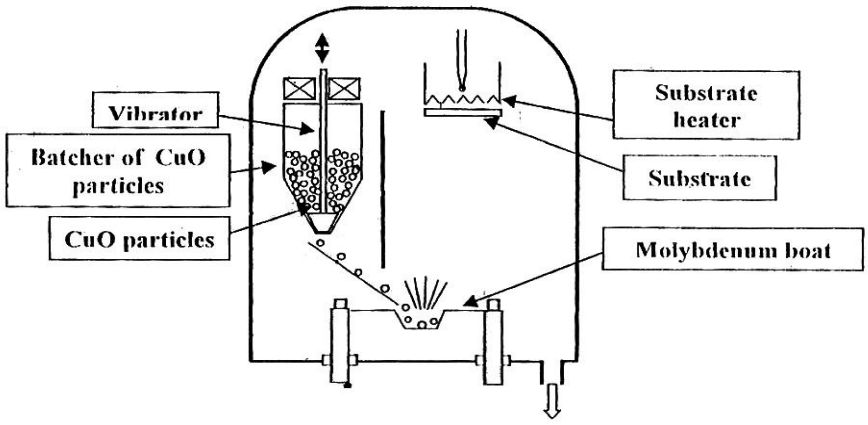

Figure (4.1): schematic representation of the experimental setup

The films were deposited on sapphire substrate. The temperature of substrates was 700°C. During the evaporation process the base pressure in vacuum chamber was changed from base pressure 1.5×10^{-5} mm Hg to the partial pressure of oxygen 1.10^{-4} mm Hg. After the film deposition the substrate was cooled to the room temperature during 1 hour with the chamber pressure 6.10^{-6}

mm Hg. The film thickness and duration of deposition were typically 1-3 micrometer and 3 hours.

The structural properties of samples were studied by X-ray diffract meter URD-6 in the 0-20 mode using Cu-Kα radiation as well as by optical Olympus microscope with magnitude 500. Transmittance and reflectance, over the wavelength from 300 to 1000 nm was measured using double beam Spectra M-50 Spectrophotometer.

4.5.2 Results and discussion

4.5.2.1 Phase formation

We have investigated the characteristics of films depend on the deposition velocity at the temperature of substrate 700°C. Figure (3-2) shows the photo of surface morphology of two films series A and B which differ from each other by the velocity of deposition. For low deposition velocity less than 5 nm/min the films of series A consist of smaller size grains than the films of series B (figures (3-2) a and b).

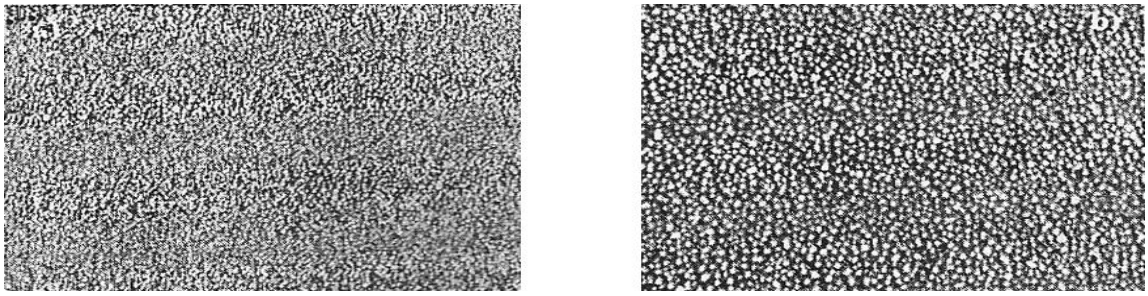

Figure (4.2): the photo of surface morphology of (a) films series A, and (b) films series B (500)

4.5.2.2 Structural analysis (XRD)

Angler XRD patterns of films series A and B are shown figure (3-3) For films series A, there is one strong XRD peak at 20=42.4° corresponding to the

(200) crystal plane of Cu_2O (figure (3-3a). This XRD pattern indicates that films series A is single phase Cu_2O film with crystalline structure. These films consist of nano-size grains and all these grains have identical orientation. Full width of half maximum (FWHM) of the XRD peak was used to estimate the grain size of the films series A. The values of the grain size calculated using Scherer's formula:

$$D = \frac{0.9\lambda}{d.\cos\theta} \qquad (4..11)$$

Where λ is the x-ray wavelength, θ is the Bragg diffraction angle, and d is full-width at the half maximum (FWHM) of the peak corresponding toθ.

For the peak corresponding to the (200) plane of Cu_2O, the resultant grain size is 25 nm. The XRD pattern for films series B presented in figure 3b contains one Cu_2O – related diffraction (111) peak (20-36.38°) and tow Cu- related diffraction peak (111) (2 θ =42.9°) and (200) (2 θ = 49.8°).

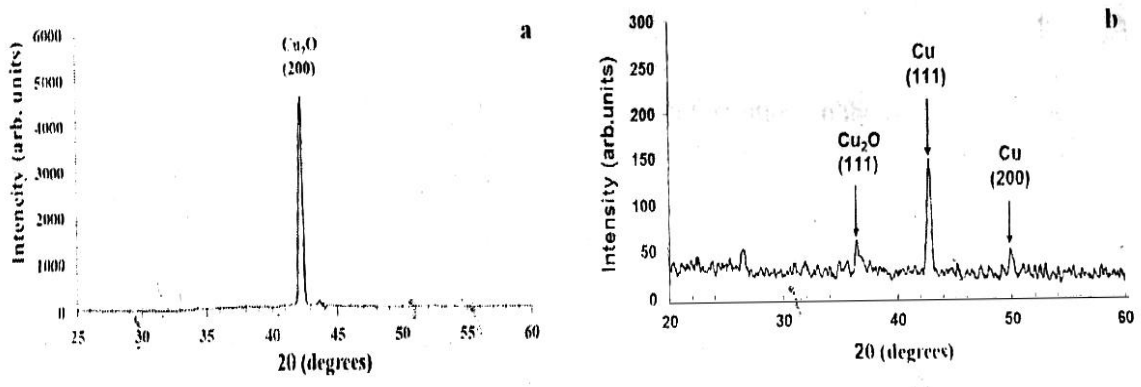

Figure (4.3): XRD patterns of (a) films series A, and (b) films series B

The composition of deposited layer formed due to reaction between cupper and oxygen. Figure (3-4) shows the equilibrium phase diagram of the Cu-O system. The partial pressure and temperature of substrate corresponding to the

films deposition conditions are shown in figure (3-4) (point A). At low velocity of deposition Cu atoms have enough time in order to completely react to oxygen. This time determined by the time of kinetic reaction for formation Cu_2O phase. In this case the composition of deposited film determined by the equilibrium Cu-O phase diagram. It is confirmed by XRD pattern of films series A where observe only Cu_2O- related diffraction peaks. We believe that at high velocity of deposition Cu atoms have not enough time to completely convert in Cu_2O phase (figure (3-3b).

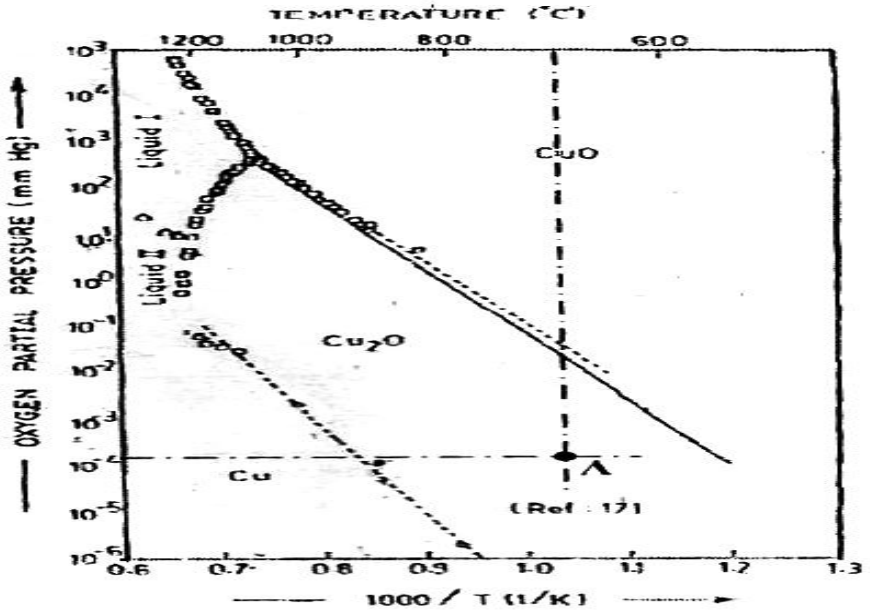

Figure (4.4): The cooper – oxygen equilibrium phase diagram

4.5.2.3 Optical properties

The transmission and absorbance spectra were taken to obtain information on the optical properties of the copper oxide thin film. In the fundamental absorption region, the optical absorption coefficient (α) can be calculated from the transmittance and reflectance data by the equation.

$$\alpha = \frac{1}{d} In \frac{(1-R)}{T} \qquad (4.12)$$

Where d is the thickness of the film.

Above the fundamental absorption edge the dependence of the absorption coefficient on the incident photon energy is given by Taue's model:

$$\alpha . hv = B\left(hv - E_g\right)^n \tag{4.13}$$

Where hv is the photon energy, E_g is the optical band gap and B is a constant and n is an exponent that depends on the type of optical transitions. As shown in figure (3-5) the best linear relationship is obtained by plotting $(\alpha . hv)^2$ against photon energy (hv), indicating that the absorption edge in this film is due to a direct allowed transition. The linear portion of the curve is fitted using linear regression analysis. The value of optical band gap was determined from the value of intercept of the straight line at $\alpha = 0$ the value of determined optical band gap is 2.05 eV which corresponds to the band gap of bulk Cu_2O.

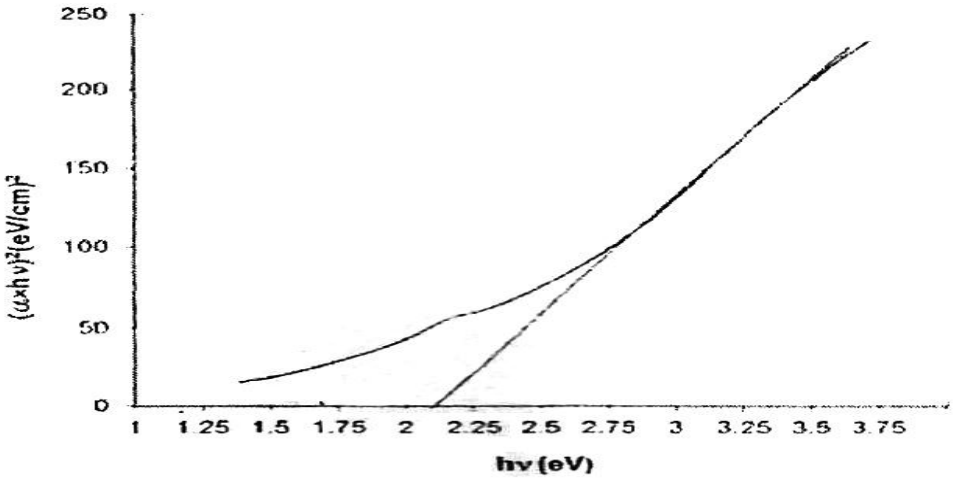

Figure (4.5): Variation of $(\alpha hv)^2$ as a function of photon energy

4.5.3 Conclusion

The films of copper oxide were deposited on sapphire substrate by the continuous thermal evaporation of CuO small particles. The effects of deposition

velocity on the structural and optical properties of Cu_2O films were investigated. It was shown that at deposition velocity less than ~5 nm/min the films deposited on the 700°C substrate consist only of Cu_2O phase. These films have n nano-grain structure and all these nana-grains have (200) preferential crystallographic orientation with average dimensions about (25-30) nm.

It was found that the optical band gap of fabricated Cu_2O films is 2.05 eV which corresponds to the hand gap of bulk Cu_2O[32].

4.6 Characterization of Dye-Sensitized solar cell with ZnO Nanorod multilayer electrode

4.6.1 Introduction

In this study, zinc oxide (ZnO) nonrods were synthesized on indium-tin-oxide (ITO) glass substrates by a hydrothermal process. The growth process was carried out one to five times to obtain ZnO nanorods of different generations (1^{st} to 5^{th} generation). Scanning electron microscopy (SEM), energy dispersive spectrometry (EDS).

And x-ray diffraction (XRD) was used to obtain the surface morphology, chemical composition, and crystallographic structure of the synthesized ZnO nanorods. These ZnO nanorods were submerged in the dye solution and ware used as the working electrode (anode) of dye-sensitized solar cell (DSSC). I-V and optoelectronic characteristics of the DSSCs using ZnO nanorods of different generations as the electrodes were measured to obtain their fill factors and conversion efficiency. Experimental results reveal that the ZnO film of the 4^{th} generation exhibits a uniform distribution of dense nanorods whose shape and microstructure are beneficial to dye adsorption and carrier transport. Therefore, the DSSC fabricated with the ZnO nanorods of the 4^{th} generation has an improved short-circuit current, fill factor, and conversion efficiency.

4.6.2 Experiments Details

In this work, ZnO nanorods prepared by a simple hydrothermal process were used to fabricate the working electrodes for DSSC applications. First, indium-tin-oxide (ITO) glass substrate was cut into 2 cm × 2 cm pieces, and then rinsed with acetone, methanol and deionizer water. After cleaning, the ITO glass substrates were blown with nitrogen to dry. Transparent tapes were adhered along the peripheral of ITO glass substrate. Only the central area of 1 cm x 1 cm was reserved for the growth for ZnO nanorods. In addition to ITO substrates, ZnO nanorods were also synthesized on silicon substrates since they are more suitable for SEM and EDS measurements. Second, deionized water was added to zinc nitrate hexahydrate (Zn $(NO_3)_2$ $6H_2O$) and methenamine ($C_6H_{12}N_4$, HMT) to obtain the reagents used for the growth of ZnO nanorods. These two solutions were mixed at the ratio of 1:1 to obtain a mixture of 0.1 M molar concentration. The mixed solution was vigorously stirred for 20 min at room temperature to ensure full and uniform mixing. The mixture was heated indirectly through water at 85°C. After the temperature of mixture was stabilized, ITO glass substrates were submerged in the mixture with ITO facing upwards. After 1 hr of high temperature process, samples were removed from the beaker and were rinsed with deionized water for 20 min to halt the growth process of ZnO nanorods. Finally, the synthesized ZnO samples were placed into a box for 5 hours so that they can dry by themselves.

This completed the growth process of ZnO, and the ZnO nanorods of the 1^{st} generation were achieved. The 2^{nd}, 3^{rd} 4^{th} and 5^{th} growth processes were then carried out sequentially to obtain the ZnO nanorods of 2^{nd}, 3^{rd}, 4^{th}, and 5^{th} generations. The ZnO nanorods synthesized in the previous growth process were used as the starting point of the next growth process and were covered by the

ZnO nanorods synthesized in the next growth process. The processing parameters (e.g. molar concentration of mixture, growth temperature, and growth time) in all subsequent growth processes of ZnO were the same as those used in the 1st growth process.

After the working electrodes using ZnO nanorods of different generations were fabricated, they were submerged in the dye solution for 8 hours so that the dye can be fully absorbed by ZnO nanorods. Subsequently, the working electrodes were assembled with the counter electrode of Pt film/ITO glass and electrolyte was injected to from DSSC.

The purpose of this work is to study the surface morphology, chemical composition, and microstructure of the ZnO nanorods of different generations. Scanning electron microscopy (SEM), energy dispersive spectrometry (EDS) and (XRD) were used to obtain the surface morphology, chemical composition, and crystallographic structure of ZnO nanorods. Afterwards, I-V characteristics of the $DSSC_s$ using ZnO nanorods of different generations were measured, and open-circuit voltage, short-circuit current, fill factor, and conversion efficiency were determined.

4.6.3. Results and Discussions:

In this study, zinc nitrate hexahydrate (Zn $(NO_3)_2$, $6H_2O$) and hexamethylene tetramine ($C_6H_{12}N_4$, HMT) were mixed at the ratio of 1:1 in water. The molar concentration ratio of Zn $(NO_3)_2$.$6H_2O$ and C6H12N4 was 1 : 1 which was the optimum value determined from our previous experimental results. HMT is non-toxic and its water-soluble polymer ring dissolves in acidic solution into functional groups to form NH3. $Zn(NO_3)_2$ can react with HMT in water to synthesize ZnO nanorods. The chemical reactions involved in the growth of ZnO nanorods are:

$C_6H_{12}N_4+6H_2O \rightarrow 6HCHO+4NH_3$

(4.14)

$NH_3+H_2O \rightarrow NH_4+OH^-$

4.15)

$2OH^-+Zn^{2+} \rightarrow ZuO+H_2O$ (4.16)

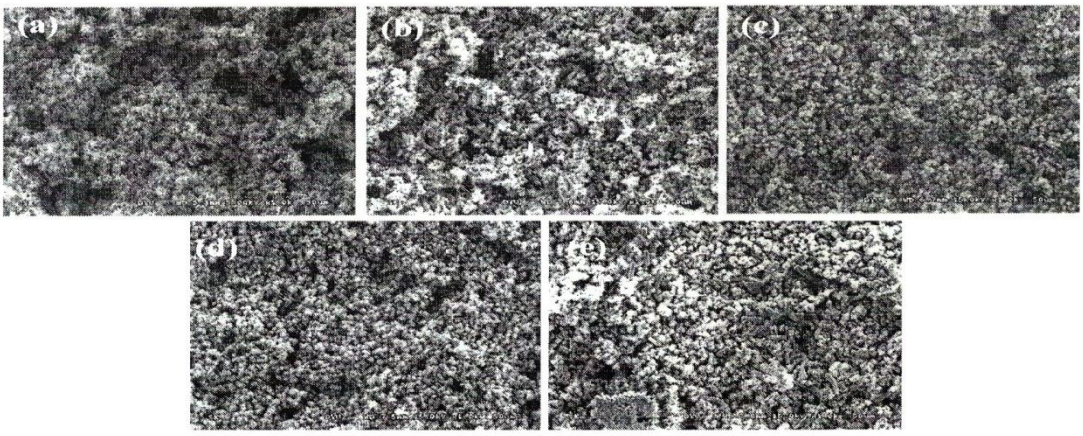

Figure (4.6) The top-view SEM images of ZnO nanorods of the: (a) 1^{st} , (b) 2^{nd} , (c) 3^{rd} (d) 4^{th} , and (e) 5^{th} generations. The magnification factor is $l \times l0^3$.

First, $C_6H_{12}N_4$ is disintegrated into formaldehyde (HCHO) and ammonia (NH_3) as shown in equation (3-6). Ammonia tends to disintegrate water to produce OH^- anions (equation 3-7). Finally, OH anions react with Zn^{+2} cations to form ZnO (equation 3-8). In the growth process of ZnO nanorods, the concentration of OH^- anions is the dominant factor. Therefore, $C_6H_{12}N_4$ that supplies OH^- anions play a key role in the growth of ZnO nanorods.

The hydrolysis rate of $C_6H_{12}N_4$ is low and thus can provide OH^- anions at a steady rate rendering a solution with a constant concentration of 0H anions. At low concentrations of $C_6H_{12}N_4$ + $Zn(NO_3)_26H_2O$, the reaction rate of OH^- anions is low: on the other hand, the reaction rate and the growth rate of ZnO nanorods

is high at high concentrations of $C_6H_{12}N_4$ + $Zn(NO_3)_26H_2O$. In this study, the molar concentration of mixture used in the growth process was 0.1M. Since our previous study has demonstrated that DSSC using ZnO nanorods electrode prepared with 0.1 M mixture, same concentration of mixture was used in this work to study the effect of ZnO nultilayer electrode on the operating characteristics of DSSC.

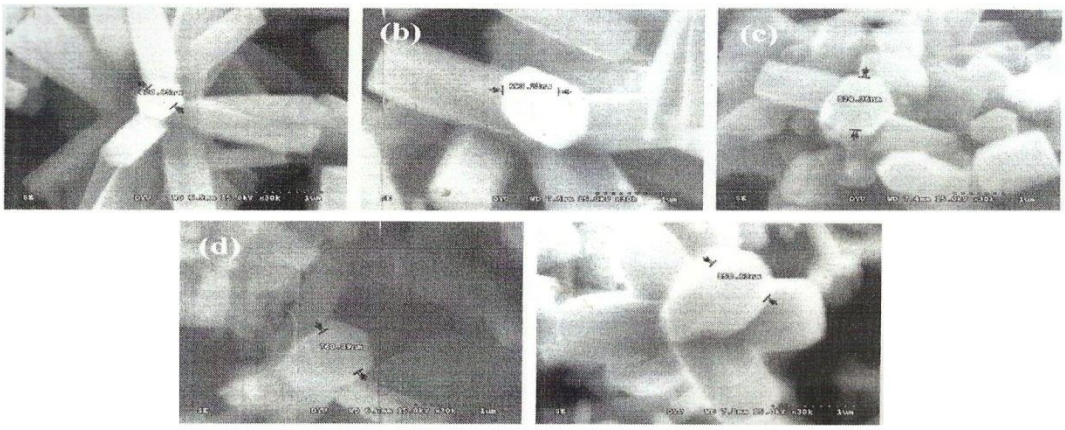

Figure (4.7) The enlarged SEM images of ZnO nanorods of the: (a) 1st , (b) 2nd , (e) 3rd (d) 4th , and (e) 5th generations. The magnification factor is 3 × 10^4.

Table (4.2) Chemical composition for the ZnO nanorods of different generations.

Chemical composition	Atomic percentage (%)				
	1st	2nd	3rd	4th	5th
O	77.82	60.18	53.49	52.85	50.60
Si	2.80	0	0	0	0
Zn	19.37	39.82	46.51	47.15	49.40
ZnO	1:4.02	1:1.51	1:1.15	1:1.12	1:1.02

Figure (4.7) shows the top-view SEM images of ZnO nanorods of different generations, while the enlarged images arc shown in the Figure (4.2). The

magnification factor is 1×10^3 for Figure (3.7), and is 3×10^3 for Figure (4.8). The growth parameters are listed as follows: the growth temperature was 85°C, growth time was 1 hr, the molar concentrations of

$Zn(NO_3)_2.6H_2O$ and $C_6H_{12}N_4$ were 0.1M (the molar ratio was 1:1), and the growth process was repeated 1 to 5 times.

From Figure (4.7)(a), (b), (c), (d), and (e), it is clearly seen that no obvious change in the surface morphology of ZnO nanorods of different generations can be observed. Figure (3-7)(a) shows the ZnO nanorods of the 1st generation which is obtained with a mixture solution of 0. 1M. the average diameter of ZnO nanorods is ~420 nm. The average diameter of nanorods increases logarithmically from ~ 693 nm for the ZnO of the 1st generation to 858 nm for the ZnO of the 5th generation. As shown in Figures (4.7) (d) and (e), the shape of nanorods tends to become short and wide. Since fresh mixture solution was added before every growth process in order to maintain a constant ion concentration of 0.1M in the solution, the ZnO nanorods that have been adhered to the substrate already will have the opportunity to replenish newly added anions. Since the growth rate on the six side walls is higher than that on the tip surface, it is reasonable for the shape of ZnO nanorods to become short and wide after multiple growth processes.

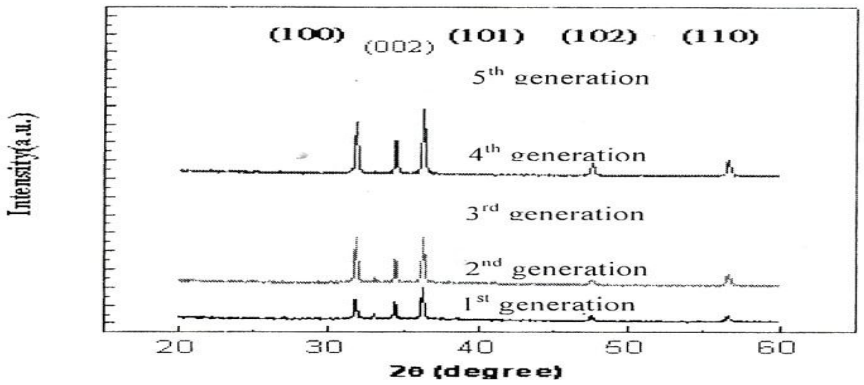

Figure (4.8). XRD spectra for the ZnO nanorods of different generations.

Table (4.3) Intensities of characteristic peaks in XRD spectra for the ZnO nanorods of different generations.

Generation of ZnO	I_a	I_c	I_b	I_a/I_c	I_b/I_c
1st	602	511	893	1.18	1.74
2nd	829	653	1169	1.27	1.79
3rd	959	710	1292	1.35	1.82
4th	1502	1058	2000	1.42	1.89
5th	1669	1135	2290	1.47	2.02

In this study, EDS used to measure the chemical composition of ZnO nanorods of different generations and is listed in Table (4.3). As observed in the EDS analysis, the atomic content of silicon in the ZnO nanorods of the 1st generation is 2.8%. Since no silicon-containing reagent was used in the growth process. The detected silicon content is caused by silicon atoms on the substrate. Obviously, the ZnO nanorods were not dense enough to completely. Cover the entire substrate. As the ZnO nanorods evolve into the 2nd generation. The atomic percentage of silicon drops to 0% indicating that the distribution of ZnO nanorods is uniform and dense. The silicon substrate is completely covered by ZnO nanorods. This is beneficial to the uniform adsorption of dye molecules. The chemical composition for ZnO nanorods of different generations can be clearly seen in table 1. It seems that the atomic ratio of zinc to oxygen decreases as the ZnO nanorods evolve. The atomic ratio of zinc to oxygen on the surfaces of nano rods is 1:4.02 for the ZnO nanorods of the 1st generation. Whereas this atomic ratio decreased to 1:1.02 for the ZnO nanorods of the 5th generation which is close to the theoretical value of 1 as is expected for ZnO.

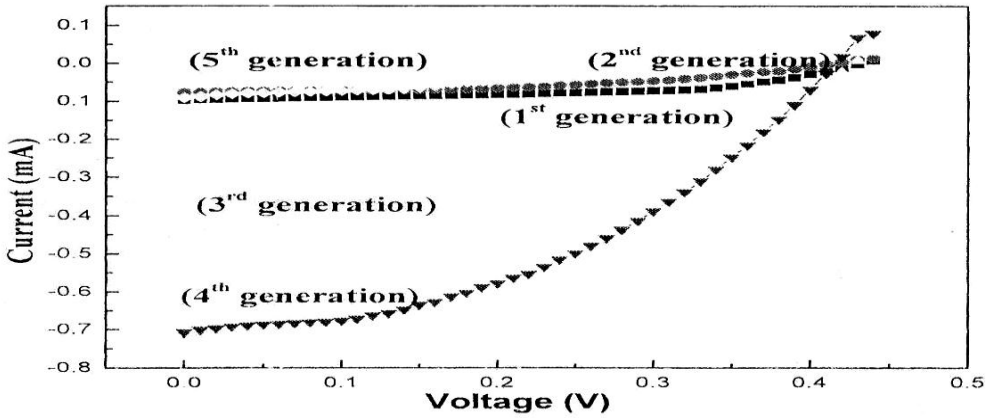

Figure (4.9) I-V characteristics for the DSSC using ZnO nanorods of different generations as the working electrode.

Figure (4.3) shows the XRD spectra for the ZnO nanorods of different generation. In figure (4.4), all spectra exhibit five peaks located at diffraction angles of 2seta=31.77^0. 34.42^0 and 36.25^0 are most pronounced. These three peaks correspond to (100),(002), and (101) directions of crystallization of wurtzite ZnO nanorods, i.e the growth along the directions of a, b, and c axis of nanorod hexagonal structure, respectively. These intensities of characteristic peaks in XRD spectra for the ZnO nanorods of the different generation are summarized in Table 2. In the different spectra, the intensity ratio in the direction of axis and c axis (I_a/I_c) and the intensity ratio in the direction of axis and c axis (I_b/I_c) are useful. As ZnO nanorods evolve from the 1^{st} generation to the 5^{th} generation, the values of I_a/I_c and I_b/I_c increase. The value of I_a/I_c increase from 1.18 to 1.47. and I_b/I_c increases from 1.74 to 2.02. The aspect ratio of nanorod also increases with the evolution of ZnO nanorods.

This is because the increases in the growth rate on the (100) and (101) surfaces of ZnO nanorods are higher than that on the (002) surface. Hence, nanorods become short and wide. This assertion is verified by the SEM image in Figure (4.1)

Figure (4.5) shows the I-V characteristics of the $DSSC_s$ fabricated with ZnO nanorods of different generations. The corresponding open-circuit voltage (V_{oc}), short-circuit current (I_{sc}), and fill-factor (FF) are tabulated in Table 3. For the $DSSC_s$ prepared with ZnO nanorods of the 4^{th} generation exhibits much improved short-circuit current and fill factor., and hence a much higher conversion efficiency. However, it is found that the $DSSC_s$ prepared with ZnO nanorods of the 5^{th} generation has a lower short-circuit current, open-circuit voltage, fill factor, and hence a lower conversion efficiency. Possible explanations are given s follows. For the ZnO nanorods of the 1^{st} generations, the distribution of nanorods on the ITO glass substrates is not uniform. Lots of voids and vacancies are found in the ZnO film so that dyes can not uniformly adsorbed in the film. Therefore, the DSSC prepared with the 1^{st} generation ZnO nanorods exhibit poor *I-V* characteristics. The distribution of ZnO nanorods of the 2^{nd} generation is still non-uniform indicating that there are some voids and vacancies in the ZnO film. This can affect the adsorption of dye molecules so that only slight improvement in the *I-V* characteristics of DSSC can be achieved.For the $DSSC_s$ using ZnO nanorods of the 3^{rd} and 4^{th} generation. Substantial improvement in their *I-V* characteristics is evident. Compared with the DSSC prepared with ZnO nanorods of the 1^{st} generation, short-circuit current increases by a factor of 7 for the DSSC using ZnO nanorods of the 4^{th} generation, and a large increase in the conversion efficiency of DSSC is achieved. From the atomic ratio of zinc to oxygen in EDS analysis, the structure of the ZnO nanorods of the 3^{rd} and 4^{th} generations is considerably better than that of the ZnO nanorods of the 1^{st} and 2^{nd} generation. Much fewer bonding vacancies are present in the nanorods. Therefore, electron is easier to travel in these films and the conversion efficiency of DSSC is increased.

The reason for the degeneration in the I-V characteristics as found in the DSSC prepared with ZnO nanorods of the 5^{th} generation is presumably caused

by the larger thickness of ZnO film. The distance which electrons have to travel through the ZnO film is increased, thus electron-hole recombination is more likely to take place and photocurrent is decreased according. Furthermore, the average diameters of ZnO nanorods become larger for the ZnO nanorods of the 5^{th} generation so that the aspect ratio of nanorods increases and nanorods become short and wide. The voids and vacancies lying between nanorods become larger and intimated contact between nanorods is unlikely now. This results in an increase in the internal resistance of working electrode. FF factor and conversion efficiency are decreased drastically and operating characteristics of DSSC are severely degraded.

The diffraction characteristic peaks of these five peaks appears in :

Figure (4. 3) shows the XRD spectra for the ZnO nanorods of different generation. In figure (4.3), all spectra exhibit five peaks located at diffraction angles of 2seta=31.77^0. 34.42^0 and 36.25^0 are most pronounced. These three peaks correspond to (100),(002), and (101) directions of crystallization of wurtzite ZnO nanorods, i.e the growth along the directions of a, b, and c axis of nanorods hexagonal structure, respectively. These intensities of characteristic peaks in XRD spectra for the ZnO nanorods of the different generation are summarized in Table 2. In the different spectra, the intensity ratio in the direction of axis and c axis (I_a/I_c) and the intensity ratio in the direction of axis and c axis (I_b/I_c) are useful. As ZnO nanorods evolve from the 1^{st} generation to the 5^{th} generation, the values of I_a/I_c and I_b/I_c increase. The value of I_a/I_c increase from 1.18 to 1.47. and I_b/I_c increases from 1.74 to 2.02. The aspect ratio of nanorods also increases with the evolution of ZnO nanorods.

This is because the increases in the growth rate on the (100) and (101) surfaces of ZnO nanorods are higher than that on the (002) surface. Hence,

nanorods become short and wide. This assertion is verified by the SEM image in Figure 1(e.

Figure (4.4) shows the I-V characteristics of the $DSSC_s$ fabricated with ZnO nanorods of different generations. The corresponding open-circuit voltage (V_{oc}), short-circuit current (I_{sc}), and fill-factor (FF) are tabulated in Table 3. For the $DSSC_s$ prepared with ZnO nanorods of the 4^{th} generation exhibits much improved short-circuit current and fill factor., and hence a much higher conversion efficiency. However, it is found that the $DSSC_s$ prepared with ZnO nanorods of the 5^{th} generation has a lower short-circuit current, open-circuit voltage, fill factor, and hence a lower conversion efficiency. Possible explanations are given s follows. For the ZnO nanorods of the 1^{st} generations, the distribution of nanorods on the ITO glass substrates is not uniform. Lots of voids and vacancies are found in the ZnO film so that dyes can not uniformly adsorbed in the film. Therefore, the DSSC prepared with the 1^{st} generation ZnO nanorods exhibit poor *I-V* characteristics. The distribution of ZnO nanorods of the 2^{nd} generation is still non-uniform indicating that there are some voids and vacancies in the ZnO film. This can affect the adsorption of dye molecules so that only slight improvement in the *I-V* characteristics of DSSC can be achieved. For the $DSSC_s$ using ZnO nanorods of the 3^{rd} and 4^{th} generation. Substantial improvement in their *I-V* characteristics is evident. Compared with the DSSC prepared with ZnO nanorods of the 1^{st} generation, short-circuit current increases by a factor of 7 for the DSSC using ZnO nanorods of the 4^{th} generation, and a large increase in the conversion efficiency of DSSC is achieved. From the atomic ratio of zinc to oxygen in EDS analysis, the structure of the ZnO nanorods of the 3^{rd} and 4^{th} generations is considerably better than that of the ZnO nanorods of the 1^{st} and 2^{nd} generation. Much fewer bonding vacancies are present in the nanorods. Therefore, electron is easier to travel in these films and the conversion efficiency of DSSC is increased.

The reason for the degeneration in the I-V characteristics as found in the DSSC prepared with ZnO nanorods of the 5^{th} generation is presumably caused by the larger thickness of ZnO film. The distance which electrons have to travel through the ZnO film is increased, thus electron-hole recombination is more likely to take place and photocurrent is decreased according. Furthermore, the average diameters of ZnO nanorods become larger for the ZnO nanorods of the 5^{th} generation so that the aspect ratio of nanorods increases and nanorods become short and wide. The voids and vacancies lying between nanorods become larger and intimated contact between nanorods is unlikely now. This results in an increase in the internal resistance of working electrode. FF factor and conversion efficiency are decreased drastically and operating characteristics of DSSC are severely degraded.

Table (4.4) Open-circuit voltage (Voc), short-circuit current (Isc), and fill factor (FF) for the DSSCs using ZnO nanorods of different generations as the working electrode.

Generation of ZnO	V_{oc}(V)	Isc(A)	FF(%)
1^{st}	0.44	9.812×10^{-5}	53.101
2^{nd}	0.43	1.694×10^{-4}	44.287
3^{rd}	0.43	4.477×10^{-4}	44.050
4^{th}	0.42	7.074×10^{-4}	41.979
5^{th}	0.37	2.348×10^{-4}	40.745

4.6.4 Conclusions

In this study, ZnO nanorods of different generations were used as the working electrodes for DSSCs. Experimental results reveal that the average diameter of ZnO nanorods increases with the evolution of ZnO nanorods.

As the ZnO nanorods evolve, the shape of ZnO nanorods varies from long, slender hexagonal column to short, wide rods after multiple growth processes. As the ZnO nanorods evolve into the 4uh1 generation, substantial improvement in the open-circuit voltage, short-circuit current, and conversion efficiency of DSSC are achieved. As the ZnO nanorods evolve into the 515 generation, the average diameter of nanorods increases to lower the specific surface area.

Less dye molecules are adsorbed which makes the photocurrent decrease. Another possible reason is the increase of internal resistance in the ZnO nanorods working electrode which can also lower fill factor and conversion efficiency[74].

Chapter Five

Material and Method

5. 1 Introduction

ZnO is an attractive compound semiconductor with a wide band gap ($E_g = 3.3\,eV$) and a large excitons binding energy (60 meV) at room temperature. It is one of a few materials that are suitable for fabrication as optoelectronic devices in short wave length region [75] attributes to these unique properties. Furthermore,ZnO can be used for various applications such as field effect transistor [76], solar cells [77] and surface acoustic wave devices [78].

Various techniques have been used to grow ZnO thin film and nanostructures. For examples, Radio Frequency (RF) sputtering [79], Pulsed Laser Deposition (PLD) [80] and Metal Organic Chemical Vapour Deposition (MOCVD) [81] have been used to deposit ZnO film. On the other hand, Chemical Vapour Deposition (CVD) [82] and direct oxidation from Zn metal block [83] have been used to grow ZnO NWs. In order to realize the importance of using ZnO nanostructures in the above mentioned applications, it is necessary to produce ZnO nanostructures with good crystal quality at relatively low synthesis temperature.

While CuO constitute the most diverse class of materials having properties covering almost all aspects of material science and physics. Among these materials, copper oxide CuO is very promising. It is a p-type semiconductor material with a band gap of about1.8 eV. The growing interest granted to CuO is due to many potential applications that it offers in the conversion of solar energy, optoelectronics and photo catalytic degradation of organic pollutants. It is also used in consumer products such as pillowcases and socks because of its cosmetic and antimicrobial properties.

In this work, the structural and optical properties of ZnO and CuO films were studied. The ZnO/CuO films were deposited using chemical deposition techniques.

Optical properties and processes in ZnO/CuO as well as its refractive index, absorbance, Transmittance reflectance, Absorption coefficient (α), Extinction coefficient (K) and the optical energy gap (E_g) were extensively studied.

As a consequence, ZnO is recognized as a promising photonic material in the blue- UV region.

Optical transitions in ZnO have been studied by a variety of experimental techniques such as optical absorption, transmission, reflection, photo reflection, spectroscopic ellipsometry, photoluminescence, cathodoluminescence, calorimetric spectroscopy, etc. It is well known that at room temperature the PL spectrum from ZnO typically consists of a UV emission band and a broad emission band, The UV emission band is dominated by the free exciting (FE) emission.

The broad emission band literally between 420 and 700nm observed nearly in all samples regardless of growth conditions is called deep level emission band (DLE).

5.2 Materials and Methods

5.2.1 Growth of CuO thin films

Copper oxide (CuO) thin films were prepared by dissolving 0.2 molar copper acetate and monoethanolamine in a 1:1 Molar ratio in 20 ml of 2-methoxyethanol solvent. Acetic acid was added drop wise to achieve a homogeneous solution. The above stock solution was vigorously stirred at 80^{O} C for 120 min. The Cu aqueous solution was filtered through a 0.2 μm poly-tetrafluoroethylene membrane and was aged for 24 h. The colour of the solvent became dark green. The precursor solution was uniformly deposited on cleaned ITO glass substrates by spin coating technique at a spin speed of 2000 rpm for

60 s. The coating process was repeated to attain the desired thickness. The films were annealed at 90 ^{O} C for 5 min after each layer deposition.

5.2.2 Growth of ZnO thin films

the precursor solution for fabricating zinc oxide thin films were prepared by dissolving 0.3 Molar zinc acetate and monoethanolamine (MEA) in a 1:1 Molar ratio in 20 ml of 2-methoxyethanol solvent. MEA was added as a stabilizer to ameliorate the solubility of the precursors. Acetic acid is then added to achieve a homogeneous solution. Above mixture was stirred at 70 ^{O}C for one hour. After stirring, the Zn aqueous solution was aged for 24 h. The colour of the solvent then became yellowish orange. The precursor solution was uniformly deposited on ITO cleaned glass substrates that coating in it CuO by spin coating technique at a spin speed of 2000 rpm for 60 s. The coatings were repeated to achieve the desired thickness of 561.56 nm. After each coating the films were baked at 70^{O}C for 5 min.

5.2.3 Samples of CuO and ZnO films annealed at various temperatures

The 8 samples of CuO and ZnO films were finally air annealed at various temperatures ranging from (60, 70, 80, 90, 100, 110, 120 and 130) ^{O}C for three hours. Each layer was characterized by studying structural, electrical and optical properties. Glancing angle X-ray diffraction analysis of the films was performed with (XRD) system. Surface morphology of the film was studied by (SEM). Optical absorbance measurements were performed with UV -Vis spectrophotometer 1240 was performed at room-temperature. Electrical characterization of the resistive thin films and current voltage characteristics of p-n junction were performed at room temperature using Kiethley 4200-SCS semiconductor parameter analyzer equipped with.

5.3 Theoretical Back ground

Consider an electron affected by electric field of strength E and friction force of coefficient γ.Itsequation of motion is given by:

$$m\ddot{x} = eE - \gamma x \quad (5.1)$$

Consider the solution

$$x = x_0 e^{-iwt}$$

From which $\dot{x} = -iwx \quad and\ \ddot{x} = -i^2 w^2 x$

$$\ddot{x}$$

$$= -w^2 x \quad (5.2)$$

Thus

$$\mathrm{m}(-\mathrm{w}^2\mathrm{x}) + -\gamma\mathrm{iwx} = \mathrm{eE}$$

$$-\mathrm{w}[\mathrm{mw} + \mathrm{i}\gamma]\mathrm{x} = \mathrm{eE}$$

$$\mathrm{x} = \frac{\mathrm{eE}}{-\mathrm{w}[\mathrm{mw}+\mathrm{i}\gamma]}$$

$$x = \frac{-eEw[mw - i\gamma]}{-w[mw + i\gamma]w[mw - i\gamma]}$$

$$x = \frac{eE[-mw + i\gamma]}{w[(mw)^2 + \gamma^2]} \quad (5.3)$$

As a result the electric dipole moment is given by

$$P = enx = \frac{en[-mw + i\gamma]eE}{w[(mw)^2 + \gamma^2]} = \varepsilon_0 \chi E \quad (5.4)$$

Thus the electric field susceptibility is a complex quantity in the form

$$\varepsilon_0 \chi = \varepsilon_0(\chi_1 + i\chi_2) = \frac{e^2 n[-mw + i\gamma]eE}{w[(mw)^2 + \gamma^2]}$$

$$\chi_1 = \frac{-mw^2}{w[(mw)^2 + \gamma^2]} \qquad \chi_2 = \frac{e^2 n\gamma}{w[(mw)^2 + \gamma^2]} \quad (5.5)$$

This susceptibility is related to the absorption coefficient α according to the expression of light intensity.

$$I = \lfloor E \rfloor^2 = \left[E_0 e^{i[(k_1 + ik_2)z - wt]}\right]^2 = E_0^2 e^{-2k_z Z} = I_0 e^{-\alpha Z} \quad (5.6)$$

Where $\alpha = 2k_2$ (5..7)

But the complex wave number satisfies

$$k = k_1 + ik_2 = \frac{w}{v} = w\sqrt{\mu\varepsilon}$$

$$k^2 = w^2\mu\varepsilon$$

$$k_1^2 - k_2^2 + 2ik_1k_2 = w^2\mu(\varepsilon_1 + i\varepsilon_2) \quad (5.8)$$

But

$$E = \varepsilon_0 E + P = \varepsilon_0[1 + x_1 + ix_2]E$$

$$= (\varepsilon_1 + i\varepsilon_2)E \quad (5.9)$$

Thus

$$\begin{cases} \varepsilon_1 = \varepsilon_0(1 + x_1) = k_1^2 - k_2^2 \\ \varepsilon_2 = \varepsilon_0 x_0 = 2k_1k_2 \end{cases} \quad (5.10)$$

From equation (5.10) and (5.7)

$$\alpha = 2k_2 = \frac{\varepsilon_0 x_2}{k_1} \quad (5.11)$$

In view of eqn. (5.5)

$$\alpha = \frac{\varepsilon_0 ne^2\gamma}{w\lceil(mw)^2 + \gamma^2\rceil} \quad (5.12)$$

If the mass and frequency are large enough such that

$$mw > \gamma \quad (5.13)$$

γ Can be neglected one get

$$\alpha = \frac{\varepsilon_0 \mathrm{n e}^2 \gamma}{\mathrm{m}^2 \mathrm{w}^3} \quad (5.14)$$

Considering γ behaves like viscosity η which depend on temperature T, it follows that

$$\alpha \backsim \gamma \sim \eta \sim T^{\frac{1}{2}} \quad (5.15)$$

5.4 Results

5.4.1 CHARACTERIZATION STUDIES

5.4.1.1 Optical properties

The figure from (1-6) exhibits the optical properties of CuO/ZnO thin films prepared by means of chemical deposition techniques.

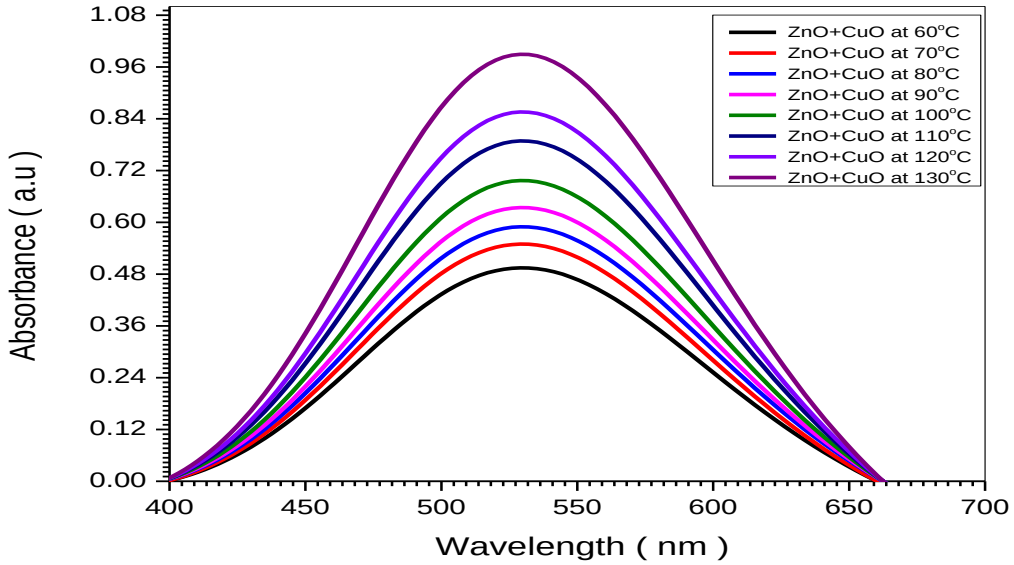

Figure (5.1) Relationship between absorbance and wavelength of ZnO/CuO p-n junction for 8 samples by heated at different temperatures in darkness

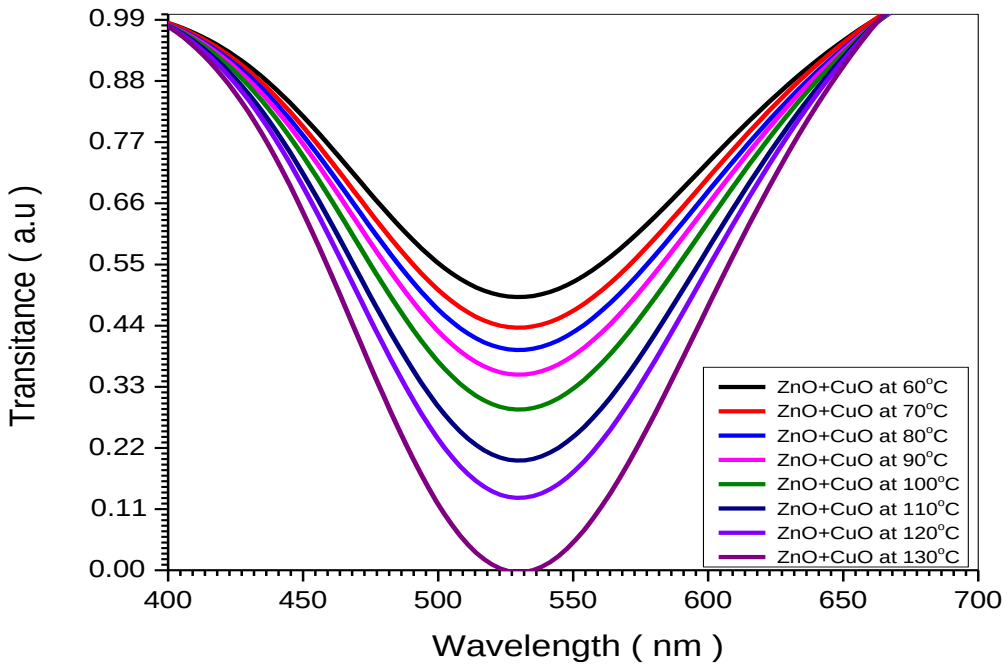

Figure (5.2) Relationship between transmittance and wavelength of ZnO/CuO p-n junction for 8 samples heated at different temperatures in the darkness

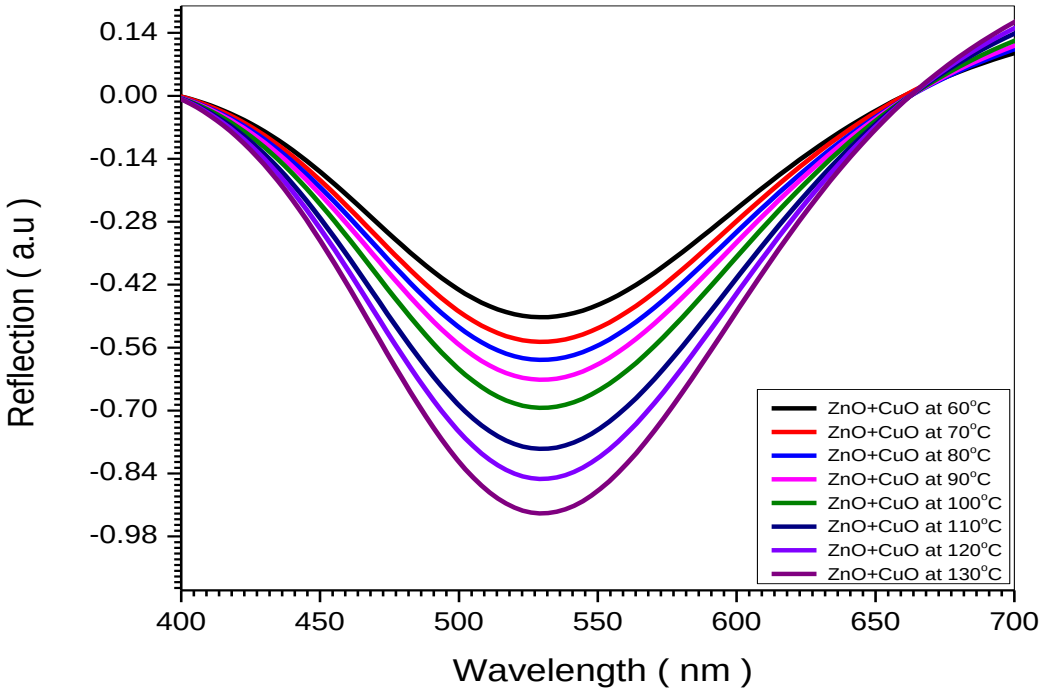

Figure (5.3) relationship between reflectance and wavelength of ZnO/CuO p-n junction for 8 samples heated at different temperatures in the darkness

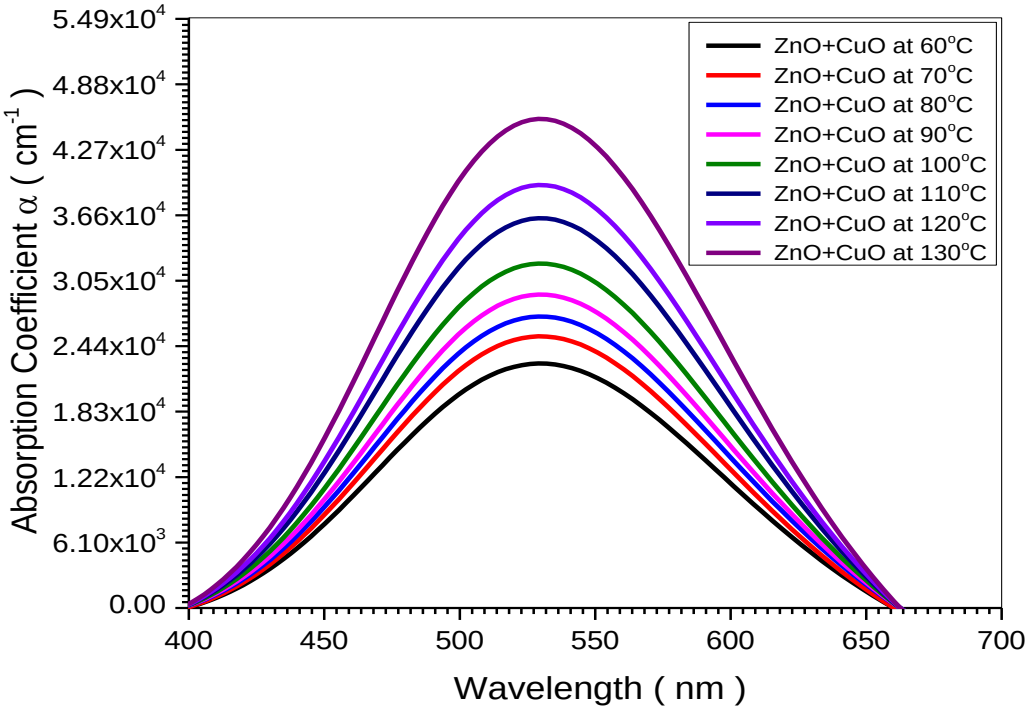

Figure (5.4) relationship between Absorbance coefficient (α) and wavelength of ZnO/CuO p-n junction for 8 samples heated at different temperatures in darkness.

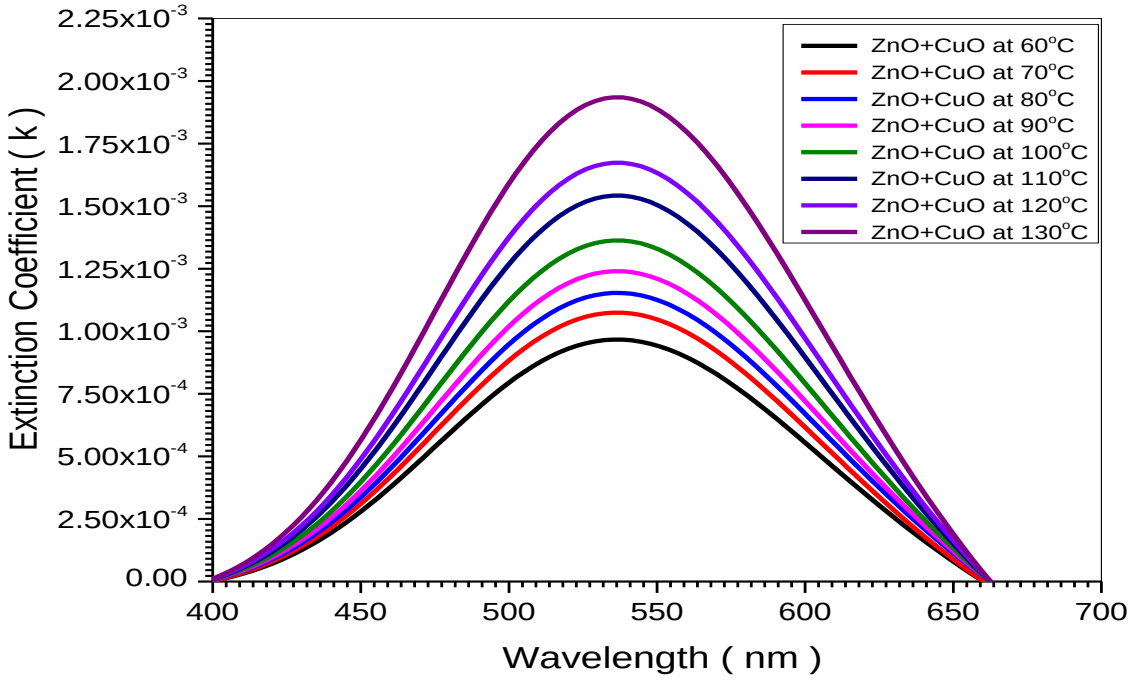

Figure (5.5) relationship between Extinction coefficient (K) and wavelength of ZnO/CuO p-n junction for 8 samples heated at different temperatures in darkness.

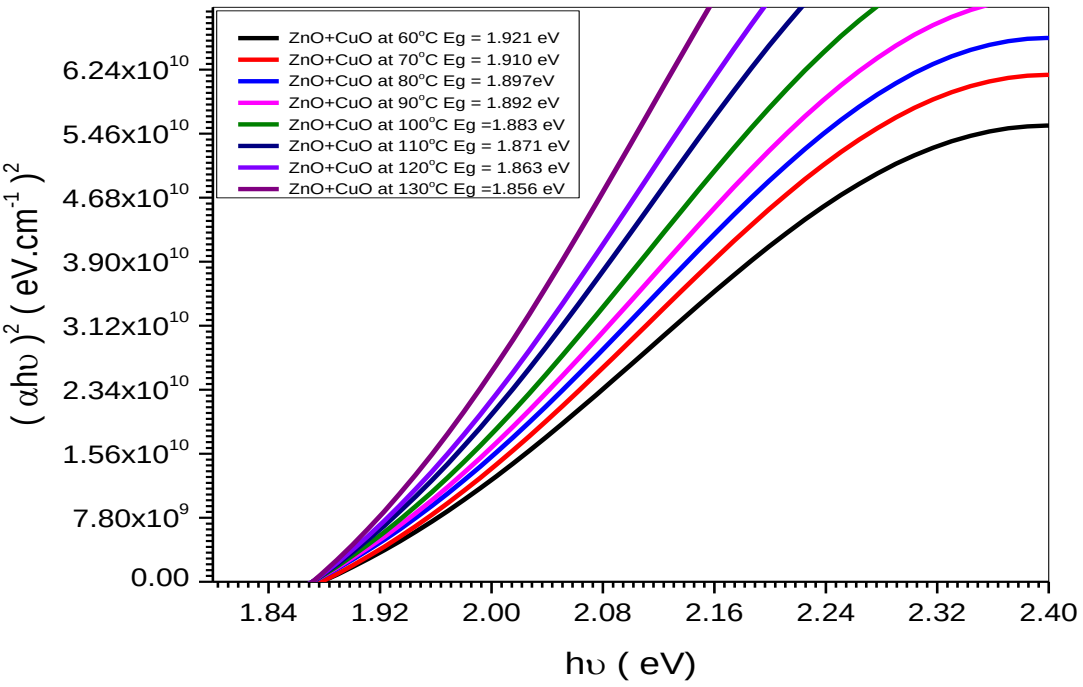

Figure (5.6) the optical energy gap (E_g) of ZnO/CuO p-n junction for 8 samples heated at different temperatures in darkness.

5.4.1.2 I-V Characteristic

Table (5.1) The I-V riding of ZnO/CuO p-n junction for 8 samples by heated for different temperatures in the darkness (without exposed to direct light)

Voltage (V)	I at60^{o}C (mA)	I at 70^{o}C (mA)	Iat80^{o}C (mA)	Iat90^{o}C (mA)	I at 100^{o}C (mA)	I at 110^{o}C (mA)	I at 120^{o}C (mA)	I at 130^{o}C (mA)
-10	-0.01408	-0.01498	-0.01628	-0.01809	-0.02033	-0.02236	-0.02459	-0.02705
-8.11712	-0.01359	-0.01445	-0.01571	-0.01746	-0.01962	-0.02158	-0.02373	-0.02611
-6.21522	-0.01255	-0.01336	-0.01452	-0.01613	-0.01812	-0.01994	-0.02193	-0.02412
-4.31331	-0.01042	-0.01108	-0.01205	-0.01339	-0.01504	-0.01654	-0.0182	-0.02002
-2.41141	-0.00609	-0.00648	-0.00704	-0.00782	-0.00879	-0.00967	-0.01063	-0.0117
-0.50951	0.00236	0.00251	0.00273	0.00303	0.0034	0.00374	0.00412	0.00453
1.39239	0.01766	0.01879	0.02042	0.02269	0.0255	0.02805	0.03085	0.03394
3.29429	0.04202	0.04471	0.04859	0.05399	0.06067	0.06673	0.07341	0.08075
5.1962	0.07379	0.0785	0.08533	0.09481	0.10653	0.11718	0.1289	0.14179
7.0981	0.10598	0.11274	0.12254	0.13616	0.15299	0.16829	0.18512	0.20363

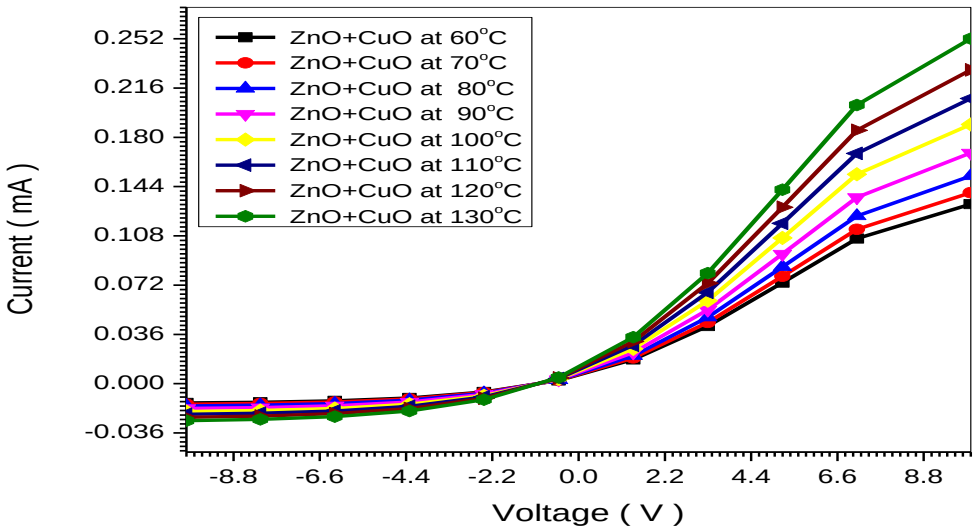

Figure (5.7) The I-V curves of ZnO/CuO p-n junction for 8 samples by annealed different temperatures in the darkness

Table (5.2) The I-V riding of ZnO/CuO p-n junction for 8 samples by annealed different

Voltage (V)	I at60^{o}C (mA)	I at 70^{o}C (mA)	Iat80^{o}C (mA)	Iat90^{o}C (mA)	I at 100^{o}C (mA)	I at 110^{o}C (mA)	I at 120^{o}C (mA)	Iat130^{o}C (mA)
-15.000	-1.00916	-1.13389	-1.21924	-1.32526	-1.45633	-1.60196	-1.60196	-1.93837
-12.027	-0.8421	-0.94618	-1.01739	-1.10586	-1.21523	-1.33676	-1.33676	-1.61748
-9.0240	-0.65522	-0.7362	-0.79162	-0.86045	-0.94555	-1.04011	-1.04011	-1.25853
-6.0210	-0.44826	-0.50366	-0.54157	-0.58866	-0.64688	-0.71157	-0.71157	-0.861
-3.0180	-0.21915	-0.24624	-0.26477	-0.2878	-0.31626	-0.34789	-0.34789	-0.42095
-0.0150	0.03433	0.03857	0.04148	0.04508	0.04954	0.0545	0.0545	0.06594
2.9879	0.31463	0.35352	0.38013	0.41318	0.45405	0.49945	0.49945	0.60434
5.9909	0.6244	0.70157	0.75438	0.81998	0.90107	0.99118	0.99118	1.19933
8.9939	0.96649	1.08594	1.16768	1.26922	1.39474	1.53422	1.53422	1.8564
11.997	1.34399	1.5101	1.62376	1.76496	1.93951	2.13347	2.13347	2.58149

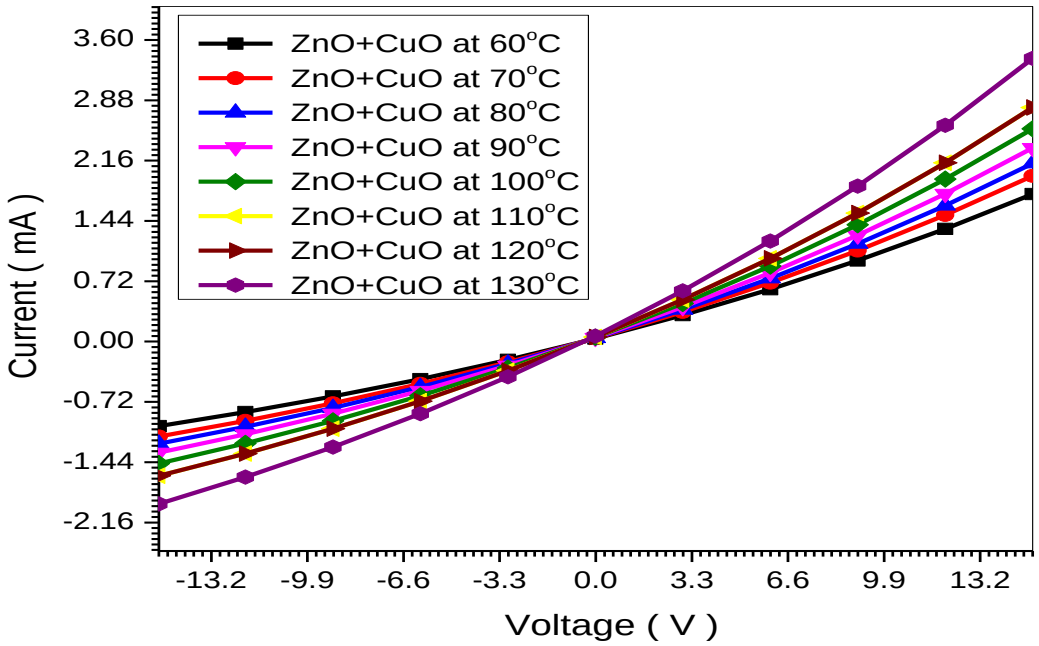

Fig (5.8) The I-V curves of ZnO/CuO p-n junction for 8 samples by annealed different temperatures under particular solar radiation.

5.4.1.3 XRD

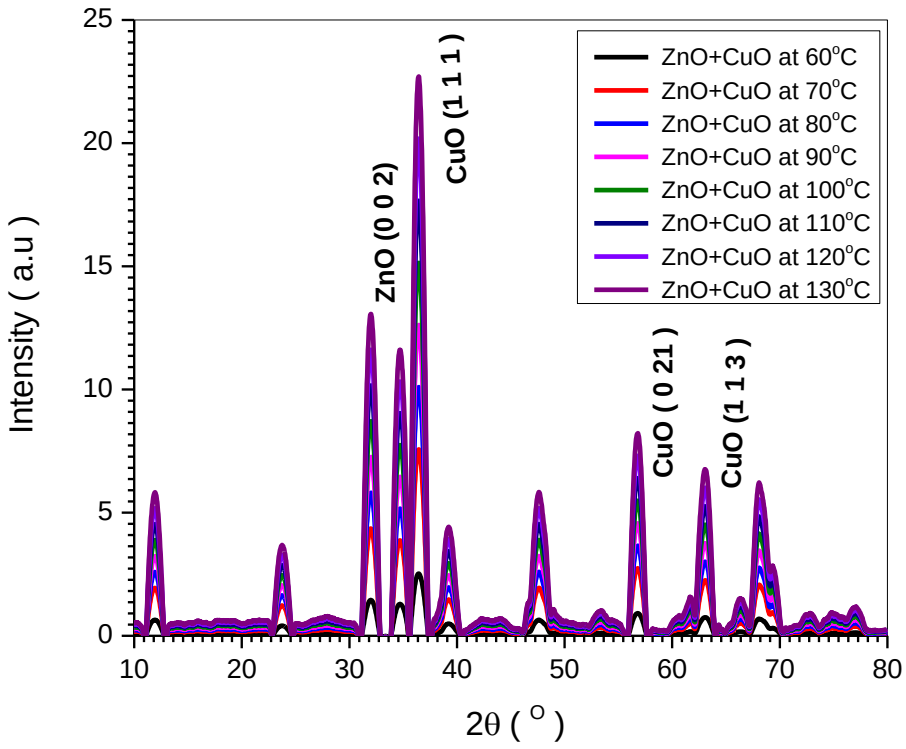

Fig (5.9) XRD patterns of the as prepared ZnO/CuO synthesized 8 samples at different annealed temperatures (60, 70, 80, 90, 100, 110, 120 and 130) ^{O}C for three hours

Table (5.3) some parameters from XRD patterns of the as prepared ZnO/CuO synthesized 8 samples at different annealed temperatures (60, 70, 80, 90, 100, 110, 120 and 130) ^{O}C for three hours

d (nm)	Intensity	Phase ID	d(nm)	I%	h	k	l	2-Theta
0.25852	467	ZnO	0.26033	44.0	0	0	2	34.421
0.24591	589	CuO	0.24595	100.0	1	1	1	36.502
0.16167	164	CuO	0.16179	0.6	0	2	1	56.862
0.13752	122	CuO	0.13752	8.6	1	1	3	68.131

An XRD pattern analysis of ZnO/CuO samples revealed phase purity and excellent crystallinity of ZnO. The phase separation between ZnO and CuO is visible, confirming the existence of both ZnO and CuO phases. All peaks are in good agreement with standard data Fig (5.9). More detailed analysis indicated the presence of a ZnO/CuO phase in table (5.3). In the XRD region from 30^{O} to 70^{O}, observed slightly amorphous background, probably related to the glass substrate of the sample. XRD analysis was used to obtain the phase and crystalline properties of the sample. Figure (5.9) shows the XRD patterns of the as collected samples of ZnO/CuO. The upper patterns correspond to the ZnO/CuO synthesized 8 samples at different annealed temperatures (60, 70, 80, 90, 100, 110, 120 and 130) ^{O}C for three hours. Apart from the most intense line obtained at $2\theta = 34.421^{O}$ corresponding to (002) plane of ZnO other lines appeared at $2\theta = 36.502^{O}$, 56.862^{O} and 68.131^{O} corresponding to the (h k l) planes of (111), (0 2 1) and (1 1 3), respectively planes of pure monoclinic structure of CuO. These were seen to closely resemble the data for spinel cubic structure confirming the formation of crystalline phase of ZnO/CuO. The absence of any additional lines, in any of the XRD patterns, confirms the purity of the ZnO/CuO phase in all the samples. The average crystallite size (t) of the

particles, in each case, was determined from the widths of the XRD lines using the Scherrer formula given by

$$t = \frac{0.9\lambda}{\beta cos\theta} \quad (5.15)$$

Where (λ) is the wavelength of X-rays, (θ) the Bragg angle and (β) the full width of the diffraction line at half of the maximum intensity. The average crystallite size was estimated to be around (1.51 μm, 1.22 μm, 561.4 nm, 223.3 nm, 170.5 nm, 133.2 nm, 109 nm and 96.2 nm) among the different synthesized samples (at different annealed temperatures (60, 70, 80, 90, 100, 110, 120 and 130) ^{O}C for three hours). This measurement points out towards the important information that the variation in the crystallite size is not very significant even though the reactor parameters are varied substantially. It may be, therefore, inferred that the crystallite size is less affected by the operating pressure and temperatures currents during the synthesis in a different annealed temperatures.

5.4.1.4 Scanning Electron Microscopy (SEM)

The morphology and particle sizes of the as-prepared sample were determined by SEM ((SEM, Tuscan Vega LMU).. The SEM images of ZnO+ CuO sample films were annealed at 60^{O}C temperatures are shown in Fig (3). These indicate that sphere-like ZnO+ CuO sample films were annealed at 60^{O}C temperatures nanostructures obtained by this method are uniform in both morphology and particle size, but have agglomeration to some extent. The average size was calculated to be 1.5μm from the measurements on the SEM micrographs. Corresponding histograms, showing the particle size distribution, are also presented in fig (2). The mean particle size 1.5 μm estimated from SEM is in close agreement with the average crystallite size 1.514 μm as calculated from histograms line broadening. The microstructure and chemical composition of the

film surface were analyzed using a scanning electron microscope (SEM, Tuscan Vega LMU). Their sizes are found to range from 1.5 to 1.514 μm

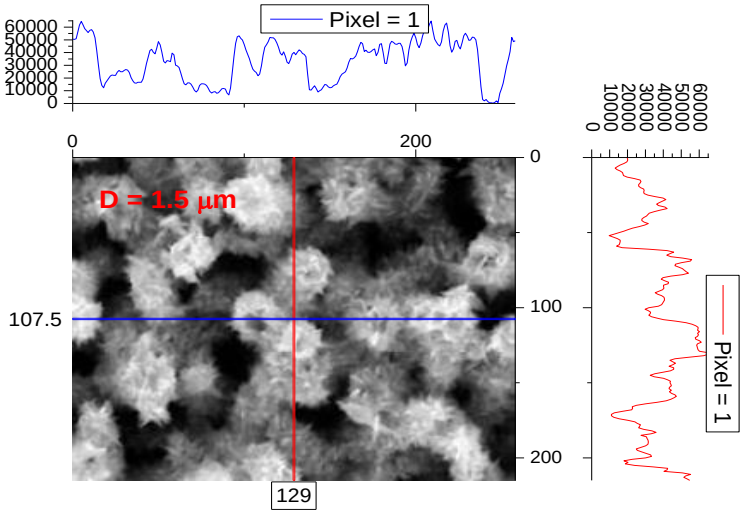

Figure (5.10) SEM images of the ZnO+ CuO sample films were annealed at 60^{O}C temperatures

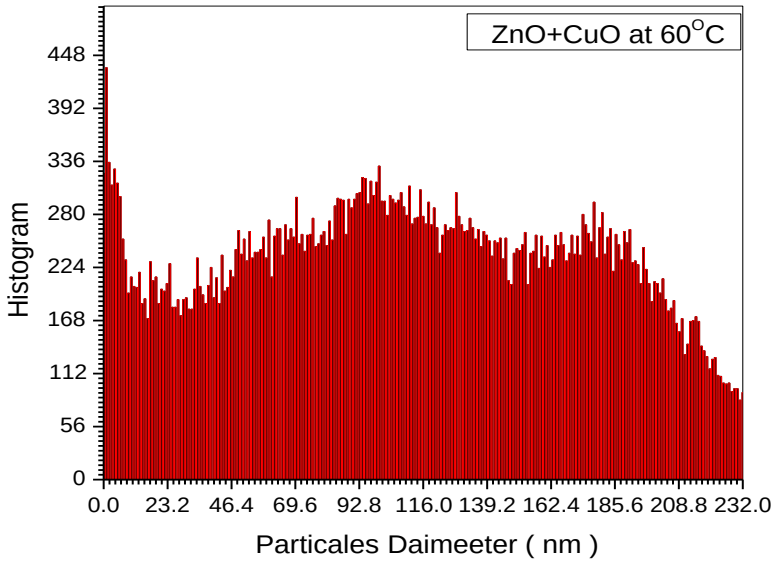

Figure (5.11) Particle diameter distribution of ZnO+ CuO sample films were annealed at 60^{O}C temperatures

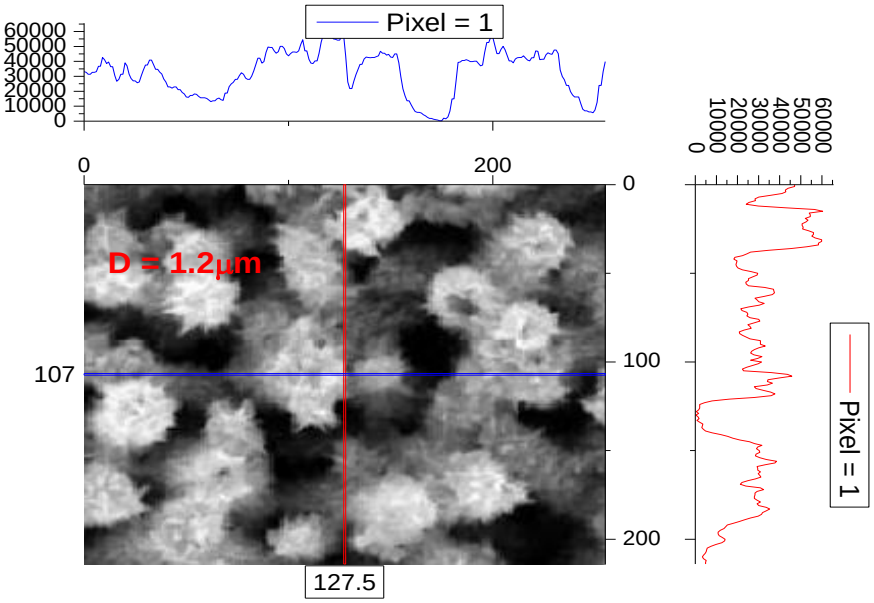

Fig (5.12) SEM images of the ZnO+ CuO sample films were annealed at 70^{O}C temperatures

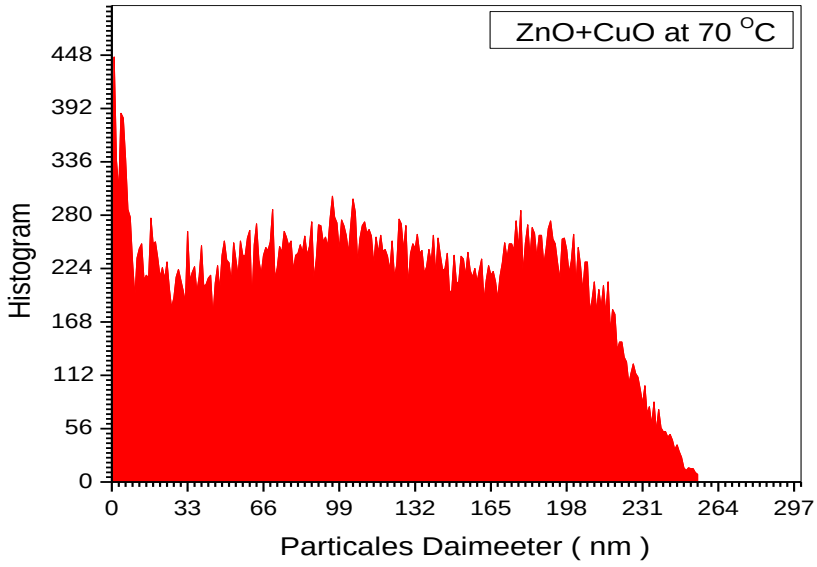

Figure Figure (5.13) Particle diameter distribution of ZnO+ CuO sample films were annealed at 70^{O}C temperature

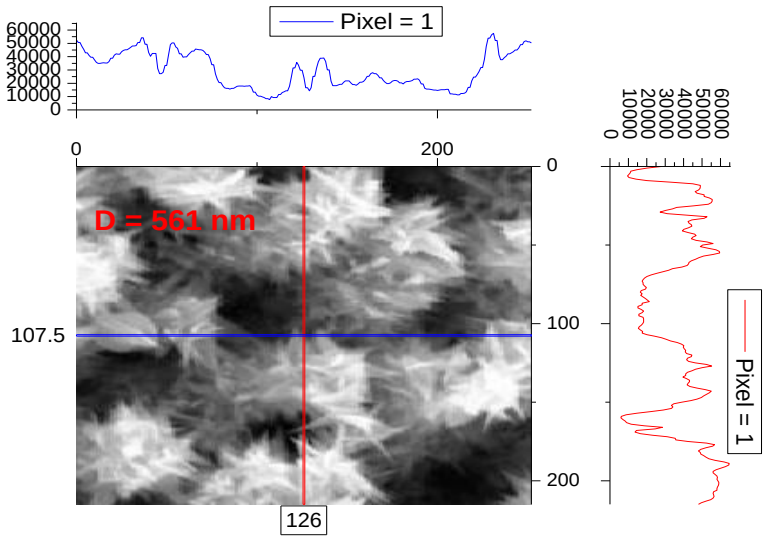

Figure (514) SEM images of the ZnO+ CuO sample films were annealed at 80^{O}C temperatures

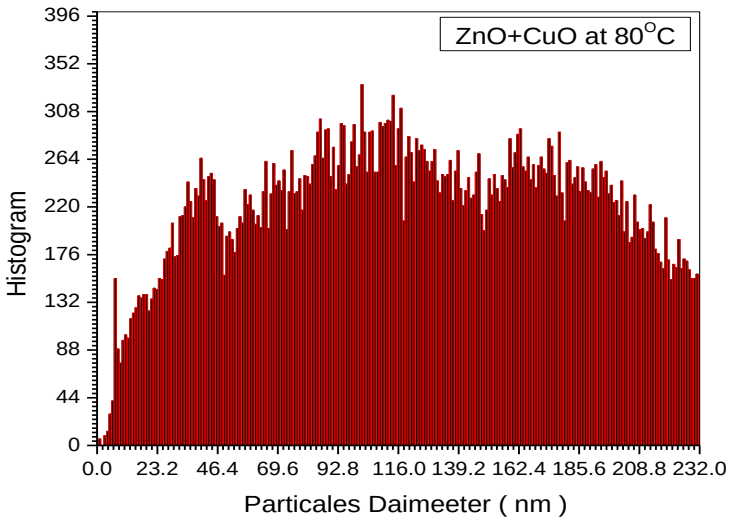

Figure (5.15) Particle diameter distribution of ZnO+ CuO sample films were annealed at 80^{O}C temperatures

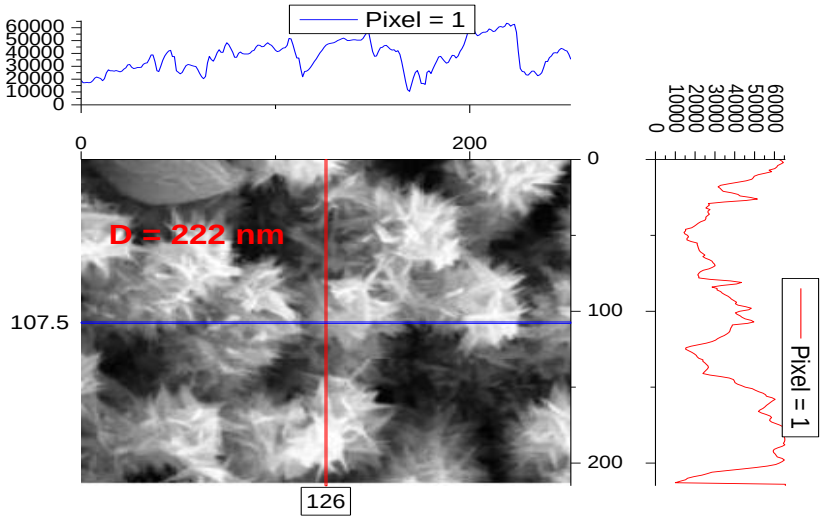

Figure (5.16) SEM images of the ZnO+ CuO sample films were annealed at 90^{O}C temperatures

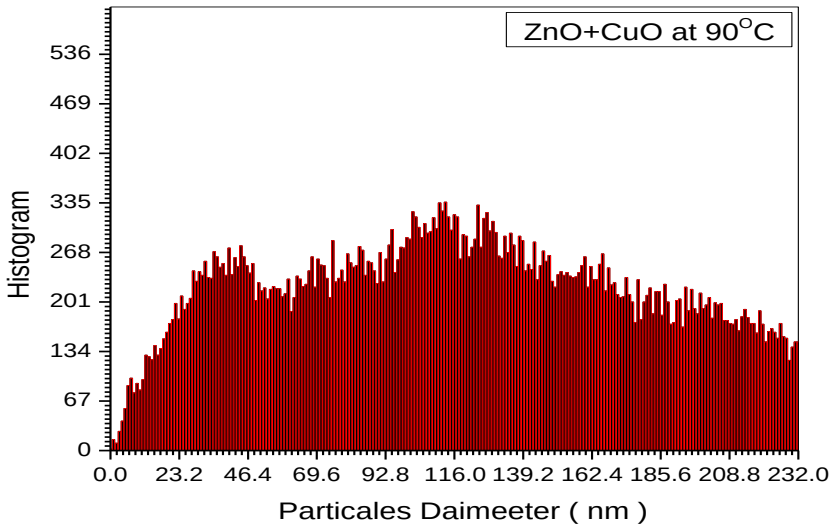

Figure (5.17) Particle diameter distribution of ZnO+ CuO sample films were annealed at 90^{O}C temperatures

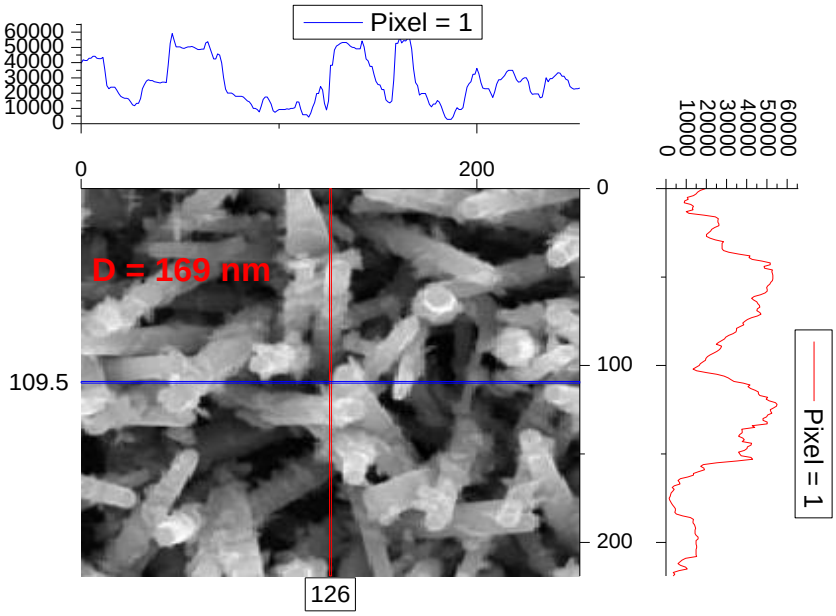

Figure (5.18) SEM images of the ZnO+ CuO sample films were annealed at 100^{O}C temperatures

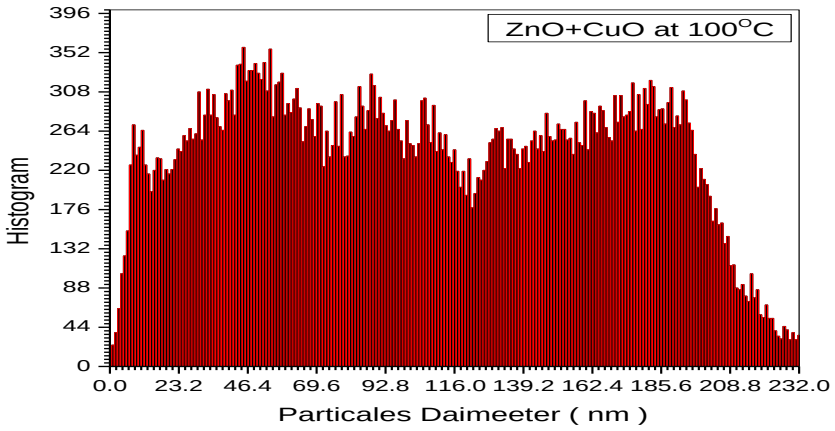

Figure (5.19) Particle diameter distribution of ZnO+ CuO sample films were annealed at 100^{O}C temperatures

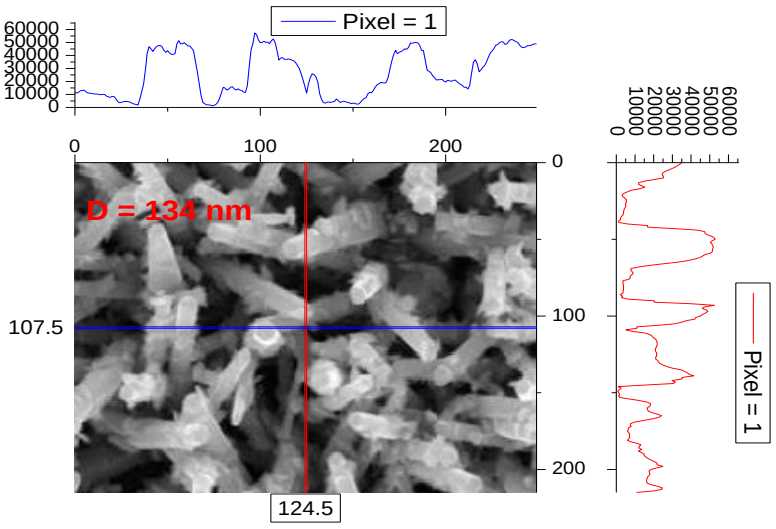

Figure (5.20) SEM images of the ZnO+ CuO sample films were annealed at 110^{O}C temperatures

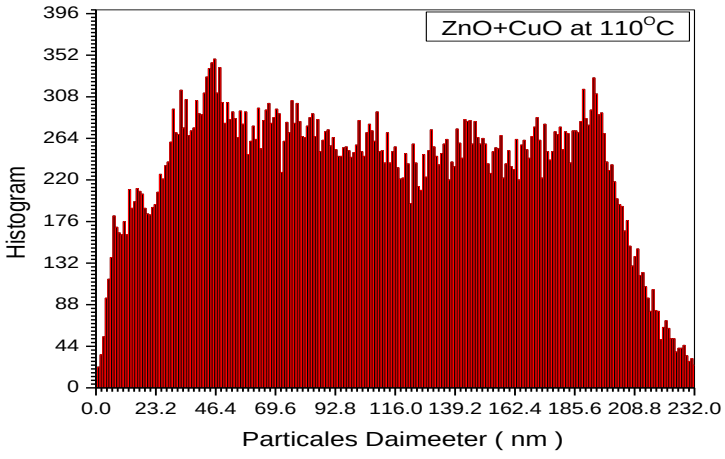

Figure (5.21) Particle diameter distribution of ZnO+ CuO sample films were annealed at 110^{O}C temperatures

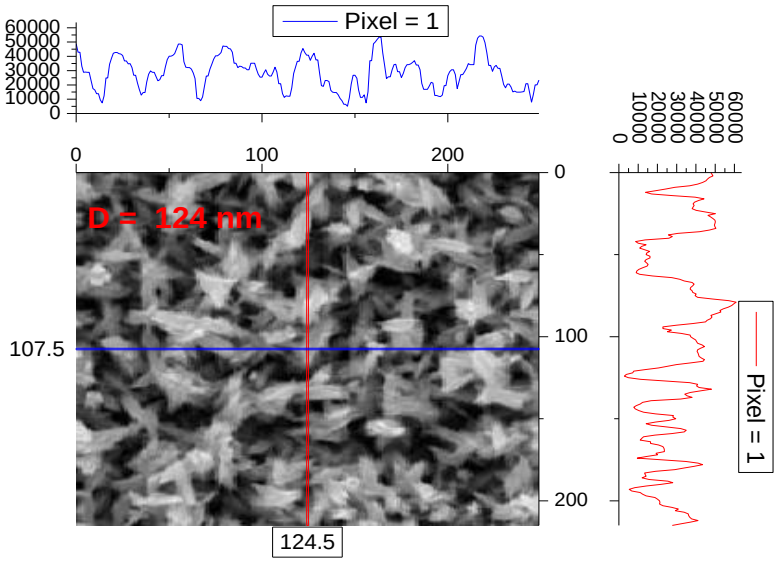

Figure (5.22) SEM images of the ZnO+ CuO sample films were annealed at 120^{O}C temperatures

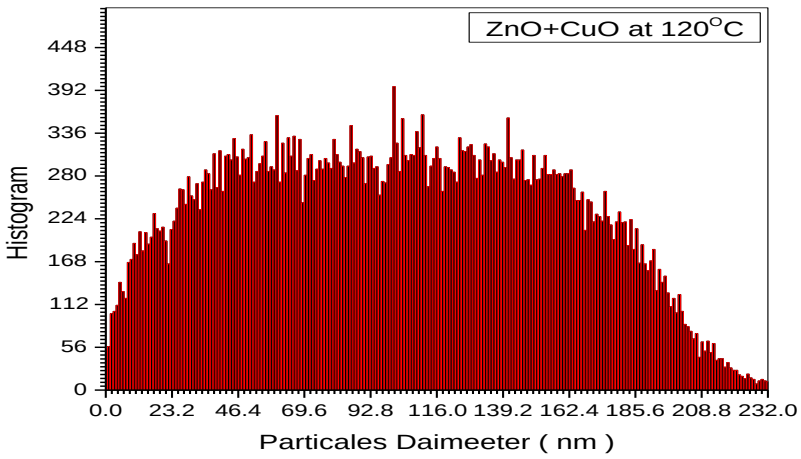

Fig (5.23) Particle diameter distribution of ZnO+ CuO sample films were annealed at 120^{O}C Temperatures

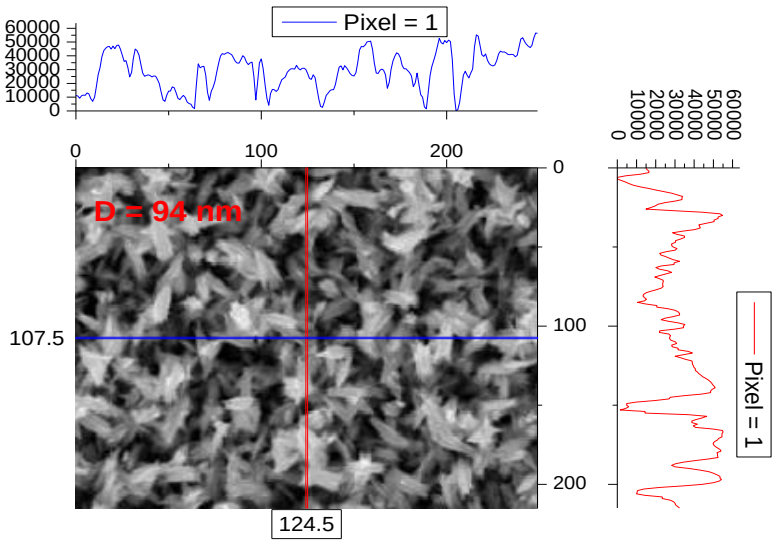

Figure (5.24) SEM images of the images of the ZnO+ CuO sample films were annealed at 130^{O}C temperatures

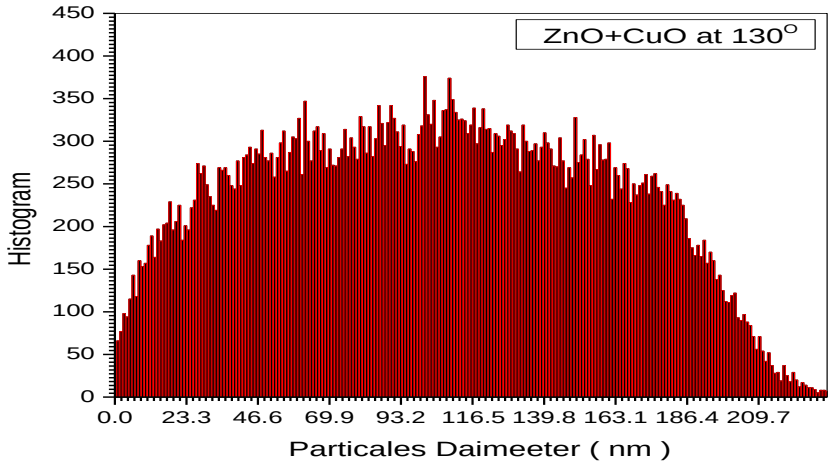

Figure (5.25) Particle diameter distribution of ZnO+ CuO sample films were annealed at 130^{O}C temperatures

- The morphology and particle sizes of the as-prepared sample were determined by SEM. The SEM images of ZnO+ CuO sample films were annealed at 60^{O}C temperatures are shown in Figure (5.10). These indicate that sphere-like ZnO+ CuO sample films were annealed at 60^{O}C temperatures nanostructures obtained by this method are uniform in both morphology and particle size, but have agglomeration to some extent. The average size was calculated to be 1.5μm from the measurements on the SEM micrographs. Corresponding histograms, showing the particle size distribution, are also presented in figure (5.11). The mean particle size 1.5 μm estimated from SEM is in close agreement with the average crystallite size 1.514 μm as calculated from histograms line broadening. The microstructure and chemical composition of the film surface were analyzed using a scanning electron microscope (SEM, Tuscan Vega LMU). Their sizes are found to range from 1.5 to 1.514 μm.
- The morphology and particle sizes of the as-prepared sample were determined by SEM. The SEM images of ZnO+ CuO sample films were annealed at 70^{O}C temperatures are shown in Figure (5.12). These indicate that sphere-like ZnO+ CuO sample films were annealed at 70^{O}C temperatures nanostructures obtained by this method are uniform in both morphology and particle size, but have agglomeration to some extent. The average size was calculated to be 1.2μm from the measurements on the SEM micrographs. Corresponding histograms, showing the particle size distribution, are also presented in figure (5.13). The mean particle size 1.2 μm estimated from SEM is in close agreement with the average crystallite size 1.216 μm as calculated from histograms line broadening. The microstructure and chemical composition of the film surface were analyzed using a scanning electron microscope (SEM, Tuscan Vega LMU). Their sizes are found to range from 1.2 to 1.216 μm.

- The morphology and particle sizes of the as-prepared sample were determined by SEM. The SEM images of ZnO+ CuO sample films were annealed at 80^{O}C temperatures are shown in Figure (5.14). These indicate that sphere-like ZnO+ CuO sample films were annealed at 80^{O}C temperatures nanostructures obtained by this method are uniform in both morphology and particle size, but have agglomeration to some extent. The average size was calculated to be 561 nm from the measurements on the SEM micrographs. Corresponding histograms, showing the particle size distribution, are also presented in figure (5.15). The mean particle size 561 nm estimated from SEM is in close agreement with the average crystallite size 561.56 nm as calculated from histograms line broadening. The microstructure and chemical composition of the film surface were analyzed using a scanning electron microscope (SEM, Tuscan Vega LMU). Their sizes are found to range from 561 to 561.56 nm.
- The morphology and particle sizes of the as-prepared sample were determined by SEM. The SEM images of ZnO+ CuO sample films were annealed at 90^{O}C temperatures are shown in Figure (5.16). These indicate that sphere-like ZnO+ CuO sample films were annealed at 90^{O}C temperatures nanostructures obtained by this method are uniform in both morphology and particle size, but have agglomeration to some extent. The average size was calculated to be 222 nm from the measurements on the SEM micrographs. Corresponding histograms, showing the particle size distribution, are also presented in figure (5.17). The mean particle size 222 nm estimated from SEM is in close agreement with the average crystallite size 223.23 nm as calculated from histograms line broadening. The microstructure and chemical composition of the film surface were analyzed using a scanning electron microscope (SEM, Tuscan Vega LMU). Their sizes are found to range from 222 to 223.23 nm.

- The morphology and particle sizes of the as-prepared sample were determined by SEM. The SEM images of ZnO+ CuO sample films were annealed at $100^{O}C$ temperatures are shown in Figure (5.18). These indicate that sphere-like ZnO+ CuO sample films were annealed at $100^{O}C$ temperatures nanostructures obtained by this method are uniform in both morphology and particle size, but have agglomeration to some extent. The average size was calculated to be 169 nm from the measurements on the SEM micrographs. Corresponding histograms, showing the particle size distribution, are also presented in figure (5.19). The mean particle size 169 nm estimated from SEM is in close agreement with the average crystallite size 170.44 nm as calculated from histograms line broadening. The microstructure and chemical composition of the film surface were analyzed using a scanning electron microscope (SEM, Tuscan Vega LMU). Their sizes are found to range from 169 to 170.44 nm.
- The morphology and particle sizes of the as-prepared sample were determined by SEM. The SEM images of ZnO+ CuO sample films were annealed at $110^{O}C$ temperatures are shown in Figure (5.20). These indicate that sphere-like ZnO+ CuO sample films were annealed at $110^{O}C$ temperatures nanostructures obtained by this method are uniform in both morphology and particle size, but have agglomeration to some extent. The average size was calculated to be 134 nm from the measurements on the SEM micrographs. Corresponding histograms, showing the particle size distribution, are also presented in figure (5.21). The mean particle size 134 nm estimated from SEM is in close agreement with the average crystallite size 130.4 nm as calculated from histograms line broadening. The microstructure and chemical composition of the film surface were analyzed using a scanning electron microscope (SEM, Tuscan Vega LMU). Their sizes are found to range from 130.4 to 134 nm.

- The morphology and particle sizes of the as-prepared sample were determined by SEM. The SEM images of ZnO+ CuO sample films were annealed at $120^{O}C$ temperatures are shown in Figure (5.22). These indicate that sphere-like ZnO+ CuO sample films were annealed at $120^{O}C$ temperatures nanostructures obtained by this method are uniform in both morphology and particle size, but have agglomeration to some extent. The average size was calculated to be 124 nm from the measurements on the SEM micrographs. Corresponding histograms, showing the particle size distribution, are also presented in figure (5.23). The mean particle size 124 nm estimated from SEM is in close agreement with the average crystallite size 109 nm as calculated from histograms line broadening. The microstructure and chemical composition of the film surface were analyzed using a scanning electron microscope (SEM, Tuscan Vega LMU). Their sizes are found to range from 109 to 124 nm.
- The morphology and particle sizes of the as-prepared sample were determined by SEM. The SEM images of ZnO+ CuO sample films were annealed at $130^{O}C$ temperatures are shown in Figure (5.24). These indicate that sphere-like ZnO+ CuO sample films were annealed at $130^{O}C$ temperatures nanostructures obtained by this method are uniform in both morphology and particle size, but have agglomeration to some extent. The average size was calculated to be 92 nm from the measurements on the SEM micrographs. Corresponding histograms, showing the particle size distribution, are also presented in figure (5.25). The mean particle size 92 nm estimated from SEM is in close agreement with the average crystallite size 94.69 nm as calculated from histograms line broadening. The microstructure and chemical composition of the film surface were analyzed using a scanning electron microscope (SEM, Tuscan Vega LMU). Their sizes are found to range from 92 to 94.69 nm.

5.5 Discussion

In this work the ZnO/CuO junction V-I characteristics was studied in two cases firstly exposed to light directly secondly when it was no light (in darkness).

When no light is exposed (in darkness), it was observed that upon increasing the temperature from 600 to 130 in steps of 10 ^{0}C, the current increases with temperature when the voltage is fixed. This may be attributed to the fact that the increase of temperature gives more electrons to gain thermal energy to move from the valance band to conduction band thus increases the current. It is also interesting to note that the current is nearly vanishes at a negative voltage equal to about – 1.8 volt. This reflects the existance of reverse bias voltage and energy gap of order 1.8 eV. The existance of negative reverse current is clearly conforms to relation:

$$I = I_0\left(e^{\beta V} - 1\right) - I_p$$

With V and I_p standing for operating voltage and photon generates current. For reverse bias the voltage is negative, thus the photon generates current dominance, thus $I = -I_p$ this current is assumed to be generated by invisible infra red photons in darkness. These infra red photons generated by human surrounding bodies and the building that exists near the ZnO/CuO diodes. These photon generate currents are less than that generated in light as we will see later

The V-I characteristics in figure (2) of ZnO/CuO unction in light shows again increase in current when temperature increases. This result again confirm the fact that, temperature increase, increases thermal energy, which in turn increases the number of electrons that absorb this energy and transfer to the conduction band. This causes electric current to increase. It is also very interesting to note that the

energy gap E_g, which correspond to zero current, increases with temperature, which agrees with theoretical relations, when

$$n = n_0 e^{-\frac{E_g}{KT}} \quad \text{and} \quad E_g = KT \ln \frac{n_0}{n}$$

Where the energy gap E_g is equal to the voltage that corresponding to zero current.

The effect of light can be observed clearly when comparing the values of reverse current at a certain voltage say (2.2 volt), where I in darks is 0.01 mA, and light is about 0.7 mA. This is relates to the fact that reverse current $I \sim I_p$. Thus in light current generated by visible photons is considerately large than that generated in dark by only free infra red photons.

Figure (5.3) shows that the absorption coefficient α increases upon increasing temperature. This may be attributed to the fact that,, the thermal motion increases with temperature. This increase in thermal motion and vibrating frequency increases collision probability which in turn increases collision of molecules with proton thus decreasing intensity by Compton scattering or by direct proton absorption this agrees with the theoretical relation which shows that $\alpha \sim T^{\frac{1}{2}}$.

In view of figure (4) it is very interesting to note that the absorption has maximum value near the wave length near 540nm. This indicates the existance of energy gab, which agrees with the previous studies concerning ZnO/CuO pn unction the value of wave length at which the absorption is maximum is also with the range predicted by other studies [20].

According to figure (5), the energy gab decreases upon increasing temperature. This conforms to the increase of absorption coefficient because decrease of

energy gab gives chances to more protons to be absorbed by electrons to bridge the gap, where photons of small frequency are absorbed.

5.6 Conclusion

The temperature affects the performance of ZnO/CuO pn junction. This is since temperature increase decreases the energy gab and increases the absorption coefficient.

The ZnO/CuO diode energy gap and V-I characteristics are sensitive to temperature as well as light. This sensitivity can be theoretically explained. Also it was found that for different temperature (60 to 130) the average Particle diameter varied from 1.5 micrometer to 92 nm which indicates that the particle size decreases with raising annealing temperature

References

[1] Yan, L.; Zheng, Y.B.; Zhao, F.; Li, S.; Gao, X.; Xu, B.; Weiss, P.S.; Zhao, Y. Chemistry and physics of a single atomic layer: Strategies and challenges for fictionalization of grapheme and grapheme-based materials. Chem. Soc. Rev. 2012, 41, 97–114.

[2] Amelia, M.; Lincheneau, C.; Silvi, S.; Credi, A. Electrochemical properties of CdSe and CdTe quantum dots. Chem. Soc. Rev. 2012, 41, 5728–5743.

[3] Joh, D.Y.; Kinder, J.; Herman, L.H.; Ju, S.-Y.; Segal, M.A.; Johnson, J.N.; Chan Garnet, K.L.; Park, J. Single-walled carbon nanotubes as excitonic optical wires. Nat. Nanotechol. 2011, 6, 51–56.

[4] Tang, F.; Li, L.; Chen, D. Mesoporous silica nanoparticles: Synthesis, biocompatibility and drug delivery. Adv. Mater. 2012, 24, 1504–1534.

[5] Laurent, S.; Forge, D.; Port, M.; Roch, A.; Robic, C.; van der Elst, L.; Muller, R.N. Magnetic iron oxide nanoparticles: synthesis, stabilization, factorization, physicochemical characterizations, and biological applications. Chem. Rev. 2008, 108, 2064–2110.

[6] Nasu, A.; Otsubo, Y. Rheology and UV protection properties of suspensions of fine titanium dioxides in silicone oil. J. Colloid Interface Sci. 2006, 296, 558–564.

[7] Colvin, V.L.The potential environmental impact of engineered nanomaterials. Nat. Biotechnology. 2003, 21, 1166–1170.

[8] Liu, Z.; Robinson, J.T.; Sun, X.; Dai, H. PEGylated aanographene oxide for delivery of water-insoluble cancer drugs. J. Am. Chem. Soc. 2008, 130, 10876–10877.

[9] Sun, X.; Liu, Z.; Welsher, K.; Robinson, J.; Goodwin, A.; Zaric, S.; Dai, H. Nano-grapheme oxide for cellular imaging and drug delivery. Nano Res. 2008, 1, 203–212.

[10] Yang, K.; Zhang, S.; Zhang, G.; Sun, X.; Lee, S.-T.; Liu, Z. Graphene in mice: Ultrahigh in vivo tumor uptake and efficient photo thermal therapy. Nano Lett. 2010, 10, 3318–3323.

[11] Liu, Z.; Chen, K.; Davis, C.; Sherlock, S.; Cao, Q.; Chen, X.; Dai, H. Drug delivery with carbon nanotubes for in vivo cancer treatment. Cancer Res. 2008, 68, 6652–6660.

[12] Harhaji, L.; Isakovic, A.; Raicevic, N.; Markovic, Z.; Todorovic-Markovic, B.; Nikolic, N.; Vranjes-Djuric, S.; Markovic, I.; Trajkovic, V. Multiple mechanisms underlying the anticancer action of nanocrystalline fullerene. Eur. J. Pharmacol. 2007, 568, 89–98.

[13] Kahru, A.; Dubourguier, H.-C. from ecotoxicology to nano ecotoxicology. Toxicology 2010, 269, 105–119.

[14]. Nations, S.; Wages, M.; Cañas, J. E.; Maul, J.; Theodora is, C.; Cobb, G.P. Acute effects of Fe2O3, TiO2, ZnO and CuO nanomaterials on Xenopus laevis. Chemosphere 2011, 83, 1053–1061.

[15] Cava, R.J. Structural chemistry and the local charge picture of copper oxide superconductors. Science 1990, 247, 656–662.

[16] Tranquada, J.M.; Sternlieb, B.J.; Axe, J.D.; Nakamura, Y.; Uchida, S. Evidence for stripe correlations of spins and holes in copper oxide superconductors. Nature 1995, 375, 561–563.

[17] Xu, J.F.; Ji, W.; Shen, Z.X.; Tang, S.H.; Ye, X.R.; Jia, D.Z.; Xin, X.Q. Preparation and characterization of CuO nanocrystals. J. Solid State Chem. 1999, 147, 516–519.

[18] Namburu, P.K.; Kulkarni, D.P.; Misra, D.; Das, D.K. Viscosity of copper oxide nanoparticles dispersed in ethylene glycol and water mixture. Exp. Therm. Fluid Sci. 2007, 32, 397–402.

[19] Chowdhuri, A.; Gupta, V.; Sreenivas, K.; Kumar, R.; Mozumdar, S.; Patanjali, P.K. Response speed of SnO2-based H2S gas sensors with CuO nanoparticles. Appl. Phys. Lett. 2004, 84, 1180–1182.

[20] Jammi, S.; Sakthivel, S.; Rout, L.; Mukherjee, T.; Mandal, S.; Mitra, R.; Saha, P.; Punniyamurthy, T. CuO nanoparticles catalyzed C-N, C-O, and C-S cross-coupling reactions: Scope and mechanism. J. Org. Chem. 2009, 74, 1971–1976.

[21] Zhang, D.-W.; Yi, T.-H; Chen, C.-H. Cu nanoparticles derived from CuO electrodes in lithium cells. Nanotechnology 2005, 16, 2338–2341.

[22] Dar, M.A.; Kim, Y.S.; Kim, W.B.; Sohn, J.M.; Shin, H.S. Structural and magnetic properties of CuO nanoneedles synthesized by hydrothermal method. Appl. Surf. Sci. 2008, 254, 7477–7481.

[23] Yin, M.; Wu, C.-K.; Lou, Y.; Burda, C.; Koberstein, J.T.; Zhu, Y.; O'Brien, S. Copper oxide nanocrystals. J. Am. Chem. Soc. 2005, 127, 9506–9511.

[24] Zhou, K.; Wang, R.; Xu, B.; Li, Y. Synthesis, characterization and catalytic properties of CuO nanocrystals with various shapes. Nanotechnology 2006, 17, 3939–3943.

[25] Chang, H.; Jwo, C.S.; Lo, C.H.; Tsung, T.T.; Kao, M.J.; Lin, H.M. Rheology of CuO nanoparticle suspension prepared by ASNSS. Rev. Adv. Mater. Sci. 2005, 10, 128–132.

[26] Hernández Battez, A.; González, R.; Viesca, J.L.; Fernández, J.E.; Díaz Fernández, J.M.; Machado, A.; Chou, R.; Riba, J. CuO, ZrO2 and ZnO nanoparticles as antiwear additive in oil lubricants. Wear 2008, 265, 422–428.

[27] Hernández Battez, A.; Viesca, J.L.; González, R.; Blanco, D.; Asedegbega, E.; Osorio, A. Friction reduction properties of a CuO nanolubricant used as lubricant for a NiCrBSi coating. Wear 2010, 268, 325–328.

[28] Pan, X.; Redding, J.E.; Wiley, P.A.; Wen, L.; McConnell, J.S.; Zhang, B. Mutagenicity evaluation of metal oxide nanoparticles by the bacterial reverse mutation assay. Chemosphere 2010, 79, 113–116.

[29] Stoimenov, P.K.; Klinger, R.L.; Marchin, G.L.; Klabunde, K.J. Metal oxide nanoparticles as bactericidal agents. Langmuir 2002, 18, 6679–6686.

[30] Ren, G.; Hu, D.; Cheng, E.W.C.; Vargas-Reus, M.A.; Reip, P.; Allaker, R.P. Characterisation of copper oxide nanoparticles for antimicrobial applications. Int. J. Antimicrob. Agents 2009, 33, 587–590.

[31] Cash, K.J.; Clark, H.A. Nanosensors and nanomaterials for monitoring glucose in diabetes. Trends Mol. Med. 2010, 16, 584–593.

[32] Becheri, A.; Dürr, M.; Lo Nostro, P.; Baglioni, P. Synthesis and characterization of zinc oxide nanoparticles: Application to textiles as UV-absorbers. J. Nanopart. Res. 2008, 10, 679–689.

[33] Strunk, J.; Kähler, K.; Xia, X.; Muhler, M. The surface chemistry of ZnO nanoparticles applied as heterogeneous catalysts in methanol synthesis. Surf. Sci. 2009, 603, 1776–1783.

[34] Yang, K.; Xing, B.S. Sorption of phenanthrene by humic acid-coated nanosized TiO2 and ZnO. Environ. Sci. Technol. 2009, 43, 1845–1851.

[35] Horie, M.; Nishio, K.; Fujita, K.; Endoh, S.; Miyauchi, A.; Saito, Y.; Iwahashi, H.; Yamamoto, K.; Murayama, H.; Nakano, H.; et al. Protein adsorption of ultrafine metal oxide and its influence on cytotoxicity toward cultured cells. Chem. Res. Toxicol. 2009, 22, 543–553.

[36] Sharma, V.; Shukla, R.K.; Saxena, N.; Parmar, D.; Das, M.; Dhawan, A. DNA damaging potential of zinc oxide nanoparticles in human epidermal cells. Toxicol. Lett. 2009, 185, 211–218.

[37] Galhardi, C.M.; Diniz, Y.S.; Rodrigues, H.G.; Faine, L.A.; Burneiko, R.C.; Ribas, B.O.; Novelli, E.L.B. Beneficial effects of dietary copper supplementation on serum lipids and antioxidant defenses in rats. Ann. Nutr. Metab. 2005, 49, 283–288.

[38] Zietz, B.P.; Dieter, H.H.; Lakomek, M.; Schneider, H.; Keßler-Gaedtke, B.; Dunkelberg, H. Epidemiological investigation on chronic copper toxicity to children exposed via the public drinking water supply. Sci. Total Environ. 2003, 302, 127–144.

[39] Galhardi, C.M.; Diniz, Y.S.; Faine, L.A.; Rodrigues, H.G.; Burneiko, R.C.M.; Ribas, B.O.; Novelli, E.L.B. Toxicity of copper intake: Lipid profile, oxidative stress and susceptibility to renal dysfunction. Food Chem. Toxicol. 2004, 42, 2053–2060.

[40] Yokohira, M.; Hashimoto, N.; Yamakawa, K.; Suzuki, S.; Saoo, K.; Kuno, T.; Imaida, K. Lung carcinogenic bioassay of CuO and TiO2 nanoparticles with intratracheal instillation using F344 male rats. J. Toxicol. Pathol. 2009, 22, 71–78.

[41] Karlsson, H.L.; Cronholm, P.; Gustafsson, J.; Möller, L. Copper Oxide Nanoparticles Are Highly Toxic: A comparison between metal oxide nanoparticles and carbon nanotubes. Chem. Res. Toxicol. 2008, 21, 1726–1732.

[42] Wang, Z.; Li, N.; Zhao, J.; White, J.C.; Qu, P.; Xing, B. CuO nanoparticle interaction with human epithelial cells: Cellular uptake, location, export, and genotoxicity. Chem. Res. Toxicol. 2012, 25, 1512–1521.

[43] Fahmy, B.; Cormier, S.A. Copper oxide nanoparticles induce oxidative stress and cytotoxicity in airway epithelial cells. Toxicol. In Vitro 2009, 23, 1365–1371.

[44] Li, J.; Quabius, E.S.; Wendelaar Bonga, S.E.; Flik, G.; Lock, R.A.C. Effects of water-borne copper on branchial chloride cells and Na+/K+-ATPase activities in Mozambique tilapia (Oreochromis mossambicus). Aquat. Toxicol. 1998, 43, 1–11.

[45] Aruoja, V.; Dubourguier, H.-C.; Kasemets, K.; Kahru, A. Toxicity of nanoparticles of CuO, ZnO and TiO2 to microalgae Pseudokirchneriella subcapitata. Sci. Total Environ. 2009, 407, 1461–1468.

[46] Grosell, M.; Blanchard, J.; Brix, K.V.; Gerdes, R. Physiology is pivotal for interactions between salinity and acute copper toxicity to fish and invertebrates. Aquat. Toxicol. 2007, 84, 162–172.

[47] Griffitt, R.J.; Weil, R.; Hyndman, K.A.; Denslow, N.D.; Powers, K.; Taylor, D.; Barber, D.S. Exposure to copper nanoparticles causes gill injury and acute lethality in Zebrafish (Danio rerio). Environ. Sci. Technol. 2007, 41, 8178–8186.

[48] Pelgrom, S.M.G.J.; Lock, R.A.C.; Balm, P.H.M.; Bonga, S.E.W. Integrated physiological response of tilapia, oreochromis mossambicus, to sublethal copper exposure. Aquat. Toxicol. 1995, 32, 303–320.

[49] Gomes, T.; Pereira, C.G.; Cardoso, C.; Pinheiro, J.P.; Cancio, I.; Bebianno, M.J. Accumulation and toxicity of copper oxide nanoparticles in the digestive gland of Mytilus galloprovincialis. Aquat. Toxicol. 2012, 118–119, 72–79.

[50] Shi, J.; Abid, A.D.; Kennedy, I.M.; Hristova, K.R.; Silk, W.K. To duckweeds (Landoltia punctata), nanoparticulate copper oxide is more inhibitory than the soluble copper in the bulk solution. Environ. Pollut. 2011, 159, 1277–1282.

[51] Bondarenko, O.; Ivask, A.; Käkinen, A.; Kahru, A. Sub-toxic effects of CuO nanoparticles on bacteria: Kinetics, role of Cu ions and possible mechanisms of action. Environ. Pollut. 2012, 169, 81–89.

[52]. Mortimer, M.; Kasemets, K.; Heinlaan, M.; Kurvet, I.; Kahru, A. High throughput kinetic vibrio fischeri bioluminescence inhibition assay for study of toxic effects of nanoparticles. Toxicol. In Vitro 2008, 22, 1412–1417.

[53] Mortimer, M.; Kasemets, K.; Kahru, A. Toxicity of ZnO and CuO nanoparticles to ciliated protozoa Tetrahymena thermophila. Toxicology 2010, 269, 182–189.

[54] Franklin, N.M.; Rogers, N.J.; Apte, S.C.; Batley, G.E.; Gadd, G.E.; Casey, P.S. Comparative toxicity of nanoparticulate ZnO, bulk ZnO, and ZnCl2 to a freshwater microalga (Pseudokirchneriella subcapitata): The importance of particle solubility. Environ. Sci. Technol. 2007, 41, 8484–8490.

[55] Cross, S.E.; Innes, B.; Roberts, M.S.; Tsuzuki, T.; Robertson, T.A.; McCormick, P. Human skin penetration of sunscreen nanoparticles: In-vitro assessment of a novel micronized zinc oxide formulation. Skin Pharmacol. Physiol. 2007, 20, 148–154.

[56] Zheng, Y.; Li, R.; Wang, Y. In vitro and in vivo biocompability of ZnO nanoparticles. Int. J. Mod. Phys. B 2009, 23, 1566–1571.

[57] Wang, B.; Feng, W.; Wang, M.; Wang, T.; Gu, Y.; Zhu, M.; Ouyang, H.; Shi, J.; Zhang, F.; Zhao, Y.; et al. Acute toxicological impact of nano- and submicro-scaled zinc oxide powder on healthy adult mice. J. Nanopart. Res. 2008, 10, 263–276.

[58] Brunner, T.J.; Wick, P.; Manser, P.; Spohn, P.; Grass, R. N.; Limbach, L. K.; Bruinink, A.; Stark, W.J. In vitro cytotoxicity of oxide nanoparticles: Comparison to asbestos, silica, and the effect of particle solubility. Environ. Sci. Technol. 2006, 40, 4374–4381.

[59] Wang, H.; Wick, R.L.; Xing, B. Toxicity of nanoparticulate and bulk ZnO, Al2O3 and TiO2 to the nematode Caenorhabditis elegans. Environ. Pollut. 2009, 157, 1171–1177.

[60] De Berardis, B.; Civitelli, G.; Condello, M.; Lista, P.; Pozzi, R.; Arancia, G.; Meschini, S. Exposure to ZnO nanoparticles induces oxidative stress and cytotoxicity in human colon carcinoma cells. Toxicol. Appl. Pharmacol. 2010, 246, 116–127.

[61] Lin, D.; Xing, B. Phytotoxicity of nanoparticles: Inhibition of seed germination and root growth. Environ. Pollut. 2007, 150, 243–250.

[62] Xiong, D.; Fang, T.; Yu, L.; Sima, X.; Zhu, W. Effects of nano-scale TiO2, ZnO and their bulk counterparts on zebrafish: acute toxicity, oxidative stress and oxidative damage. Sci. Total Environ. 2011, 409, 1444–1452.

[63] Buffet, P.-E.; Amiard-Triquet, C.; Dybowska, A.; Risso-de Faverney, C.; Guibbolini, M.; Valsami-Jones, E.; Mouneyrac, C. Fate of isotopically labeled zinc oxide nanoparticles in sediment and effects on two endobenthic species, the

clam Scrobicularia plana and the ragworm Hediste diversicolor. Ecotoxicol. Environ. Saf. 2012, 84, 191–198.

[64] Blinova, I.; Ivask, A.; Heinlaan, M.; Mortimer, M.; Kahru, A. Ecotoxicity of nanoparticles of CuO and ZnO in natural water. Environ. Pollut. 2010, 158, 41–47.

[65] Pipan-Tkalec, Z.; Drobne, D.; Jemec, A.; Romih, T.; Zidar, P.; Bele, M. Zinc bioaccumulation in a terrestrial invertebrate fed a diet treated with particulate ZnO or ZnCl2 solution. Toxicology 2010, 269, 198–203.

[66] Yamamoto, O. Influence of particle size on the antibacterial activity of zinc oxide. Int. J. Inorg. Mater. 2001, 3, 643–646.

[67] Jiang, W.; Mashayekhi, H.; Xing, B. Bacterial toxicity comparison between nano- and micro-scaled oxide particles. Environ. Pollut. 2009, 157, 1619–1625.

[68] Hu, X.; Cook, S.; Wang, P.; Hwang, H.-M. In vitro evaluation of cytotoxicity of engineered metal oxide nanoparticles. Sci. Total Environ. 2009, 407, 3070–3072.

[69] Heinlaan, M.; Ivask, A.; Blinova, I.; Dubourguier, H.-C.; Kahru, A. Toxicity of nanosized and bulk ZnO, CuO and TiO2 to bacteria Vibrio fischeri and crustaceans Daphnia magna and Thamnocephalus platyurus. Chemosphere 2008, 71, 1308–1316.

[70] Baek, Y.-W.; An, Y.-J. Microbial toxicity of metal oxide nanoparticles (CuO, NiO, ZnO, and Sb2O3) to Escherichia coli, Bacillus subtilis, and Streptococcus aureus. Sci. Total Environ. 2011, 409, 1603–1608.

[71] Kasemets, K.; Ivask, A.; Dubourguier, H.-C.; Kahru, A. Toxicity of nanoparticles of ZnO, CuO and TiO2 to yeast Saccharomyces cerevisiae. Toxicol. In Vitro 2009, 23, 1116–1122.

[72] Brayner, R.; Ferrari-Iliou, R.; Brivois, N.; Djediat, S.; Benedetti, M.F.; Fiévet, F. Toxicological impact studies based on Escherichia coli bacteria in ultrafine ZnO nanoparticles colloidal medium. Nano Lett. 2006, 6, 866–870.

[73] Yan, L.; Zhao, F.; Li, S.; Hu, Z.; Zhao, Y. Low-toxic and safe nanomaterials by surface-chemical design, carbon nanotubes, fullerenes, metallofullerenes, and graphenes. Nanoscale 2011, 3, 362–382.

[74] Hund-Rinke, K.; Simon, M. Ecotoxic effect of photocatalytic active nanoparticles (TiO2) on algae and Daphnids. Environ. Sci. Pollut. Res. 2006, 13, 225–232.

[75] Mayer, A.; Vadon, M.; Rinner, B.; Novak, A.; Wintersteiger, R.; Fröhlich, E. The role of nanoparticle size in hemocompatibility. Toxicology 2009, 258, 139–147.

[76] Ahmed Khogali, Solar energy, Sudan coin press, Khartoum (2007).

[77] Maissel, L.I, and Change, R., Hand book of thin film technology, MC-Graw-Hill, new york (1970).

[78] N.S. Sariciftci, primary photo excitations in conjngated polymers, world scientific, Singapore.

[79] Pope, M., swenberg, C.E., Electronic processes in organic crystals and polymers, oxford university press, new york (1999).

[80] PhD by dipl. Ing. Klaus Detvitsch“organic solar cell Architectures” Cambridge and craz, July 2000.

[81] Kazuya Fujimoto, Takeo Oku, Tsuyoshi Akiyama and AT sushi Suzuki “ fabrication and characterization, of copper oxide – zinc oxide solar calls prepared by electrode position”, Department of materials science, The university of shiga prefecture, Hikone, Shiga 522 – 8533, Japan 2012.

[82] Hiroki Kidowaki, Takeo Oku and Tsyoshi Akiyama "Fabrication and evaluation of CuO/ZnO Heterostructures for photoelectric conversion 2500 hassaka, hikone, shiga 522-8533 Japan – October 2012.

[83] E.O. Omayio, P.M. Karimi, W.K. Njoroge, F. K. Mugwanga, "current – Voltage characteristics of P-CuO/n-ZnO: sn solar cell" Department of physics and Kenyatta university, Kenya December 2012.

[84] H.Kidowaki, T. Oku, T.Akiyama "Fabrication and characterization of CuO/ ZnO solar cells" Department of Materials Science, The university of shiga prefecture, 2500 Hassaka, hikone Shiga 522 – 8533, Japan 2011.

[85] B. Das, S.P. McGinnis, P. Sines "High Efficiency solar cells based on semiconductor nanostructures" West viranina University. Morgan Town, WV 26506 – 6109, USA September 1999.

[86] A. Kay, M. Gratzel, J. Phys. Chem. 97 (1993), 6272.

[87] Yee – Fun Lim, Joshua Jochaj. choi, and Tobias Hanrath "Facile Synthesis of colloidal CuO nanocrystals for light – harvesting Applications" Gornall University, (Thaca, N.y 148533 – 1501, USA 14 July 2011.

[88] C.I. Brabec and J.R. Durrant "Solution – Processed Organic Solar cells" MRS Bulletin, Vol, 33, no, 7 PP. 670 – 675, 2008.

[89] Li, G., Shrotriya, V., and yao, Y. " Investigations of annealing effects and film thickness dependence of polymer solar cells based on poly (3-hexylthiophent Appl, Phys, V, 98. No. 4, PP- 043704, 2005.

[90] A.K. Pandey, J.M. Nunzi, B- Partier, and A. Molition, "size effect on organic optoelectronics devices", Example of photovoltaic cell efficiency Elsevier, V. 372, PP.1333 – 1326, 2007.

[91] U mang V Desai, Chengkun Xu, Jiamin Wu and Di Gao "solid – state dye – sensitized solar cells based on ordered ZnO nanowire arrays" university of Pittsburgh, PA 15261, USA, 16 march 2012.

[92] M Gloeckler, Al Fahrenbruch, JR sites "Numerical modeling of CIGS and CdTe Solar cells: setting the Baseline" 3rd conf. Pvener - conv., 491 – 494, 2003.

[93] SI Fonash. Solar Cell Device Physics. 2nd edition, Elsevier USA, 2010.

[94] Donald A. Neamen "Semiconductor Physics and Devices", University of New Mexico, 3rd edition, 2008.

[95] CA wolden, Jkurtin, JB Baxter, I Replins, SE Shaheen, JT Torvik, AARocket, VM Fthenakis, ES Aydil "Photovoltaic Manufacturing: Present Status, Future Prospects and research needs" J: Vac. Sci. Technol. A29(3); 03080 i(1.16), 2011.

[96] John and Willi Leone family Department of energy and mineral engineering "Numerical modeling of Tin – Based Absorber devices for cost – effective solar photovoltaic" may 2012.

[97] A. Mittiga, E. Solar , F.Sarto, M. Jucci and R- Vasnthi, Heterojunction solar cell with 2% efficiency based on a CuO substrate, App. Phys. 2006.

[98] M. Izaki, T. Shinagawa, K. Mizuno, Y. Ida, M. Inava and A. Tasaka, Photo chemically hetero junction diode device, J. Phys. D: App. Phys 2007.

[99] B. G hoch, M. Dos, P Banerjee., S DAS " Fabrication of the SnS/ ZnO Hetero Junction for PV Application using electrodeposited ZnO films " Semiconductor. Sci. Techno 2013.

[100] Kamat, P.V, et al (2014) "semiconductor nano particles, in hand book of nano structured materials and nanotechnology, Academic press: New York.

[101] Warfel. P (2009) physics of solar cells – form principles of new concepts, wiley VCH.

[102] R. V inodkumar, K.J.L. etthy, D. Beena A.D. Detty, I. Nava, U. V. nayor, V.P mahadevan, V. Ganesan, V.R.R eddy, Effect of ITO buffer layers on the structural, optical and electrical properties of ZnO multilayer thin films prepared by pulsed laser deposition technique, Sol, energy. Mater. Sol. Cells 2011.

[103] H. Kidowaki, T. Oku, T. Akiyama, "Fabrication and characterization of CuO / ZnO solar cells, Journal of physics: Conference Series, 2012.

[104] V. D. Mihailetchi (2010) Device physics of organic bulk heterojunction solar cells, PHD thesis, University of groningch.

[105] Wirfel (2014), physics of solar cells – 1st ed, weinheim, wiley .VcH.

[106] Peiwei Lv, Weifeng Zheng, Limei Lin, Fuchuan peng, Zhigao Huang, Fachunlai " I-V characteristics of ZnO/ CuO thin film n-i-p heterojunction", School of physics and opto – electronic tech, fuijan Normal university PR China B January 2011.

[107] VA Gevorkyan, A E Reymers, M Neresyan, " Characterization of Cu_2O thin films prepared by evaporation of CuO powder" 2012.

[108] Shih-fong Lee, Yung-Ping Chang, Li-Ying Lee, Jung-Fu Hsu " Characterization of Dye – Sensitized Solar Cells with ZnO Nanorod Multilayer Electrode" 2007 National Kaohsiung University of Applied Sciences, ISSN 1813-3851.

[109] Marius Grundman, "The physics of Semiconductors, An introduction Including Devices and Nano physics, January 2006.

[110] S.M . Sze, Hsincha , Taiwan, Kwakk, Ng san Jose, Clifornia, "Physics of Semiconductor Device Third Edition, July 2006.

[111] Martin A. Freen, Keith emery, yoshihiro hishikawa and Wilhelm warta, Solar cell efficiency tables (version 37), John 2010.

[112] Antonio Facchelttti. (2010), π-Conjugated polymers for organic Electronics and Photovoltaic Cell Applications. Journal of Chemistry and the materials Research Center United States, Northwestern University 214: 202-211.

[113] Bassam Z. Shakhashiri A Handbook for Teachers of Chemistry 'polymers' Journal Chemical or the week, volume 1 (1983), Page 241.

[114] Barry C. Thompson and Jean M. J.Fr_chet*" Polymer-Fullerene Composite Solar Cells" 2008 Wiley-VCH Cerlag GmbH & Co. KGaA, Weinheim Angew. Chem. Int. Ed. 2008.

[115] Chang, R.; Hsu, J.H.; Fann, W. S.; Liang, C.H.; Hayashi, M.; Yu, J.; Lin, S.H.; Chang, E. C.; Chuang, (2000) Investigations of Ultrafest Dynamics in Light-emitting polymers. Journal of chinese Chemical Society (1-2): 142-152.

[116] C.J. Brabec, G. Zerza, G. Cerullo, S. De Silvestri, S. Luzzati, J. C. Hummelen (2001). Tracing photoinduced electron transfer process in conjugated polymer/ fullerence bulk heterojunctions in real time. Journal of chemical physics letters 340: 232-236.

[117] N. S. Sariceftic (Ed.), (1998), Primaty photo excitations in conjugated polymers: Moleculat excition versus Semiconductor Band Model. World Scientific Publishers, Singapore.